UNIVERSITY OF TRENTO

Doctoral School in Civil, Environmental and Mechanical Engineering

Curriculum 3. Modelling and Simulation

Diana Giarola

Dynamic interaction between shear bands

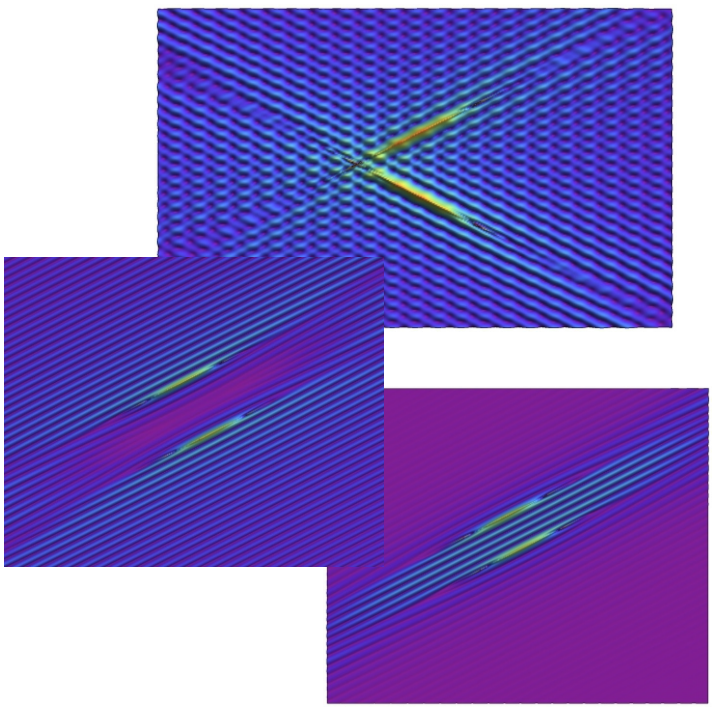

2019 - Doctoral thesis

University of Trento

Doctoral Thesis

Dynamic interaction between shear bands

Author:
Diana Giarola

Supervisor:
Prof. Davide Bigoni
Prof. Andrea Piccolroaz
Dott. Domenico Capuani

Topic 3. Modelling and Simulation
XXXI cycle 2015/2018

Department of Civil, Environmental and Mechanical Engineering
Solid and Structural Mechanics Group

Doctoral School in Civil, Environmental and Mechanical Engineering
http://web.unitn.it/en/dricam
Via Mesiano 77, I-38123 Trento
Tel. +39 0461 282670 / 2611 - dicamphd@unitn.it

UNIVERSITY OF TRENTO
Graduate School in Structural Engineering
Modelling and Simulation
XXXI Cycle

Ph.D. Program Head: prof. D. Bigoni

Final Examination: 28 March 2019

Board of Examiners:
Prof. Raymond W. Ogden University of Glasgow Scotland, UK
Prof. Luigi Gambarotta, Università di Genova, Italia
Prof. Giovanni Noselli, SISSA Scuola Internazionale Superiore di Studi Avanzati, Italia

Abstract

A shear band of finite length, formed inside a ductile material at a certain stage of a continued homogeneous strain, provides a dynamic perturbation to an incident wave field, which strongly influences the dynamics of the material and affects its path to failure. The investigation of this perturbation is presented for a ductile metal, with reference to the incremental mechanics of a material obeying the J_2-deformation theory of plasticity (a special form of prestressed, elastic, anisotropic, and incompressible solid). The treatment originates from the derivation of integral representations relating the incremental mechanical fields at every point of the medium to the incremental displacement jump across the shear band faces, generated by an impinging wave. The boundary integral equations (under the plane strain assumption) are numerically approached through a collocation technique, which takes account of the singularity at the shear band tips and permits the analysis of an incident wave impinging on a shear band.

It is shown that the presence of the shear band induces a resonance, visible in the incremental displacement field and in the stress intensity factor at the shear band tips, which promotes shear band growth. Moreover, the waves scattered by the shear band are shown to generate a fine texture of vibrations, parallel to the shear band line and propagating at a long distance from it, but leaving a sort of conical shadow zone, which emanates from the tips of the shear band.

Moreover, the approach is generalised to study the interaction of multiple shear bands showing that it may lead to resonance and corresponding growth of shear bands, but also to their annihilation. At the same time, multiple scattering may bring about focusing or, conversely, shielding from waves. Due to the difficulties inherent to the experimental analysis of time-harmonic dynamics of shear bands, the proposed mechanical model represents the only practical possibility of analyzing the fine micromechanisms governing material collapse and discloses the complex interplay between dynamics and shear band growth or arrest.

Acknowledgements

Firstly, I would like to thank Professor Davide Bigoni for the great opportunity, the motivation and the encouragements that he gave me in these three years. I am also deeply grateful to Dr. Domenico Capuani for the help and the support despite the great distance, and our super productive meetings from Ferrara to Bologna.
Moreover, I would like to thank all members of the Solid and Structural Mechanics Group at the University of Trento, and in particular the colleagues of "Aula Prof. Bacca" and the Instabilities Lab. Last but not the least, I would like to thank my family and my friends for their constant support during these years.
Support from the ERC Advanced Grant "Instabilities and non-local multiscale modelling of materials" 340561-FP7-PEOPLE-IDEAS-ERC-2013-AdG (2014-2019) is gratefully acknowledged.

List of pubblications

The results reported in the present thesis have been summarized in the following papers:

- D. Bigoni, D. Capuani, D. Giarola (2017). Dynamics of shear bands in a prestressed material. *Conference proceeding of the 21st International Conference on Composite Materials.*

- D. Giarola, D. Capuani, D. Bigoni (2018). The dynamics of a shear band. *Journal of the Mechanics and Physics of Solids* 112, 472-490.

- D. Giarola, D. Capuani, D. Bigoni (2018). Dynamic interaction of multiple shear bands. *Scientific Reports* 8:16033.

- D. Bigoni, D. Capuani, D. Giarola (2019). Scattering of waves by a shear band. *Conference proceeding of the First International Conference on Theoretical, Applied and Experimental Mechanics. ICTAEM 2018. Structural Integrity, vol 5. Springer, Cham.*

Contents

1 Introduction

When a ductile material is subject to severe strain, failure is preluded by the emergence of shear bands which initially nucleate in a small area, but quickly extend rectilinearly and accumulate damage, until they degenerate into fractures. Nucleation and growth of shear bands and their interactions in ductile materials are concurrent causes of failure, a complex process which is strongly affected by dynamics and far from being completely understood. Therefore, research on shear bands yields a fundamental understanding of the intimate rules of failure, so that it may be important in the design of new materials with superior mechanical performances.

The aim of the present thesis is to investigate dynamic perturbations in the stress/deformation fields of an incident wave, induced by multiple shear bands interaction, formed inside a ductile metal, at a certain stage of a continued strain.

The incremental constitutive equations used to describe nonlinear materials are briefly introduced in Chapter 2 together with the condition for their positive definiteness, ellipticity, and regime classification, in the special cases of the J_2-deformation theory of plasticity and Mooney-Rivlin material.

The shear band model is introduced in Chapter 3, together with the boundary conditions that allow to obtain the boundary integral equation presented in Chapter 4 and based on the time-harmonic Green's functions

for the incremental nonlinear elasticity. In order to give a numerical solution to the shear band problem, a Boundary Element Method with an ad hoc collocation technique is formulated.

The case pertaining to an isolated shear band in infinite incompressible nonlinear elastic material is reported in Chapter 5. Displacements, Stress Intensity Factors, and deviatoric strain fields are presented for the cases of a time-harmonic transverse shear wave that travels orthogonal to the shear band, and with generic inclination with respect to it. Results show that wave propagation induces a resonance effect of the shear band, promoting its growth, and show that the scattered field of a shear band is composed by a family of plane waves parallel to the band, Figure 1.1.

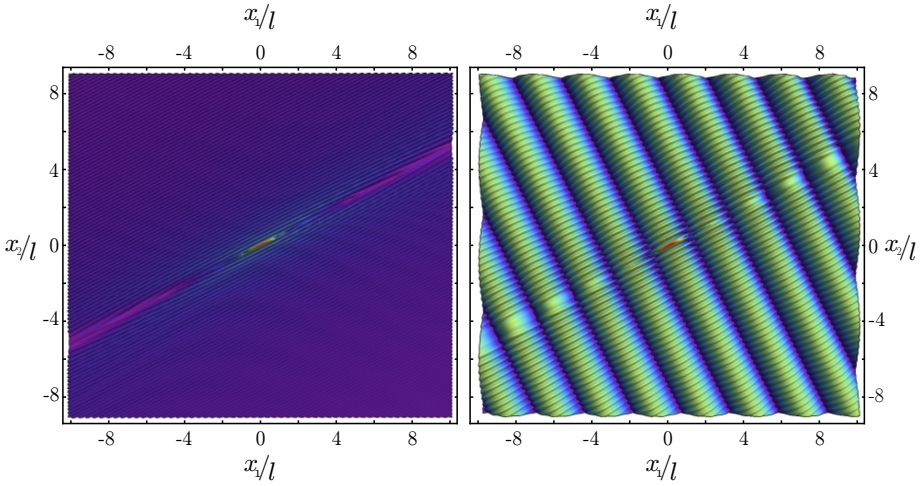

FIGURE 1.1: Scattered (left) and total (right) incremental deviatoric strain field is reported as produced by an incident shear wave travelling parallel to the shear band of length $2\,l$ ($\beta = \theta$, with β direction of the wave propagation and θ inclination of the shear band) with wave number $\Omega\, l/c_1 = 1$ (denoting with Ω the circular frequency and c_1 the wave speed).

The dynamic interaction of multiple shear bands is introduced in Chapter 6, where the appropriate numerical technique used to solve the problem is described in detail. Four different configurations of shear bands are considered in Chapter 7: parallel and aligned shear bands, two

shear bands in a V-shaped configuration and four shear bands in a squared configuration. Results show that different geometries of shear bands can lead to opposite effects, of focusing or shielding from waves (Figure 1.2), and in some cases promote resonance effects or the annihilation of the shear band.

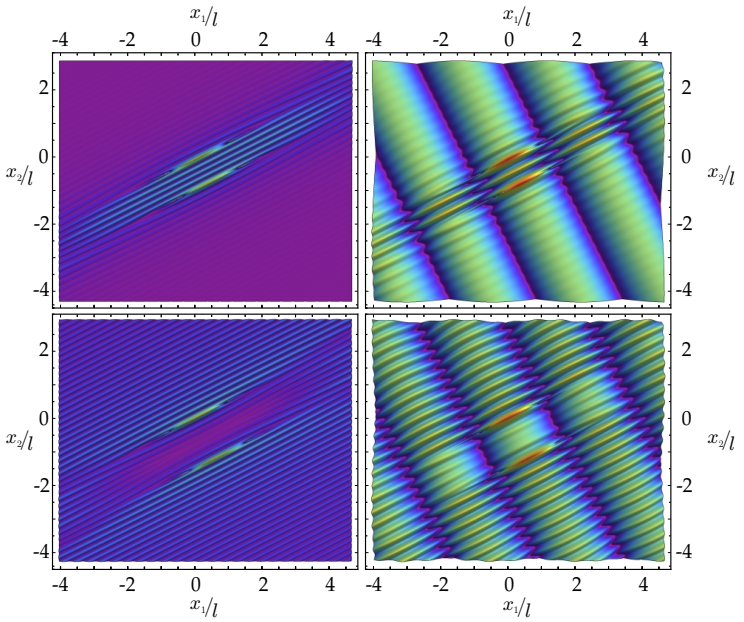

FIGURE 1.2: Examples of wave focusing (upper part) and shielding (lower part) generated by two parallel shear bands. Scattered (left) and total (right) incremental deviatoric strain field is reported as produced by an incident shear wave travelling parallel to the shear bands ($\beta = \theta$) with wave number $\Omega\, l/c_1 = 1$.
.

2 The incremental constitutive equations for incompressible plane strain

In this Chapter, the set of equations that characterise the problem of the incremental nonlinear elasticity upon which the present thesis is focussed, is briefly illustrated. The analysis of strain localizations, in the form of shear bands, can be only analyzed by the using of the incremental elasticity due to the large strains involved.

To this purpose, the Biot problem [10] has been chosen, in which an infinite medium is homogeneously and biaxially deformed within the elliptic range. The current configuration is plane strain and characterized by two in-plane stretches. The incremental response of this incompressible solid is linear and governed by the two Biot moduli, which are functions of the in-plane stretches.

2.1 The incremental constitutive equation

Biot has provided a general procedure for deriving the incremental response of an elastic incompressible material, starting from the constitutive equation expressed in terms of the Cauchy stresses $\boldsymbol{\sigma}$ and the

Cauchy-Green left tensor $\mathbf{B} = \mathbf{F}\mathbf{F}^T$, as

$$\boldsymbol{\sigma} = -q\mathbf{I} + \beta_0\mathbf{B} + \beta_1\mathbf{B}^{-1}, \tag{2.1}$$

in which q is function of the hydrostatic pressure $\hat{p} = \text{tr}\boldsymbol{\sigma}/3$ with the relation

$$q = -\hat{p} + \frac{1}{3}\beta_0 I_1 + \frac{1}{6}\beta_1\left(I_1^2 - I_2\right), \quad I_1 = \text{tr}\mathbf{B}, \quad I_2 = \text{tr}\mathbf{B}^2, \tag{2.2}$$

and β_0 and β_1 are generic functions of the two invariants (I_1, I_2) of $\mathbf{B}$

$$\beta_0 = \beta_0(I_1, I_2), \qquad \beta_1 = \beta_1(I_1, I_2). \tag{2.3}$$

The constitutive equation (2.1) implies the coaxiality between tensors $\mathbf{B}$ and $\boldsymbol{\sigma}$, so that they share a principal reference system where

$$\text{diag}\mathbf{B} = (\lambda_1^2, \lambda_2^2, \lambda_3^2), \qquad \text{diag}\boldsymbol{\sigma} = (\sigma_1, \sigma_2, \sigma_3), \tag{2.4}$$

in which σ_i are the principal stresses and $\lambda_i > 0$ are the principal stretches that satisfy the incompressibility constraint

$$\lambda_1\lambda_2\lambda_3 = 1. \tag{2.5}$$

Consequently, terms β_0 and β_1 of equation (2.1) can be determined in the principal Eulerian reference system as follows

$$\beta_0 = \frac{1}{\lambda_1^2 - \lambda_2^2}\left[\frac{(\sigma_1 - \sigma_3)\lambda_1^2}{\lambda_1^2 - \lambda_3^3} - \frac{(\sigma_2 - \sigma_3)\lambda_2^2}{\lambda_2^2 - \lambda_3^2}\right] \tag{2.6}$$

and

$$\beta_1 = \frac{1}{\lambda_1^2 - \lambda_2^2}\left[\frac{\sigma_1 - \sigma_3}{\lambda_1^2 - \lambda_3^3} - \frac{\sigma_2 - \sigma_3}{\lambda_2^2 - \lambda_3^2}\right] \tag{2.7}$$

Biot [10] has shown that the most general incremental response of a hyperelastic incompressible material deformed in plane strain can be characterized in terms of the Zaremba-Jaumann derivative of the Cauchy stress $\overset{\nabla}{\boldsymbol{\sigma}}$,

$$\overset{\nabla}{\boldsymbol{\sigma}} = \dot{\boldsymbol{\sigma}} - \mathbf{W}\boldsymbol{\sigma} + \boldsymbol{\sigma}\mathbf{W}, \tag{2.8}$$

(where $\mathbf{W}$ is the incremental rotation tensor and $\dot{\boldsymbol{\sigma}}$ is the increment of Cauchy stress) as

$$\overset{\nabla}{\sigma}_{11} - \overset{\nabla}{\sigma}_{22} = 2\mu_* \left(D_{11} - D_{22}\right), \qquad \overset{\nabla}{\sigma}_{12} = 2\mu D_{12}, \tag{2.9}$$

where, in an updated Lagrangean description (in which the current state is used as reference), D_{ij} are the in-plane components of the Eulerian strain increment tensor $\mathbf{D}$, which has to satisfy the incompressibility constraint $\mathrm{tr}\mathbf{D} = 0$, and μ and μ_* are two incremental shear moduli, respectively parallel and inclined at 45° with respect to the x_1-axis [4], and they can be expressed as functions of the principal stretches

$$\mu = \frac{\lambda_1^2 + \lambda_2^2}{2}\left(\beta_0 - \frac{\beta_1}{\lambda_1^2\lambda_2^2}\right). \tag{2.10}$$

and

$$\begin{aligned}\mu_* = \frac{\lambda_1^2 + \lambda_2^2}{2}\beta_0 + \frac{\lambda_1^2 - \lambda_2^2}{4}\left(\lambda_1^2\frac{\partial\beta_0}{\partial\lambda_1} - \lambda_2^2\frac{\partial\beta_0}{\partial\lambda_2}\right) \\ - \frac{1}{\lambda_1^2\lambda_2^2}\left[\frac{\lambda_1^2 + \lambda_2^2}{2}\beta_1 + \frac{\lambda_1^2 - \lambda_2^2}{4}\left(\lambda_1^2\frac{\partial\beta_1}{\partial\lambda_1} - \lambda_2^2\frac{\partial\beta_1}{\partial\lambda_2}\right)\right]\end{aligned} \tag{2.11}$$

In terms of the unsymmetric nominal stress increment $\dot{\mathbf{t}}$, related to the Zaremba-Jaumann derivative of the Cauchy stress as

$$\dot{\mathbf{t}} = \overset{\nabla}{\boldsymbol{\sigma}} - \boldsymbol{\sigma}\mathbf{W} - \mathbf{D}\boldsymbol{\sigma}, \tag{2.12}$$

the constitutive equations (2.8), together with the incompressibility constraint, can be rewritten as

$$\dot{t}_{ij} = \mathbb{K}_{ijkl}v_{l,k} + \dot{p}\delta_{ij}, \quad v_{i,i} = 0, \tag{2.13}$$

where, v_i is the incremental displacement, $\dot{p}$ is the incremental hydrostatic stress and δ_{ij} is the Kronecker delta (indices range between 1 and 2, a comma denotes partial differentiation). The fourth-order tensor $\mathbb{K}_{ijkl}$ of the instantaneous moduli, posseses the major symmetry $\mathbb{K}_{ijkl} = \mathbb{K}_{klij}$

(but not the two minor symmetries), and is defined in components as

$$\begin{array}{lll} \mathbb{K}_{1111} = \mu_* - \dfrac{\sigma}{2} - p, & \mathbb{K}_{1122} = -\mu_*, & \mathbb{K}_{1112} = \mathbb{K}_{1121} = 0, \\ \mathbb{K}_{2211} = -\mu_*, & \mathbb{K}_{2222} = \mu_* + \dfrac{\sigma}{2} - p, & \mathbb{K}_{2212} = \mathbb{K}_{2221} = 0, \\ \mathbb{K}_{1212} = \mu + \dfrac{\sigma}{2}, & \mathbb{K}_{1221} = \mathbb{K}_{2112} = \mu - p, & \mathbb{K}_{2121} = \mu - \dfrac{\sigma}{2}, \end{array} \tag{2.14}$$

where the prestress parameters σ and p are the in-plane deviatoric and mean stresses, functions of the principal Cauchy stresses, respectively, as

$$\sigma = \sigma_1 - \sigma_2, \qquad p = \frac{\sigma_1 + \sigma_2}{2}, \tag{2.15}$$

so that, the components of equation (2.13) in the explicit form are

$$\begin{array}{rcl} \dot{t}_{11} &=& \left(2\mu_* - \dfrac{\sigma}{2} - p\right) v_{1,1} + \dot{p}, \\ \dot{t}_{12} &=& (\mu - p) v_{1,2} + \left(\mu + \dfrac{\sigma}{2}\right) v_{2,1}, \\ \dot{t}_{21} &=& (\mu - p) v_{2,1} + \left(\mu - \dfrac{\sigma}{2}\right) v_{1,2}, \\ \dot{t}_{22} &=& \left(2\mu_* + \dfrac{\sigma}{2} - p\right) v_{1,1} + \dot{p}. \end{array} \tag{2.16}$$

Introducing the dimensionless measure of the deviatoric pre-stress k and the dimensionless parameter quantifying the amount of orthotropy ξ, defined as

$$k = \frac{\sigma}{2\mu}, \qquad \xi = \frac{\mu_*}{\mu}, \tag{2.17}$$

the components (2.16) can be rewritten as

$$\begin{array}{rcl} \dot{t}_{11} &=& (2\mu_* - p)\, v_{1,1} + \dot{\pi}, \\ \dot{t}_{12} &=& (\mu - p) v_{1,2} + (\mu + \mu k)\, v_{2,1}, \\ \dot{t}_{21} &=& (\mu - p) v_{2,1} + (\mu - \mu k)\, v_{1,2}, \\ \dot{t}_{22} &=& -(2\mu_* - p)\, v_{1,1} + \dot{\pi}, \end{array} \tag{2.18}$$

where $\dot{\pi}$ is the in-plane hydrostatic nominal stress increment defined as

$$\dot{\pi} = \frac{\dot{t}_{11} + \dot{t}_{22}}{2} = \dot{p} - \frac{\dot{\sigma}_1 - \dot{\sigma}_2}{2} v_{1,1}. \tag{2.19}$$

The constitutive equations (2.13)–(2.14) are representative of a broad class of material behaviours, including all possible elastic incompressible materials which are orthotropic with respect to the current principal stress directions.

2.2 Local uniqueness and stability criteria for Biot plane strain and incompressibility elasticity

Positive definiteness of $\mathbb{K}$

The uniqueness of the solution is given by the positive definiteness of $\mathbb{K}$ that, for all velocity gradient and under the incompressibility constraint, can be written as

$$v_{j,i}\mathbb{K}_{ijkl}v_{l,k} > 0 \tag{2.20}$$

which can be developed and written in the form

$$\begin{aligned}(\mathbb{K}_{1111} - 2\mathbb{K}_{1122} + \mathbb{K}_{2222})v_{1,1}^2 \\ + \mathbb{K}_{2121}v_{1,2}^2 + 2\mathbb{K}_{1221}v_{1,2}v_{2,1} + \mathbb{K}_{1212}v_{2,1}^2 > 0,\end{aligned} \tag{2.21}$$

and corresponds to the Hill and Hutchinson exclusion condition. Since all components of the velocity gradients of equation (2.21) are free parameters, the conditions to hold are

$$\mathbb{K}_{1111} - 2\mathbb{K}_{1122} + \mathbb{K}_{2222} > 0, \qquad \mathbb{K}_{1212} > 0, \qquad \mathbb{K}_{1212}\mathbb{K}_{2121} - \mathbb{K}_{1221}^2 > 0, \tag{2.22}$$

which, using the definition of the fourth-order tensor $\mathbb{K}$ (2.14), reduce to

$$0 < \sigma_1 + \sigma_2 < 4\mu_* \qquad \frac{\sigma_1^2 + \sigma_2^2}{\sigma_1 + \sigma_2} < 2\mu. \tag{2.23}$$

So that, for a positive prestress ($k > 0$) every incremental bifurcation is excluded (for $\mu > 0$), and can be summarize in a dimensionless form as

$$0 < p/\mu < 2\xi, \qquad \frac{k^2 + (p/\mu)^2}{2\,p/\mu} < 1. \tag{2.24}$$

Strong ellipticity and ellipticity

Strain localization is explained in terms of ellipticity loss and it could lead to shear band formation. Considering the elastic fourth-order tensor, strong ellipticity corresponds to the positive definiteness of its eigenvalues, while ellipticity corresponds to the non vanishing of the same eigenvalues.
Introducing $\mathbf{n}$ and $\mathbf{g}$, two unit vectors orthogonal to each other, with components

$$\mathbf{n} = \{\cos\gamma, \sin\gamma\}, \qquad -\mathbf{g} = \{-\sin\gamma, \cos\gamma\}, \tag{2.25}$$

in which γ is the angle between $\mathbf{n}$ and the x_1 axis, the strong ellipticity condition is expressed as

$$g_j\, n_i\, \mathbb{K}_{ijkl}\, n_k\, g_l > 0, \tag{2.26}$$

or in an expanded form

$$\begin{aligned}\mathbb{K}_{1212}\cos^4\gamma + \mathbb{K}_{2121}\sin^4\gamma \\ + (\mathbb{K}_{1111} - 2\mathbb{K}_{1122} - 2\mathbb{K}_{1221} + \mathbb{K}_{2222})\cos^2\gamma\sin^2\gamma > 0\end{aligned} \tag{2.27}$$

that holds for every γ, and with the definition of $\mathbb{K}$ (2.14), can be rewritten as

$$\mu\sin^4\gamma\left[(1+k)\cot^4\gamma + 2(2\xi - 1)\cot^2\gamma + 1 - k\right] > 0, \tag{2.28}$$

which is equivalent to the following three inequalities:

$$\mu > 0, \qquad k^2 < 1, \qquad 2\xi > 1 - \sqrt{1 - k^2}. \tag{2.29}$$

Then assuming $\mu > 0$ the ellipticity and strong ellipticity criteria are equivalent. The inclination γ of the normal vector of the shear band (introduced in the next Chapter), is obtained from equation (2.28) at the ellipticity loss.

Surface bifurcation

Let us consider an elastic half-space defined in the region $x_2 \leq 0$, and homogeneously pre-stressed; the surface instability [4, 42] occurs in the elliptic regime when the following relation is satisfied

$$4\xi - 2p/\mu = \frac{(p/\mu)^2 - 2p/\mu + k^2}{\sqrt{1-k^2}}. \tag{2.30}$$

The surface instability can be considered a local instability criterion, and is always possible in a nonlinear elastic pre-stressed half space before loss of ellipticity. In the special case, when surface instability occurs at the elliptic boundary, this means that it occurs simultaneously with a shear band formation.

2.3 The regime classification

Let us now consider the superimposition of incremental deformations, at an arbitrary stage of a homogeneous, plane deformation of an infinite medium, by application of a time-harmonic incremental body force $\dot{f}_j$. While the current state of stress trivially satisfies equilibrium, the equations of the incremental motion are

$$\dot{t}_{ij,i} + \dot{f}_j \delta(\mathbf{x}) = \rho \frac{\partial^2 v_j}{\partial t^2}, \tag{2.31}$$

where ρ is the mass density, $\delta(\mathbf{x})$ is the Dirac delta function, and t denotes the time. For time-harmonic motion with circular frequency Ω, and incremental displacement field
$v_i(\mathbf{x}) \exp(-i\Omega t)$, equations (2.31) with the substitution of equation (2.13)

becomes

$$(2\mu_* - \mu)\, v_{1,11} + \left(\mu - \frac{\sigma}{2}\right) v_{1,22} + \dot{f}_1 \delta(\mathbf{x}) = -\dot{\pi}_{,1} - \rho\Omega^2\, v_1, \qquad (2.32)$$

$$(2\mu_* - \mu)\, v_{2,22} + \left(\mu + \frac{\sigma}{2}\right) v_{2,11} + \dot{f}_2 \delta(\mathbf{x}) = -\dot{\pi}_{,2} - \rho\Omega^2\, v_2. \qquad (2.33)$$

The incremental displacement field can be derived from a stream function $\psi(\mathbf{x})\exp(-i\Omega t)$, introduced as

$$v_1 = \psi_{,2}, \quad v_2 = -\psi_{,1}. \qquad (2.34)$$

A differentiation of the two equations (2.32) and (2.33) with respect to x_2 and x_1, respectively, and subtracting the results, yields the differential equation

$$(1+k)\,\psi_{,1111} + 2\,(2\xi - 1)\,\psi_{,1122} + (1-k)\,\psi_{,2222} + \frac{\dot{f}_{1,2}}{\mu} - \frac{\dot{f}_{2,1}}{\mu} + \\ + \frac{\rho}{\mu}\Omega^2\,(\psi_{,11} + \psi_{,22}) = 0. \qquad (2.35)$$

Localization of deformation is usually identified with the condition of loss of ellipticity of the equations governing incremental equilibrium, and for this reason all the results of the present thesis are restricted to the elliptic regime. The principal part of the differential equation (2.35) is the same as in the quasi-static case and its homogeneous associated equation is

$$(1+k)\,\psi_{,1111} + 2\,(2\xi - 1)\,\psi_{,1122} + (1-k)\,\psi_{,2222} = 0, \qquad (2.36)$$

and dividing by $\mu\,\psi_{,2222}$, assumes the form

$$\mu\psi_{,2222}\left[(1+k)\,\frac{\psi_{,1111}}{\psi_{,2222}} + 2\,(2\xi - 1)\,\frac{\psi_{,1122}}{\psi_{,2222}} + (1-k)\right] = 0. \qquad (2.37)$$

Assuming that the solution has the following structure:

$$\psi(x_1, x_2) = A\exp^{i\,\boldsymbol{\omega}\cdot\mathbf{x}} \qquad (2.38)$$

where $A \in \mathbb{R}$, $\boldsymbol{\omega} \in \mathbb{C}^2$ and $\mathbf{x} \in \mathbb{R}^2$, and substituting its derivatives in equation (2.37), we obtain:

$$\mu\omega_2^4 \left[(1+k)\frac{\omega_1^4}{\omega_2^4} + 2(2\xi - 1)\frac{\omega_1^2}{\omega_2^2} + 1 - k \right] = 0, \tag{2.39}$$

which is strongly related to the inequality (2.28). Equation (2.39) admits:

- four real solutions ω_1/ω_2, in the hyperbolic regime (denoted by H);
- two real solutions ω_1/ω_2, in the parabolic regime (denoted by P);
- no real solutions ω_1/ω_2, in the elliptic regime (denoted by E).

The elliptic regime may be further sub-divided into elliptic complex (EC) and elliptic imaginary (EI) regimes. In particular, equation (2.39) admits:

- two conjugate pairs of complex solutions in the elliptic complex regime (EC), with domain expressed as

$$k^2 < 1 \qquad \text{and} \qquad 1 - \sqrt{1-k^2} < 2\xi < 1 + \sqrt{1-k^2} \tag{2.40}$$

- four purely imaginary solutions (in conjugate pairs) in the elliptic imaginary regime (EI) with domain expressed as

$$k^2 < 1 \qquad \text{and} \qquad 2\xi < 1 + \sqrt{1-k^2}. \tag{2.41}$$

Introducing the roots ω_1^2/ω_2^2 of equation (2.39)

$$(1+k)\frac{\omega_1^4}{\omega_2^4} + 2(2\xi-1)\frac{\omega_1^2}{\omega_2^2} + 1 - k = (1+k)\left[\frac{\omega_1^2}{\omega_2^2} - \gamma_1\right]\left[\frac{\omega_1^2}{\omega_2^2} - \gamma_2\right], \tag{2.42}$$

where

$$\left.\begin{matrix}\gamma_1 \\ \gamma_2\end{matrix}\right\} = \frac{1 - 2\mu_*/\mu \pm \sqrt{\Delta}}{1+k}, \quad \text{with} \quad \Delta = k^2 - 4\frac{\mu_*}{\mu} + 4\left(\frac{\mu_*}{\mu}\right)^2. \tag{2.43}$$

it is possible to conclude that:

- γ_1, γ_2 are a conjugate pair in the (EC) regime, with $\Delta > 0$,
- γ_1, γ_2 are both real and negative in the (EI) regime, with $\Delta < 0$

The regime classification, with the superposition of the Hill criterion exclusion and the surface instability, is reported in Figure 2.1 for a J_2-deformation theory of plasticity with hardening exponent $N = 0.4$.

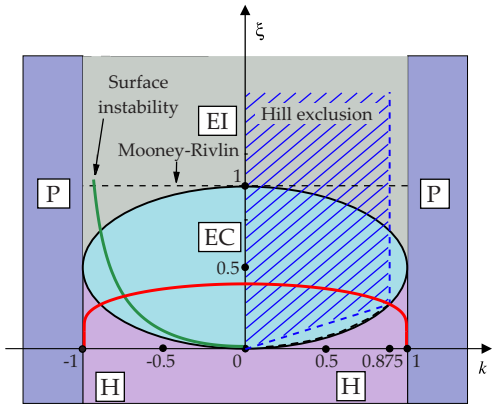

FIGURE 2.1: Regime classifications: in light blue the EC regime, in grey the EI regime, in pink the H regime and in purple the P regime. In continuous red line the J_2-deformation theory path with $N = 0.4$. In blue the Hill exclusion condition (with $p/\mu = 0.59k$ in order to approach the EC/H boundary with the J_2-deformation theory path with $N = 0.4$) and in green the surface instability.

2.4 Mooney-Rivlin material

The Mooney-Rivlin material is defined by the strain energy density function

$$W(\lambda_i) = \frac{\mu_1}{2}\left(\lambda_1^2 + \lambda_2^2 + \lambda_3^2 - 3\right) - \frac{\mu_2}{2}\left(\lambda_1^{-2} + \lambda_2^{-2} + \lambda_3^{-2} - 3\right) \qquad (2.44)$$

in which μ_1 and μ_2 are the two constant moduli. The difference

$$\mu_0 = \mu_1 - \mu_2 > 0 \qquad (2.45)$$

represents the shear modulus in the original unstressed state, which has to be strictly positive.
With reference to equation (2.1) the two functions β_0 and β_1 are constant and are

$$\beta_0 = \mu_1, \qquad \beta_1 = \mu_2, \tag{2.46}$$

and then equation (2.1) can be written as

$$\boldsymbol{\sigma} = -\pi\mathbf{I} + \mu_1\mathbf{B} + \mu_2\mathbf{B}^{-1}. \tag{2.47}$$

The two incremental shear moduli μ and μ_*, respectively parallel and inclined at $45°$ with respect to the x_1-axis, are expressed as

$$\mu = \mu_* = \frac{\mu_0}{2}(\lambda_1^2 + \lambda_2^2). \tag{2.48}$$

If an infinitesimal shear deformation of amplitude γ, parallel to axes $\mathbf{e}_1$ and $\mathbf{e}_2$, and with direction inclined of $\pi/4$ with respect to $\mathbf{e}_1$, is applied to an unloaded solid, the shear stress evaluated from equation (2.47) is

$$\sigma_{12} = \gamma(\mu_1 - \mu_2) = \gamma\mu_0. \tag{2.49}$$

Substituting the stretches for the incompressible deformation $\lambda_1 = \lambda_2 = \lambda$ and $\lambda_3 = 1/\lambda_1^2$ into the strain energy density function, equation (2.44) becomes

$$W(\lambda) = \frac{\mu_1}{2}\left(\frac{2\lambda^6 - 3\lambda^4 + 1}{\lambda^4}\right) - \frac{\mu_2}{2}\left(\frac{\lambda^8 - 3\lambda^4 + 2\lambda^2}{\lambda^4}\right) \tag{2.50}$$

and gives the conclusion that for $\lambda \to 0$ the strain energy W has the sign of μ_1, whereas for $\lambda \to \infty$ the strain energy W has the sign of $-\mu_2$. This leads to the result that $\mu_1 \geq 0$ and $\mu_2 \leq 0$ if we want the strain energy W to be definite positive.

The regime classification introduced in Section 2.2 can be evaluated under the uniaxial strain condition, using the coefficients

$$0 < k = p/\mu < 1, \qquad \xi = 1, \tag{2.51}$$

that satisfy conditions (2.24). Defining the logarithmic strain as

$$\varepsilon_i = \log \lambda_i, \tag{2.52}$$

the loss of ellipticity corresponds to $k = 1$ and then to a corresponding logarithmic strain $\varepsilon_1 = 1.32$. The special case for which the prestress $k = 0$ corresponds to the isotropic condition.

2.5 The J_2–deformation theory of plasticity

In this thesis attention is focused on the behaviour of ductile metals, which can be represented through the J_2-deformation theory of plasticity, whose constitutive equations (Hutchinson and Neale, 1979) in plane strain reduce to

$$\sigma_1 - \sigma_2 = K \left(\frac{2}{\sqrt{3}} \right)^{N+1} |\varepsilon_1|^{N-1} \varepsilon_1, \tag{2.53}$$

where K is a stiffness parameter, $N \in (0, 1]$ a hardening exponent and $\varepsilon_1 = -\varepsilon_2$ are the logarithmic strains, related to the principal stretches $\lambda_1 = 1/\lambda_2$ via $\varepsilon_1 = \log \lambda_1 = -\varepsilon_2 = -\log \lambda_2$. The incremental moduli μ and μ_*, defining equation (2.13), can be written as

$$\mu = \frac{1}{3} E_s \left(\varepsilon_1 - \varepsilon_2\right) \coth \left(\varepsilon_1 - \varepsilon_2\right), \;\; \mu_* = \frac{1}{9} \frac{E_s}{\varepsilon_e^2} \left[3(\varepsilon_1 + \varepsilon_2)^2 + N(\varepsilon_1 - \varepsilon_2)^2 \right], \tag{2.54}$$

where E_s is the secant modulus to the effective-stress/effective-strain curve, given by

$$E_s = K \left(\frac{2}{\sqrt{3}} \right)^{N-1} |\varepsilon_1|^{N-1}. \tag{2.55}$$

Note that the out-of-plane stress increment can be calculated from the expression

$$\overset{\nabla}{\sigma}_{33} = \mathrm{tr}\dot{\boldsymbol{\sigma}}/3 = \dot{p}. \tag{2.56}$$

The regime classification introduced in Section 2.2 can be evaluated in terms of a J_2-deformation theory of plasticity using the coefficients

$$\xi = \frac{N}{2\varepsilon_1 \coth(2\varepsilon_1)}, \qquad k = \frac{1}{\coth(2\varepsilon_1)} \tag{2.57}$$

that satisfy conditions (2.24). The loss of ellipticity corresponds to the equation

$$N = \varepsilon_1^E \tanh \varepsilon_1^E, \tag{2.58}$$

where ε_1^E is the logarithmic strain for the loss of ellipticity.

3 The shear band model

Modelling of a shear band as a slip plane embedded in a highly prestressed material and perturbed by a mode II incremental strain, reveals that a highly inhomogeneous and strongly focussed stress state is created in the proximity of the shear band and aligned parallel to it. This evidence, together with the fact that the incremental energy release rate blows up when the stress state approaches the condition for ellipticity loss, may explain the rectilinear growth of shear bands (documented in several experiments, [24, 30, 65, 66]) and the reason why they are a preferred mode of failure for ductile materials [9, 13, 44, 49, 53].

The aim of the present thesis is to investigate dynamic perturbations in the stress/deformation fields of an incident wave, induced by a shear band of finite length, formed inside a ductile metal, at a certain stage of a continued strain. The shear band is modelled as possessing null thickness and thus behaving as a discontinuity surface, an assumption which is motivated by the experimental observation [50, 59, 69] that thicknesses in metals are on the order of micrometres, while lengths can reach millimeters, so that a thickness-to-length ratio of order 10^{-3} is considered to be negligible.

3.1 The boundary conditions

A shear band of finite length $2l$ is a very thin layer of material subject to intense shear, emerging inside a ductile material at a certain stage of a uniform deformation path with a well-defined inclination θ_0, measured from the σ_1–principal axis of stress.

The shear band is characterized by a high compliance to shear parallel to it, so that it can be modelled by assuming that the incremental nominal traction tangential to the shear band vanishes, while the normal nominal traction and the normal component of the incremental displacement remain continuous. Introducing the jump operator [[ ]] as

$$[[g]] = g^+ - g^-, \tag{3.1}$$

[where g^+ and g^- denote the limits approached by the field $g(\mathbf{x})$ at the discontinuity surface] and two reference systems, namely, $x_1 - x_2$ aligned parallel to the orthotropy axes of the material and $\hat{x}_1 - \hat{x}_2$ aligned parallel to the shear band, Fig. 3.1, the conditions holding along the shear band are the following.

- Null incremental nominal shearing tractions:

$$\hat{t}_{21}(\hat{x}_1, 0^{\pm}) = 0, \quad \forall |\hat{x}_1| < l. \tag{3.2}$$

- Continuity of the incremental nominal traction orthogonal to the shear band:

$$[[\hat{t}_{22}(\hat{x}_1, 0)]] = 0, \quad \forall |\hat{x}_1| < l. \tag{3.3}$$

- Continuity of the incremental displacement component orthogonal to the shear band:

$$[[\hat{v}_2(\hat{x}_1, 0)]] = 0, \quad \forall |\hat{x}_1| < l. \tag{3.4}$$

The above equations show that the shear band is modelled as a (null-thickness) discontinuity surface, which is more general than a crack (because a shear band can carry a finite compressive tractions across its

faces), but may represent a dislocation [2, 67, 68]; in metals the null-thickness assumption is strongly motivated by the experimental observation [50, 59, 69] that a shear band thickness-to-length ratio is of the order 10^{-3} since lengths of shear bands can reach millimetres, while their thickness is confined to only a few micrometres. In the absence of prestress, the shear band model reduces to a weak surface whose faces can freely slide and at the same time are constrained to remain in contact, but when a prestress is present, the shear band model differs from that of a sliding planar surface [5]. The prescriptions (3.2)–(3.4) have been directly borrowed from those defining the onset of a shear band in a material [4].

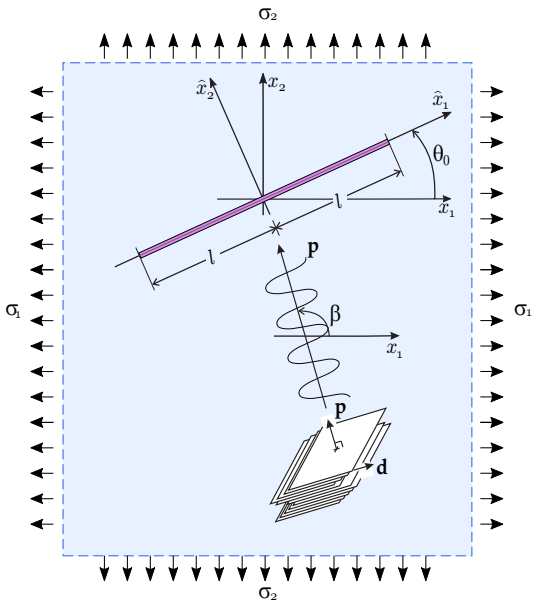

FIGURE 3.1: A plane shear wave (sketched as a moving deck of cards) is impinging a shear band of finite-length ($2l$) in a prestressed, orthotropic material. The shear band (aligned parallel to the $\hat{x}_1$–axis) is inclined at an angle ϑ_0 (positive when anticlockwise) with respect to the orthotropy axes x_1 and x_2 (aligned parallel to the prestress state); the wave is inclined at an angle β with respect to the x_1-axis.

The analysis of the shear band will be restricted to a tensile prestress and the value of the normalized in-plane mean stress, p/μ, will be selected in such a way that the Hill exclusion condition (2.24) is satisfied, so that spurious bifurcations will not affect the dynamics near the shear band, which is analysed as follows.

3.2 The shear band inclination

The inclination γ of the normal vector of the shear band, can be computed from the inequality (2.28), and it is expressed in terms of the shear band inclination with the relation

$$\gamma = \theta_0 + \pi/2. \tag{3.5}$$

For the two different boundaries at the ellipticity loss, the inclination θ_0 results:

- at the EC/H boundary the following relation holds true

  $$k = \text{sign}(k) 2\sqrt{\xi(1-\xi)}, \tag{3.6}$$

  so that, the normal vector of the shear band is inclined at an angle γ, where

  $$\tan^2\gamma = \frac{1 + \text{sign}(k) 2\sqrt{\xi(1-\xi)}}{1-2\xi}. \tag{3.7}$$

  Therefore two shear band are possible with inclinations

  $$\theta_0 = \pm \text{arccot} \sqrt{\frac{1 + 2\,\text{sign}(k)\sqrt{\xi(1-\xi)}}{1-2\xi}}. \tag{3.8}$$

  In the particular case of a J_2-deformation theory of plasticity with hardening exponent $N = 0.4$, the inclination of the shear band is $\theta_0 = 26.7$

- at the EI/P boundary where the condition for positive prestress is

  $$k = 1, \qquad \xi = 1, \tag{3.9}$$

that leads to

$$\gamma = \frac{\pi}{2}, \tag{3.10}$$

so only one shear band can emerge horizontally ($\theta_0 = 0$).

3.3 Non-linear elastic waves

Assuming a time-harmonic motion of circular frequency Ω, a wave characterized by an incremental displacement field $\mathbf{v}^{inc}(\mathbf{x})e^{-i\Omega t}$ travels through the medium and is incident upon the shear band. Then, a scattered incremental displacement field $\mathbf{v}^{sc}(\mathbf{x})e^{-i\Omega t}$ is generated by the interaction of the incident wave with the shear band such that the total incremental displacement field $\mathbf{v}(\mathbf{x})e^{-i\Omega t}$ is represented as the sum

$$\mathbf{v} = \mathbf{v}^{inc} + \mathbf{v}^{sc}. \tag{3.11}$$

The scattered field $\mathbf{v}^{sc}$ must satisfy the radiation condition at infinity and the conditions of energy boundedness near the shear band edge. Outside of the shear band, the incremental displacement field satisfies the equations of motion, which written in terms of the stream function ψ reduces to equation (2.35) with null body force.

The incident wave field is represented by an incremental, time-harmonic plane wave propagating with phase speed c in a direction defined by the unit propagation vector $\mathbf{p}$ [43] and having the form

$$\mathbf{v}^{inc} = A\mathbf{d}e^{i\frac{\Omega}{c}(\mathbf{x}\cdot\mathbf{p}-ct)}, \tag{3.12}$$

where A is the amplitude, $\mathbf{d}$ is the direction of motion and c the wave speed. Since the wave (3.12) propagates in an incompressible material, isochoricity implies

$$\mathbf{d}\cdot\mathbf{p} = 0, \tag{3.13}$$

so that the incident wave is transverse, with the motion orthogonal to the propagation direction. A substitution of equation (3.12) into equation (2.35), written with $\dot{f}_{1,2} = \dot{f}_{2,1} = 0$, and use of equation (3.13) yields the

following expression for the wave speed

$$c^2 = \frac{\mu}{\rho}\left[(1+k)p_1^4 + 2\,(2\xi - 1)\,p_1^2 p_2^2 + (1-k)p_2^4\right], \tag{3.14}$$

which, setting $p_1 = \cos\beta$ and $p_2 = \sin\beta$ and

$$c_1 = \sqrt{\mu(1+k)/\rho}, \tag{3.15}$$

provides

$$c(\beta) = c_1 \sin^2\beta \sqrt{(\cot^2\beta - \gamma_1)\,(\cot^2\beta - \gamma_2)}. \tag{3.16}$$

Note that in the limits $\beta \to 0$ and $\beta \to \pi$, c tends to c_1, which represents the speed of a wave traveling in the direction of the x_1–axis.

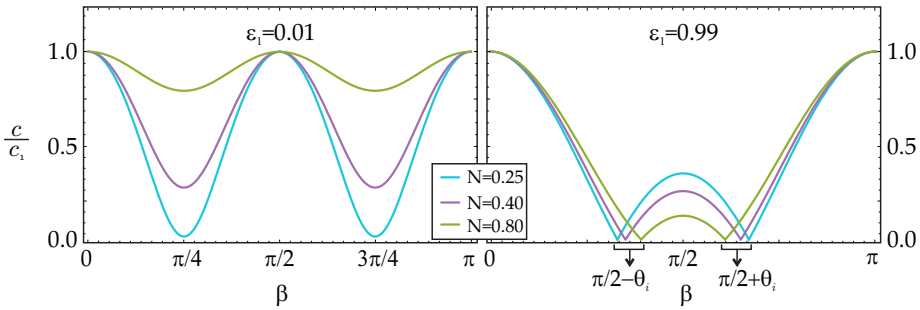

FIGURE 3.2: Dimensionless wave speed as function of the direction of propagation of the wave, for three different hardening exponent of the J_2-deformation theory of plasticity ($N = 0.25$, $N = 0.4$, $N = 0.8$): on the left for a level of prestrain tending to zero, and on the right for a level of prestrain on the elliptic boundary.

The dimensionless wave speed of equation (3.16) is reported in Figure 3.2 as a function of the direction of propagation of the wave.

Results are reported for three different hardening exponent of the J_2-deformation theory of plasticity ($N = 0.25$, $N = 0.4$, $N = 0.8$), and for the higher (right) and lower (left) prestrain ε_1. It is shown that a lower level of prestrain corresponds to a smoother function of the wave speed; at the opposite, for higher prestrain equation (3.16) presents corners in

correspondence of the inclination of the normal vector of the shear band. This means that when the wave travels orthogonal to the shear band, the wavelength and the wave speed tend to zero in correspondence of the elliptic boundary, because material instability occurs, and for this purpose, the numerical analysis of the shear band problem exactly on the elliptic boundary is impossible. The only possibility is to assume being an infinitesimal before the boundary, and in fact, all the results presented in the thesis has been analysed assuming to have a prestrain $\varepsilon_1 = 0.99\,\varepsilon_1^E$.

4 The numerical method

Dynamic effects play an important role on shear band growth and related failure development, most of the analyses conducted so far were limited to quasi-static conditions, while numerical simulations addressing the dynamics of shear bands are scarce (and referred to high strain-rate loading [12, 20, 32, 34, 33, 42, 39, 63, 70]). The incremental behaviour of a pre-stressed, elastic, anisotropic and incompressible material, containing a finite-length shear band of negligible thickness, is analyzed in the dynamic regime. To this purpose, integral representations are derived (under the plane strain condition and assuming ellipticity and homogeneity of the material properties), relating the incremental fields at every point of the medium to the incremental displacement jump across the shear band faces, which originates from an impinging wave.

The integral equations are numerically solved with an *ad hoc* developed collocation method, which allows for the treatment of the singularities present at the tips of the shear bands and provides a basis for the analysis of dynamic disturbances propagating in a solid near the boundary of ellipticity loss. The collocation technique was previously used for crack problems [14, 16, 21, 38, 56, 57, 60], not for shear bands, and presents several advantages when compared with finite element methods (see for instance [12, 33, 39]), the main ones being: (i.) only the boundary of the shear band is discretized; (ii.) an infinite medium can be easily evaluated; (iii.) the radiation damping condition is automatically satisfied, avoiding

spurious wave reflection at fictitious boundaries.

4.1 The time-harmonic Green's function for incremental nonlinear elasticity

The infinite body Green's functions can be found by solving equation (2.35) when the body force is given by the Dirac delta function $\delta(\mathbf{x})$, i.e. $\dot{f}_j\delta(\mathbf{x})$. Introducing a plane wave expansion for the incremental displacement v_i^g of the Green's state

$$v_i^g(\mathbf{x}) = -\frac{1}{4\pi^2}\oint_{|\boldsymbol{\omega}=1|}\tilde{v}_i^g(\boldsymbol{\omega}\cdot\mathbf{x})d\boldsymbol{\omega}, \tag{4.1}$$

where ω is a unit vector with components

$$\omega_1 = \cos(\alpha+\theta), \qquad \omega_2 = \sin(\alpha+\theta) \tag{4.2}$$

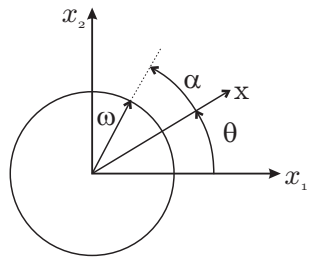

FIGURE 4.1: Reference system, vectors $\boldsymbol{\omega}, \mathbf{x}$ and angles θ and α.

with reference to Figure 4.1, the following representation can be obtained from equation (2.35) in the transformed domain

$$\begin{aligned}\tilde{v}_i^g(\boldsymbol{\omega}\cdot\mathbf{x}) = \; & \frac{(\delta_{1i}\omega_2-\delta_{2i}\omega_1)(\delta_{1g}\omega_2-\delta_{2g}\omega_1)}{L(\boldsymbol{\omega})}\,[\mathrm{Ci}(\eta\mid\boldsymbol{\omega}\cdot\mathbf{x}\mid)\cos(\eta\,\boldsymbol{\omega}\cdot\mathbf{x})+\\ & +\mathrm{Si}(\eta\,\boldsymbol{\omega}\cdot\mathbf{x})\sin(\eta\,\boldsymbol{\omega}\cdot\mathbf{x})-i\frac{\pi}{2}\cos(\eta\,\boldsymbol{\omega}\cdot\mathbf{x})],\end{aligned} \tag{4.3}$$

where Ci and Si are the cosine integral and sine integral functions, respectively, and

$$L(\boldsymbol{\omega}) = \mu(1+k)\omega_2^4 \left(\frac{\omega_1^2}{\omega_2^2} - \gamma_1\right)\left(\frac{\omega_1^2}{\omega_2^2} - \gamma_2\right) > 0, \tag{4.4}$$

with

$$\eta = \Omega\sqrt{\frac{\rho}{L(\boldsymbol{\omega})}}. \tag{4.5}$$

The gradient of the incremental displacement (4.1) can be written as

$$v_{i,k}^g(\mathbf{x}) = -\frac{1}{4\pi^2}\oint_{|\boldsymbol{\omega}|=1} \tilde{v}_{i,k}^g(\boldsymbol{\omega}\cdot\mathbf{x})d\omega \tag{4.6}$$

where

$$\tilde{v}_{i,k}^g(\boldsymbol{\omega}\cdot\mathbf{x}) = \omega_k \frac{\delta_{ig} - \omega_i\omega_g}{L(\boldsymbol{\omega})}\left[\frac{1}{\boldsymbol{\omega}\cdot\mathbf{x}} - \eta\Xi(\eta\boldsymbol{\omega}\cdot\mathbf{x})\right] \tag{4.7}$$

and

$$\Xi(\alpha) = \sin(\alpha)\mathrm{Ci}(|\alpha|) - \cos(\alpha)\mathrm{Si}(\alpha) - i\frac{\pi}{2}\sin(\alpha). \tag{4.8}$$

The plane wave expansion of (2.35) has been developed in [6] and [7]. Finally the Green's function for incremental nominal stresses can be derived from the constitutive equations (2.13) as

$$\begin{aligned} \dot{t}_{11}^g &= (2\mu_* - p)\, v_{1,1}^g + \dot{\pi}^g, & \dot{t}_{12}^g &= (\mu - p)\, v_{1,2}^g + (\mu + \mu k)\, v_{2,1}^g, \\ \dot{t}_{21}^g &= (\mu - p)\, v_{2,1}^g + (\mu - \mu k)\, v_{1,2}^g, & \dot{t}_{22}^g &= -(2\mu_* - p)\, v_{1,1}^g + \dot{\pi}^g. \end{aligned} \tag{4.9}$$

4.2 The boundary integral equation

The scattered field $\mathbf{v}^{sc}$ satisfies the extension of the Betti identity provided in [7, 15]

$$v_g^{sc}(\mathbf{y}) = \int_{\partial B}\left(\dot{t}_{ij}n_i v_j^g(\mathbf{x},\mathbf{y}) - \dot{t}_{ij}^g(\mathbf{x},\mathbf{y})n_i v_j\right) dl_{\mathbf{x}}, \tag{4.10}$$

where ∂B represents the boundary of the shear band, which is made up of two straight lines of length $2l$, with external unit normals of opposite sign, so that equation (4.10) can be specialized for a shear band to

$$v_g^{sc}(\mathbf{y}) = -\int_{-l}^{l} \left([\![\dot{t}_{ij}]\!] n_i v_j^g(\hat{x}_1, \mathbf{y}) - \dot{t}_{ij}^g(\hat{x}_1, \mathbf{y}) n_i [\![v_j]\!] \right) d\hat{x}_1. \tag{4.11}$$

Because the incremental traction is continuous across the shear band, equations (3.2)–(3.3), the following boundary integral equation is obtained

$$v_g^{sc}(\mathbf{y}) = \int_{-l}^{l} \dot{t}_{ij}^g(\hat{x}_1, \mathbf{y}) n_i [\![v_j]\!] \, d\hat{x}_1, \tag{4.12}$$

which provides the incremental displacement at every point in the body as function of the jump of the incremental displacement $[\![v_j]\!]$ across the shear band.

The gradient of the incremental displacement can be evaluated from the integral equation (4.12) as

$$v_{g,k}^{sc}(\mathbf{y}) = -\int_{-l}^{l} \dot{t}_{ij,k}^g(\hat{x}_1, \mathbf{y}) n_i [\![v_j]\!] \, d\hat{x}_1, \tag{4.13}$$

so that from the constitutive equations (2.13) the incremental stress can be written as

$$\dot{t}_{lm}^{sc}(\mathbf{y}) = -\mathbb{K}_{lmkg} \int_{-l}^{l} \dot{t}_{ij,k}^g(\hat{x}_1, \mathbf{y}) n_i [\![v_j]\!] \, d\hat{x}_1 + \dot{p}(\mathbf{y}) \delta_{lm}, \tag{4.14}$$

where the incremental in-plane mean stress $\dot{p}$, for the moment unknown, can be determined from the following boundary integral equation [8]

$$\begin{aligned} \dot{p}(\mathbf{y}) \;=\; & -\int_{\partial B} \dot{t}_{ig}\, n_i\, \dot{p}^g(\mathbf{x}-\mathbf{y})\, dl_x + \int_{\partial B} n_i\, v_j\, \mathbb{K}_{ijkg}\, \dot{p}_{,k}^g(\mathbf{x}-\mathbf{y})\, dl_x \\ & -\int_{\partial B} v_i\, n_i \left[\left(4\mu\mu_* - 4\mu_*^2 + \mu\sigma - 2\mu_*\sigma - \frac{\sigma^2}{2} \right) v_{1,11}^1(\mathbf{x}-\mathbf{y}) \right. \\ & \left. -\sigma \left(\mu + \frac{\sigma}{2} \right) v_{2,11}^2(\mathbf{x}-\mathbf{y}) + \rho\Omega^2 W(\mathbf{x}-\mathbf{y}) \right] dl_x, \end{aligned} \tag{4.15}$$

where $\dot{p}^g$ is the incremental in-plane mean stress of the Green's state

$$\dot{p}^g = \dot{\pi}^g - \frac{\sigma}{2} v^g_{1,1}, \tag{4.16}$$

in which

$$\dot{\pi}^g = \frac{\omega_g(2\mu_* - \mu)(1-\omega_g^2) + (\mu - (\delta_{2g} - \delta_{1g})\frac{\sigma}{2})\omega_g^2}{L(\boldsymbol{\omega})} \left[\frac{1}{\boldsymbol{\omega}\cdot\mathbf{x}} - \eta\Xi(\eta\boldsymbol{\omega}\cdot\mathbf{x})\right] + \omega_g\eta\Xi(\eta\,\boldsymbol{\omega}\cdot\mathbf{x}) \tag{4.17}$$

and

$$\tilde{W} = \left[4\,(\mu - \mu_*)\,\omega_2^2 - \sigma\right] \tilde{v}_2^2(\boldsymbol{\omega}\cdot\mathbf{x}) + \log|\boldsymbol{\omega}\cdot\mathbf{x}|. \tag{4.18}$$

Introducing for ∂B the straight boundary of the shear band, $\hat{x}_1 \in [-l, l]$, equation (4.15) becomes

$$\begin{aligned}\dot{p}(\mathbf{y}) \;=\; & -\int_{\partial B} [[\dot{t}_{ig}]]\, n_i\, \dot{p}^g(\mathbf{x}-\mathbf{y})\, dl_x + \int_{\partial B} n_i\, [[v_j]]\, \mathbb{K}_{ijkg}\, \dot{p}^g_{,k}(\mathbf{x}-\mathbf{y})\, dl_x \\ & -\int_{\partial B} [[v_i]]\, n_i \left[\left(4\mu\mu_* - 4\mu_*^2 + \mu\sigma - 2\mu_*\sigma - \frac{\sigma^2}{2}\right) v^1_{1,11}(\mathbf{x}-\mathbf{y}) \right. \\ & \left. -\sigma\left(\mu + \frac{\sigma}{2}\right) v^2_{2,11}(\mathbf{x}-\mathbf{y}) + \rho\Omega^2 W(\mathbf{x}-\mathbf{y})\right] dl_x,\end{aligned} \tag{4.19}$$

which, considering the continuity of incremental tractions, equations (3.2)–(3.3), and the continuity of the normal component of the incremental displacement across the shear band (3.4) reduces to

$$\dot{p}(\mathbf{y}) = \int_{-l}^{l} n_i\, [[v_j]]\, \mathbb{K}_{ijkg}\, \dot{p}^g_{,k}(\hat{x}_1, \mathbf{y})\, d\hat{x}_1. \tag{4.20}$$

In order to determine the incremental displacement jump $[\![v_j]\!]$, unknown in equation (4.12), the point $\mathbf{y}$ is assumed to approach the shear band boundary. Denoting with $\mathbf{s}$ the unit vector tangent to the shear band, the boundary conditions at the shear band become

$$\mathbf{n}\cdot\dot{\mathbf{t}}^{(sc)}\mathbf{s} = -\mathbf{n}\cdot\dot{\mathbf{t}}^{(inc)}\mathbf{s}, \tag{4.21}$$

so that equation (4.13) can be rewritten as

$$\hat{t}_{21}^{(inc)}(\mathbf{y}) = n_l s_m \mathbb{K}_{lmkg} \int_{-l}^{l} \dot{t}_{ij,k}^{g}(\hat{x}_1, \mathbf{y}) n_i [\![v_j]\!] d\hat{x}_1. \tag{4.22}$$

Equation (4.22) represents the boundary integral formulation for the dynamics of a shear band interacting with an impinging wave. The kernel of the integral equation (4.22) is hypersingular of order r^{-2} as $r \to 0$, being r the distance between field point $\mathbf{x}$ and source point $\mathbf{y}$

$$r = |\mathbf{x} - \mathbf{y}| = \sqrt{(x_1 - y_1)^2 - (x_2 - y_2)^2}. \tag{4.23}$$

Note that the integral on right-hand side of equation (4.22) is specified in the finite-part Hadamard sense.

The solution for an inclined shear band in an infinite medium can be expressed in the inclined reference system sketched in Fig. 3.1.

The components of the vector of incremental displacements $\mathbf{v}$ in the reference system x_1–x_2, can be expressed in the local reference system $\hat{x}_1$–$\hat{x}_2$ as

$$\mathbf{v} = \mathbf{Q}\hat{\mathbf{v}}, \quad [\mathbf{Q}] = \begin{bmatrix} \cos\vartheta & -\sin\vartheta \\ \sin\vartheta & \cos\vartheta \end{bmatrix}, \tag{4.24}$$

so that, due to the boundary conditions (3.4),

$$[\![v_j]\!] = Q_{j1}[\![\hat{v}_1]\!] = s_j[\![\hat{v}_1]\!], \tag{4.25}$$

equation (4.22) can be given the final form

$$\hat{t}_{21}^{(inc)}(\mathbf{y}) = n_l s_m \mathbb{K}_{lmkg} \int_{-l}^{l} \dot{t}_{ij,k}^{g}(\hat{x}_1, \mathbf{y}) n_i s_j [\![\hat{v}_1]\!] d\hat{x}_1, \tag{4.26}$$

showing that the dynamics of a shear band is governed by a linear integral equation in the unknown jump of tangential incremental displacement across the shear band faces, $[\![\hat{v}_1]\!]$. It is worth noting that the gradient of the Green incremental stress tensor, constituting the kernel of the boundary integral equation, turns out to be the sum of a static part $\dot{t}_{ij,k}^{g(st)}$ and a dynamic part $\dot{t}_{ij,k}^{g(dyn)}$, whose expressions are given in Appendix B,

leading to

$$\hat{t}_{21}^{(inc)}(\mathbf{y}) = n_l s_m \mathbb{K}_{lmkg} \int_{-l}^{l} \left(\hat{t}_{ij,k}^{g(st)}(\hat{x}_1, \mathbf{y}) + \hat{t}_{ij,k}^{g(dyn)}(\hat{x}_1, \mathbf{y}) \right) n_i s_j [\![\hat{v}_1]\!] d\hat{x}_1. \tag{4.27}$$

4.3 Discretization and numerical procedure

The treatment of the boundary integral equation (4.27) requires the development of an *ad hoc* numerical procedure, which needs the implementation of a special strategy to enforce the singular behaviour at the band tips, similar to that developed for cracks in [56, 57].

Since both field and source points $\mathbf{x}$ and $\mathbf{y}$ lie on the $\hat{x}_1$–axis, equation (4.26) can be rewritten as

$$\hat{t}_{21}^{(inc)}(\hat{y}) = n_l s_m \mathbb{K}_{lmkg} \int_{-l}^{l} \hat{t}_{ij,k}^{g}(\hat{x}, \hat{y}) n_i s_j [\![\hat{v}]\!](\hat{x})\, d\hat{x}, \tag{4.28}$$

where the index '1' has been dropped, so that $\hat{x}$, $\hat{y}$ and $[\![\hat{v}]\!]$ replace respectively $\hat{x}_1$, $\hat{y}_1$ and $[\![\hat{v_1}]\!]$.

The shear band segment is divided into Q intervals $[\hat{x}_{(q)}, \hat{x}_{(q+1)}]$ $(q = 0, \ldots, Q-1; \hat{x}_{(0)} = -l, ; \hat{x}_{(Q)} = l)$ and a linear variation of the incremental displacement jump $[\![\hat{v}]\!]$ is assumed within each interval, with the exception of the two intervals situated at the shear band tips, where a square root variation of the incremental displacement jump $[\![\hat{v}]\!]$ is adopted:

$$[\![\hat{v}]\!](\hat{x}_{(q)} + \zeta\Delta_q) = [\![\hat{v}]\!]_{(q)}(1-\zeta) + [\![\hat{v}]\!]_{(q+1)}\zeta \quad (q = 1, \ldots, Q-2), \tag{4.29}$$

$$[\![\hat{v}]\!](\hat{x}_{(q)} + \zeta\Delta_q) = [\![\hat{v}]\!]_{(q+1)}\sqrt{\zeta} \quad (q = 0), \tag{4.30}$$

$$[\![\hat{v}]\!](\hat{x}_{(q)} + \zeta\Delta_q) = [\![\hat{v}]\!]_{(q)}\sqrt{1-\zeta} \quad (q = Q-1), \tag{4.31}$$

where $\Delta_q = |\hat{x}_{(q+1)} - \hat{x}_{(q)}|$, $\zeta \in [0,1]$ and $[\![\hat{v}]\!]_{(q)} (q = 1, \ldots, Q-1)$ is the nodal value of the incremental displacement jump (Figure 4.2). The square root variation is adopted to take into account the singularity at the shear band tip, as is usual for the crack tip problem [45, 56, 57, 60].

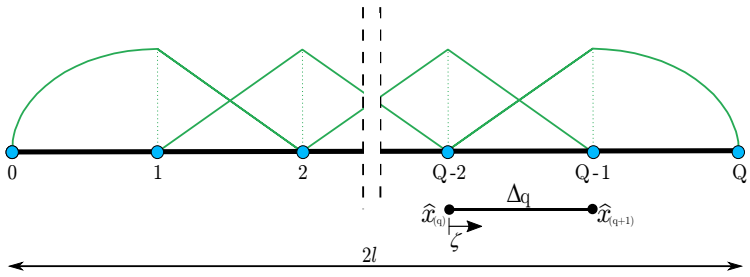

FIGURE 4.2: The shear band line is divided in Q-intervals. Within each interval a linear variation of the incremental displacement jump is assumed, with the exception of the two intervals at the shear band tips.

For a more compact form of the following equations, let us define

$$\tilde{\mathbb{K}}_{lmkgij} = n_l s_m \mathbb{K}_{lmkg} n_i s_j \tag{4.32}$$

When $\hat{y} = \hat{x}_{(p)}\,(p = 1, \ldots, Q-1)$ is assumed to be the source point, the relevant integral equation becomes

$$\begin{aligned}
\hat{t}^{(inc)}_{21}(\hat{x}_{(p)}) &= \tilde{\mathbb{K}}_{lmkgij}\Delta_0 \int_0^1 \dot{t}^g_{ij,k}(\hat{x}_{(0)} + \zeta\Delta_0, \hat{x}_{(p)})\,[\![\hat{v}]\!]_{(1)}\sqrt{\zeta}\,d\zeta \\
&+ \tilde{\mathbb{K}}_{lmkgij}\sum_{q=1}^{p-2}\Delta_q \int_0^1 \dot{t}^g_{ij,k}(\hat{x}_{(q)} + \zeta\Delta_q, \hat{x}_{(p)})([\![\hat{v}]\!]_{(q)}(1-\zeta) + [\![\hat{v}]\!]_{(q+1)}\zeta\,)\,d\zeta \\
&+ \tilde{\mathbb{K}}_{lmkgij}\sum_{q=p-1}^{p}\Delta_q \int_0^1 \dot{t}^g_{ij,k}(\hat{x}_{(q)} + \zeta\Delta_q, \hat{x}_{(p)})([\![\hat{v}]\!]_{(q)}(1-\zeta) + [\![\hat{v}]\!]_{(q+1)}\zeta\,)\,d\zeta \\
&+ \tilde{\mathbb{K}}_{lmkgij}\sum_{q=p+1}^{Q-2}\Delta_q \int_0^1 \dot{t}^g_{ij,k}(\hat{x}_{(q)} + \zeta\Delta_q, \hat{x}_{(p)})([\![\hat{v}]\!]_{(q)}(1-\zeta) + [\![\hat{v}]\!]_{(q+1)}\zeta\,)\,d\zeta \\
&+ \tilde{\mathbb{K}}_{lmkgij}\Delta_{Q-1} \int_0^1 \dot{t}^g_{ij,k}(\hat{x}_{(Q-1)} + \zeta\Delta_{Q-1}, \hat{x}_{(p)})\,[\![\hat{v}]\!]_{(Q-1)}\sqrt{1-\zeta}\,d\zeta.
\end{aligned} \tag{4.33}$$

In equation (4.33), the integrals which are singular for $\hat{x}_{(q)} + \zeta\Delta_q \to \hat{x}_{(p)}$ are relevant to the static kernel $\dot{t}_{12}^{g(st)}$ and can be rearranged as

$$\begin{aligned}
&\sum_{q=p-1}^{p} \Delta_q \int_0^1 \dot{t}_{ij,k}^{g(st)}(\hat{x}_{(q)} + \zeta\Delta_q, \hat{x}_{(p)})(\llbracket\hat{v}\rrbracket_{(q)}(1-\zeta) + \llbracket\hat{v}\rrbracket_{(q+1)}\zeta\,)\,d\zeta \\
&\quad = \Delta_{p-1}\int_0^1 \dot{t}_{ij,k}^{g(st)}(\hat{x}_{(p-1)} + \zeta\Delta_{p-1}, \hat{x}_{(p)})\llbracket\hat{v}\rrbracket_{(p)}\zeta\,d\zeta \\
&\quad +\Delta_p \int_0^1 \dot{t}_{ij,k}^{g(st)}(\hat{x}_{(p)} + \zeta\Delta_p, \hat{x}_{(p)})\llbracket\hat{v}\rrbracket_{(p)}(1-\zeta)\,d\zeta \\
&\quad +\Delta_{p-1}\int_0^1 \dot{t}_{ij,k}^{g(st)}(\hat{x}_{(p-1)} + \zeta\Delta_{p-1}, \hat{x}_{(p)})\llbracket\hat{v}\rrbracket_{(p-1)}(1-\zeta)\,d\zeta \\
&\quad +\Delta_p \int_0^1 \dot{t}_{ij,k}^{g(st)}(\hat{x}_{(p)} + \zeta\Delta_p, \hat{x}_{(p)})\llbracket\hat{v}\rrbracket_{(p+1)}\zeta\,d\zeta,
\end{aligned} \tag{4.34}$$

so that, by means of a change of variable, the integrals can be evaluated as

$$\begin{aligned}
&\sum_{q=p-1}^{p} \Delta_q \int_0^1 \dot{t}_{ij,k}^{g(st)}(\hat{x}_{(q)} + \zeta\Delta_q, \hat{x}_{(p)})(\llbracket\hat{v}\rrbracket_{(q)}(1-\zeta) + \llbracket\hat{v}\rrbracket_{(q+1)}\zeta\,)\,d\zeta \\
&= \int_{-\Delta_{p-1}}^{\Delta_p} \dot{t}_{ij,k}^{g(st)}(r\mathbf{e}_r)\llbracket\hat{v}\rrbracket_{(p)}\,dr - \left(\frac{1}{\Delta_{p-1}} + \frac{1}{\Delta_p}\right)\int_{-\Delta_{p-1}}^{\Delta_p} \dot{t}_{ij,k}^{g(st)}(r\mathbf{e}_r)\llbracket\hat{v}\rrbracket_{(p)}\,r\,dr \\
&\quad -\frac{1}{\Delta_{p-1}}\int_{-\Delta_{p-1}}^{0} \dot{t}_{ij,k}^{g(st)}(r\mathbf{e}_r)\llbracket\hat{v}\rrbracket_{(p-1)}\,r\,dr + \frac{1}{\Delta_p}\int_0^{\Delta_p} \dot{t}_{ij,k}^{g(st)}(r\mathbf{e}_r)\llbracket\hat{v}\rrbracket_{(p+1)}\,r\,dr,
\end{aligned} \tag{4.35}$$

with $\mathbf{e}_r = \mathbf{r}/r$. The non-null finite parts of the above integrals can be calculated as

$$\begin{aligned}
\int_{-\Delta_{p-1}}^{\Delta_p} \dot{t}_{ij,k}^{g(st)}(r\mathbf{e}_r)\llbracket\hat{v}\rrbracket_{(p)}\,dr &= T_{ijk}^{g}(\theta)\left(-\frac{1}{\Delta_{p-1}} - \frac{1}{\Delta_p}\right)\llbracket\hat{v}\rrbracket_{(p)}, \\
-\frac{1}{\Delta_{p-1}}\int_{-\Delta_{p-1}}^{0} \dot{t}_{ij,k}^{g(st)}(r\mathbf{e}_r)\llbracket\hat{v}\rrbracket_{(p-1)}\,r\,dr &= T_{ijk}^{g}(\theta)\frac{\log\Delta_{p-1}}{\Delta_{p-1}}\llbracket\hat{v}\rrbracket_{(p-1)}, \\
\frac{1}{\Delta_p}\int_0^{\Delta_p} \dot{t}_{ij,k}^{g(st)}(r\mathbf{e}_r)\llbracket\hat{v}\rrbracket_{(p+1)}\,r\,dr &= T_{ijk}^{g}(\theta)\frac{\log\Delta_p}{\Delta_p}\llbracket\hat{v}\rrbracket_{(p+1)}
\end{aligned} \tag{4.36}$$

and the function $T_{ijk}^{g}(\theta)$ is explicitly provided in Appendix A.

In the particular cases when $\hat{y} = \hat{x}_{(p)}$ is assumed to be the source point and $p = 1$ or $p = Q-1$, equation (**??**) has to be rewritten as

$$\begin{aligned}
\hat{t}_{21}^{(inc)}(\hat{x}_{(p)}) &= \tilde{\mathbb{K}}_{lmkgij}\Delta_0 \int_0^1 \dot{t}_{ij,k}^{g}(\hat{x}_{(0)} + \zeta\Delta_0, \hat{x}_{(p)})\,[\![\hat{v}]\!]_{(1)}\sqrt{\zeta}\,d\zeta \\
&\quad + \tilde{\mathbb{K}}_{lmkgij}\Delta_1 \int_0^1 \dot{t}_{ij,k}^{g}(\hat{x}_{(1)} + \zeta\Delta_1, \hat{x}_{(p)})([\![\hat{v}]\!]_{(1)}(1-\zeta) + [\![\hat{v}]\!]_{(2)}\zeta\,)\,d\zeta \\
&+ \tilde{\mathbb{K}}_{lmkgij}\sum_{q=2}^{Q-3}\Delta_q \int_0^1 \dot{t}_{ij,k}^{g}(\hat{x}_{(q)} + \zeta\Delta_q, \hat{x}_{(p)})([\![\hat{v}]\!]_{(q)}(1-\zeta) + [\![\hat{v}]\!]_{(q+1)}\zeta\,)\,d\zeta \\
&+ \tilde{\mathbb{K}}_{lmkgij}\Delta_{Q-2} \int_0^1 \dot{t}_{ij,k}^{g}(\hat{x}_{(Q-2)} + \zeta\Delta_{Q-2}, \hat{x}_{(p)})([\![\hat{v}]\!]_{(Q-2)}(1-\zeta) + [\![\hat{v}]\!]_{(Q-1)}\zeta\,)\,d\zeta \\
&\quad + \tilde{\mathbb{K}}_{lmkgij}\Delta_{Q-1} \int_0^1 \dot{t}_{ij,k}^{g}(\hat{x}_{(Q-1)} + \zeta\Delta_{Q-1}, \hat{x}_{(p)})\,[\![\hat{v}]\!]_{(Q-1)}\sqrt{1-\zeta}\,d\zeta.
\end{aligned} \tag{4.37}$$

When $p = 1$, the finite parts of singular integrals can be evaluated as

$$\begin{aligned}
&\Delta_0 \int_0^1 \dot{t}_{ij,k}^{g(st)}(\hat{x}_{(0)} + \zeta\Delta_0, \hat{x}_{(p)})\,[\![\hat{v}]\!]_{(1)}\sqrt{\zeta}\,d\zeta \\
&\qquad\qquad + \Delta_1 \int_0^1 \dot{t}_{ij,k}^{g(st)}(\hat{x}_{(1)} + \zeta\Delta_1, \hat{x}_{(p)})\,[\![\hat{v}]\!]_{(1)}(1-\zeta)\,d\zeta \\
&\quad = T_{ijk}^{g}(\theta)\left(-\frac{9}{8\Delta_0} - \frac{\ln\Delta_0}{2\Delta_0} - \frac{1}{\Delta_1} - \frac{\ln\Delta_1}{\Delta_1}\right)[\![\hat{v}]\!]_{(1)},
\end{aligned} \tag{4.38}$$

while, when $p = Q-1$, the finite parts of the singular integrals can be evaluated as

$$\begin{aligned}
&\Delta_{Q-2} \int_0^1 \dot{t}_{ij,k}^{g(st)}(\hat{x}_{(Q-2)} + \zeta\Delta_{Q-2}, \hat{x}_{(p)})\,[\![\hat{v}]\!]_{(Q-1)}\zeta\,d\zeta \\
&\qquad\qquad + \Delta_{Q-1} \int_0^1 \dot{t}_{ij,k}^{g(st)}(\hat{x}_{(Q-1)} + \zeta\Delta_{Q-1}, \hat{x}_{(p)})\,[\![\hat{v}]\!]_{(Q-1)}\sqrt{1-\zeta}\,d\zeta \\
&= T_{ijk}^{g}(\theta)\left(-\frac{9}{8\Delta_{Q-1}} - \frac{\ln\Delta_{Q-1}}{2\Delta_{Q-1}} - \frac{1}{\Delta_{Q-2}} - \frac{\ln\Delta_{Q-2}}{\Delta_{Q-2}}\right)[\![\hat{v}]\!]_{(Q-1)}.
\end{aligned} \tag{4.39}$$

Hence, using a collocation method, thus assuming $p = 1, \dots, Q-1$, a system of $Q-1$ algebraic equations is obtained which can be written in matrix form as follows

$$\left\{\hat{\mathbf{t}}_{21}^{(inc)}\right\} = [\mathbf{C}]\,\{[\![\hat{\mathbf{v}}]\!]\}\,, \tag{4.40}$$

with $\mathbf{C}$ the matrix of the coefficients.

The nominal shear traction $\hat{t}_{21}^{(inc)}$ generated by a shear wave impinging the shear band can be obtained using equations (2.34) and (2.13) into equation (3.12), thus yielding

$$\begin{aligned}\hat{t}_{21}^{(inc)}(\mathbf{x}) = \tau_0\, e^{i\frac{\Omega}{c}(\mathbf{p}\cdot\mathbf{x}-ct)}\big[&(n_1^2(\eta-1)-(1-k)n_2^2)\cos^2\theta_0\\ &+(n_2^2(\eta-1)+(1+k)n_1^2)\sin^2\theta_0\\ &+n_1n_2(\eta-2\xi)\sin 2\theta_0\big].\end{aligned} \tag{4.41}$$

where $\tau_0 = iA\mu\Omega/c$ is the maximum shear stress acting at the shear wave front in the quasi-static limit, $\Omega \to 0$. For a wave traveling orthogonally to the shear band, equation (4.41) reduces to a positive quantity, at least until strong ellipticity holds true.

4.4 Validation of the numerical procedure

A shear band is discretized with $Q = 100$ line elements and numerically analyzed when inside a ductile metal whose behaviour is described by the J_2-deformation theory of plasticity. A validation of the developed numerical technique can be obtained, in the limit $\Omega \to 0$, by comparing with the analytic solution for the static case provided by Bigoni and Dal Corso [9]. This validation is provided in Figure 4.3, where the modulus of the displacement jump $[\![\hat{v}_1]\!]$ (divided by the semi-length of the shear band) is plotted along the shear band line $\hat{x}_1$. The validation turns out to be excellent, as the analytic solution is superimposed to the numerical solutions, for different values of the hardening exponent N $(0.25, 0.4, 0.5)$, at respective levels of prestrain close to the elliptic boundary $(\varepsilon_1 = 0.522, \varepsilon_1 = 0.667, \varepsilon_1 = 0.771)$.

The convergence of the numerical solution to the static -analytical-solution (developed in [9]) is shown in Figure 4.4, where the (percent) error in the incremental displacement jump $[\![\hat{v}]\!]_q$, evaluated at the middle of the shear band, $\hat{x_1}/l = 0$, is reported as a function of the number of the collocation points Q.

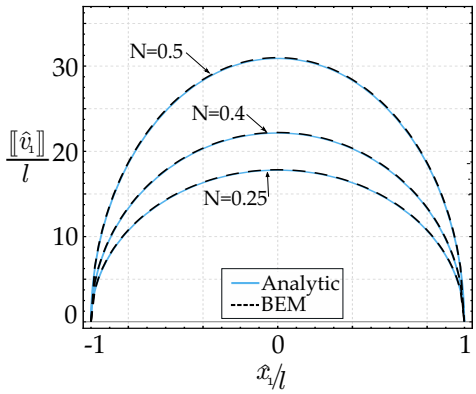

FIGURE 4.3: The quasi-static behaviour of a shear band loaded with a remote shear (obtained numerically in the limit $\Omega \to 0$) is compared with an available analytical solution for different hardening exponents N and prestrains near the elliptic border. Modulus of dimensionless displacement jump along the shear band line, $\hat{x}_1/l$, for the J_2-deformation theory of plasticity and three hardening exponents $N\,(0.25, 0.4, 0.5)$.

Two different sets of shape functions are considered, namely, linear shape functions for the whole shear band in one case (circular spots), while in the other case square-root shape functions are used only in the element at the shear band tip (square spots). It can be seen that in the middle of the shear band for $Q = 100$ the error is about 1% for both shape function sets.

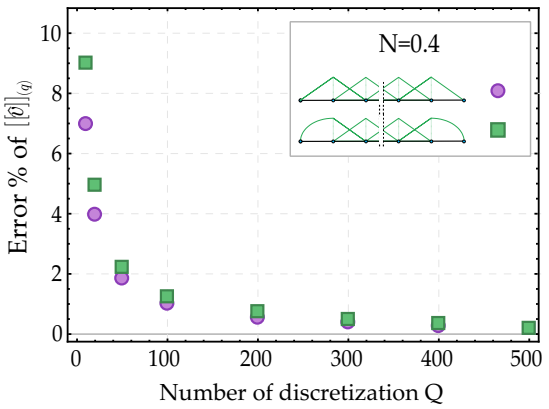

FIGURE 4.4: Percent error in the incremental displacement jump $[\![\hat{v}]\!]_{\hat{q}}$ for different numbers of collocation points $Q\,(10, 20, 50, 100, 200, 500)$, and for two sets of shape functions ($N = 0.4$ has been considered). The errors are evaluated at the middle of the shear band, $\hat{x}_1/l = 0$, note that the circular and square spots are practically superimposed for Q>200.

With $Q = 100$ elements and the selected shape functions, the computing time necessary to find the displacement jump across the shear band ranges between 15 and 20 minutes running the software Mathematica 11.2 in a computer AMD Opteron cluster Stimulus (available at the 'Instability Lab' of the University of Trento).

5 Results for an isolated shear band

In this Chapter results pertaining to an isolated shear band are reported for two different constitutive equations: for a J_2-deformation theory of plasticity with hardening exponent $N = 0.4$, and for a Mooney-Rivlin material.

5.1 Results for the J_2-deformation theory of plasticity

A shear band is discretized with $Q = 100$ line elements and numerically analyzed when inside a ductile metal whose behaviour is described by the J_2-deformation theory of plasticity. The incremental moduli are provided by equations (2.54) and the hardening exponent is assumed to be $N = 0.4$, so that ellipticity is lost at the critical value of the logarithmic strain $\varepsilon_1 \approx 0.678$. Results are presented below.

5.1.1 Wave propagation normal to the shear band

The direction of the wave propagation is now considered to be orthogonal to the shear band faces, so that the whole front of the band is uniformly

loaded. The numerical solution of the linear system (4.40) allows to compute the longitudinal displacement jump across the shear band, $[\![\hat{v}_1]\!]$. The dynamic shape of the displacement jump along the shear band line is reported in Figure 5.1, referred to a prestrain $\varepsilon_1 = 0.667$, close to the boundary of ellipticity loss. This figure shows that, near the resonance frequency, the displacement jump along the shear band assumes the quasi-static shape, but at high frequency displays a markedly different behaviour [37], namely, it decades in amplitude and displays an oscillation (see the pink curve referred to $\Omega l/c_1 = 6$).

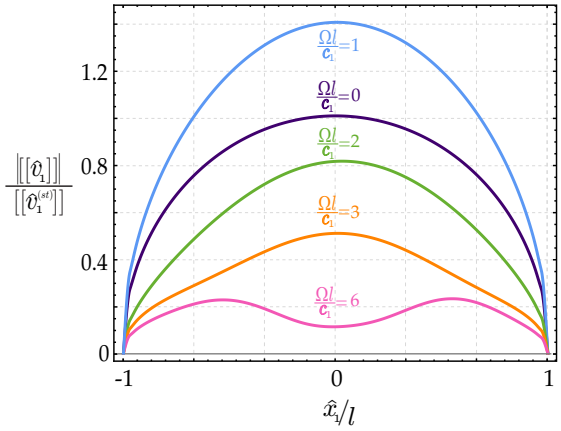

FIGURE 5.1: Modulus of dimensionless displacement jump along the shear band line, $\hat{x}_1/l$, for the J_2-deformation theory of plasticity: different wavenumber are considered with $N = 0.4$ and prestrain $\varepsilon_1 = 0.667$.

The variation with the wavenumber, $\Omega l/c_1$, (of the modulus) of the displacement jump $[\![\hat{v}_1]\!]$ (normalized with respect to the quasi-static value $[\![\hat{v}_1^{(st)}]\!]$) is shown in Figure 5.2 for several values of prestrain, ranging from 0 to $\varepsilon_1 = 0.667$. In this figure the maxima of the curves represent resonance condition (the displacement grows, but does not blow-up to infinity, due to the radiation damping, properly accounted for in the numerical solution), so that it is clear that an increase in the prestrain leads to an amplification factor which grows from 20%, occurring at null prestrain, to 41%, occurring at a prestrain close to the border of ellipticity loss.

Results not reported for brevity show that a decrease in the hardening exponent N shifts the resonance towards higher frequencies.

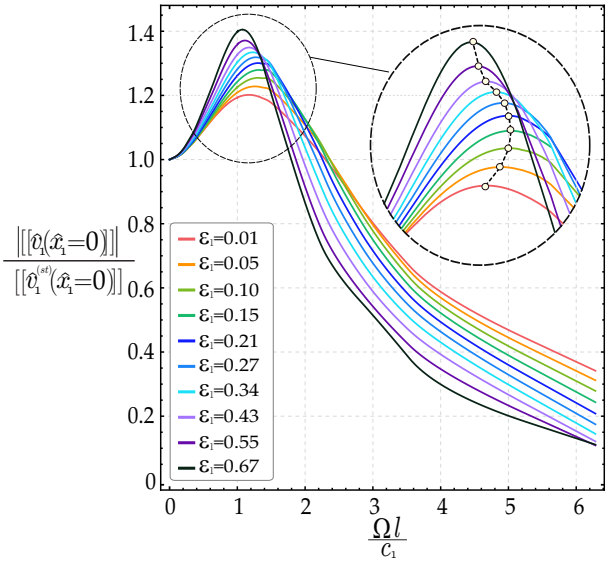

FIGURE 5.2: Modulus of dimensionless displacement jump in the middle of the shear band ($\hat{x}_1 = 0$) is plotted as a function of the dimensionless frequency for different values of prestrain and for the J_2-deformation theory of plasticity with $N = 0.4$ and limit prestrain $\varepsilon_1 = 0.667$ at the EC/H boundary. Note that a resonance frequency is visible (the peak of the curves) and that this resonance becomes more evident at increasing prestrain, when it approaches the elliptic boundary.

The stress concentration at the shear band tips can be investigated using the Stress Intensity Factor (SIF) and because only incremental shear stresses are acting on the band, a Mode II SIF is adopted, which is defined as

$$K_{II} = \lim_{\hat{x}_1 \to l^+} \hat{\dot{t}}_{21}(\hat{x}_1, \hat{x}_2 = 0)\sqrt{2\pi(\hat{x}_1 - l)} \tag{5.1}$$

which in the quasi-static case becomes

$$K_{II}^{st} = \hat{t}_{21}^{\infty}\sqrt{\pi\, l}. \tag{5.2}$$

The SIF is also defined as a function of the displacement jump in the form [3, 18]

$$K_{II} = \frac{\mu\sqrt{2\pi}}{4(1-\nu)} \frac{[\![\hat{v}]\!]_{(1)}}{\sqrt{\Delta_0}}, \tag{5.3}$$

where $[\![\hat{v}]\!]_{(1)}$ is the displacement jump evaluated at the first inner node from the tip of the shear band. Figure 5.3 reports the SIF, K_{II}, normalized through the quasi-static condition $K_{II}^{(st)}$, as a function of the wavenumber.

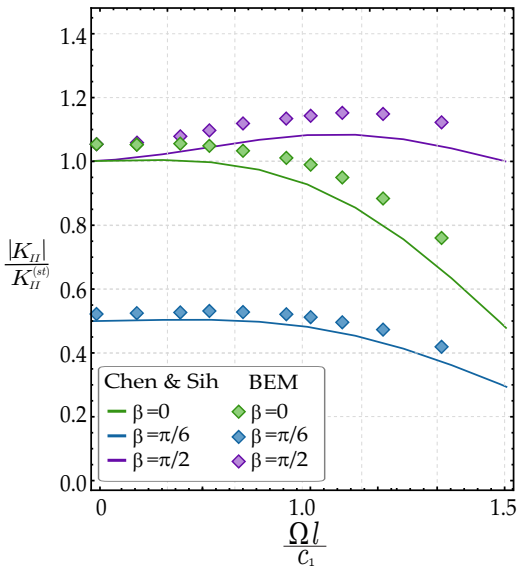

FIGURE 5.3: Modulus of dimensionless mode II Stress Intensity Factor at the shear band tip as a function of the wavenumber; a comparison with the analytical solution of Chen and Sih [17], with null prestrain in the isotropic case with $\mu = \mu_*$.

It has to be noted that Chen and Sih [17] developed an analytical solution for the SIF pertinent to a crack impinged by an incident shear wave in a linear elastic and isotropic body. This solution can be used to validate the developed numerical procedure, as reported in Figure 5.3, relative to a null prestrain. Here the absolute value of the SIF (normalized

with respect to the quasi-static limit) is reported as a function of the wavenumber. The validation turns out to be satisfactory because, for the tested angles β of the wave propagation, the discrepancy is within 8%.

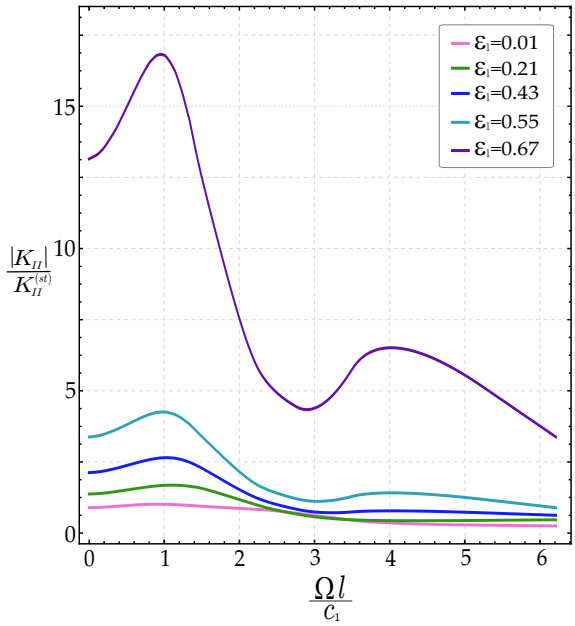

FIGURE 5.4: Modulus of dimensionless mode II Stress Intensity Factor at the shear band tip as a function of the wavenumber for different levels of prestrain for a J_2-deformation theory with $N = 0.4$.

The dimensionless SIF for the shear band tips at different levels of prestrain is reported in Figure 5.4 as a function of the dimensionless frequency. In the quasi-static limit and for a null prestrain the SIF correctly tends to 1, while, when the elliptic boundary is approached, the SIF blows up, reaching a value approximately 15 times the quasi-static value for a prestrain $\varepsilon_1 = 0.66$, whereas at the elliptic border it grows to infinity, coherently with the quasi-static behaviour, [9]. This is once more the evidence of a resonance condition, with an increase of 41% of the SIF with respect to the quasi-static case. It is important to remark that both evidences presented in Fig. 5.2 and 5.4 show that the presence of a shear

band produces a resonance, evidenced through a substantial growth in the jump of displacement across the shear band and in the stress intensity factor at the shear band tip.

5.1.2 Wave propagation inclined or parallel to the shear band

A wave obliquely impinging a shear band is now considered, with $\mathbf{p} \cdot \mathbf{n}$ different from both 0 and 1. The shear traction can be derived from equation (4.41) and is composed of a real symmetric part and an imaginary skew-symmetric part. Therefore, the traction is non-symmetric with respect to the $\hat{x}_2$-axis.

This can be noted in Figure 5.5, where, as in Figure 5.1, the dimensionless displacement jump is reported along the shear band line as a function of the dimensionless frequency, for various inclinations of the wave propagation vector. When the wave propagation is inclined at an angle β belonging to the interval $(-\pi/2 + \theta_0, \pi/2 + \theta_0)$, the maximum value of the displacement jump shifts towards the right tip of the band.

Due to the fact that the wave is now inclined with respect to the shear band, the stress intensity factors at the tips of the shear band are different [62], see Figure 5.6, where the dimensionless SIF for the two tips (one denoted by '+' and the other by '−') are reported as functions of the dimensionless frequency. It can be observed that the higher the displacement jump, the higher is the SIF, moreover a wave orthogonal to the shear band produces the largest value of the SIF and therefore the maximum resonance.

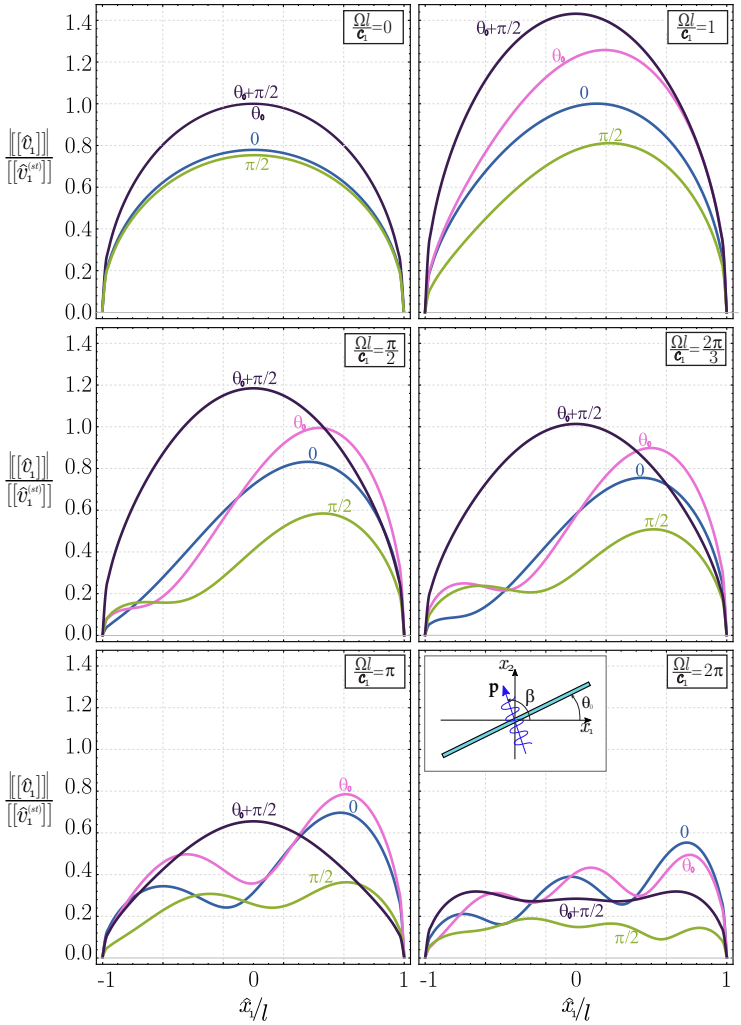

FIGURE 5.5: Modulus of dimensionless displacement jumps (for a J_2-deformation theory of plasticity material with $N = 0.4$) along the shear band line, $\hat{x}_1/l$, at various wavenumber. For each wavenumber, four different inclinations β of the wave propagation are considered $(0, \theta_0, \pi/2, \pi/2 + \theta_0)$.

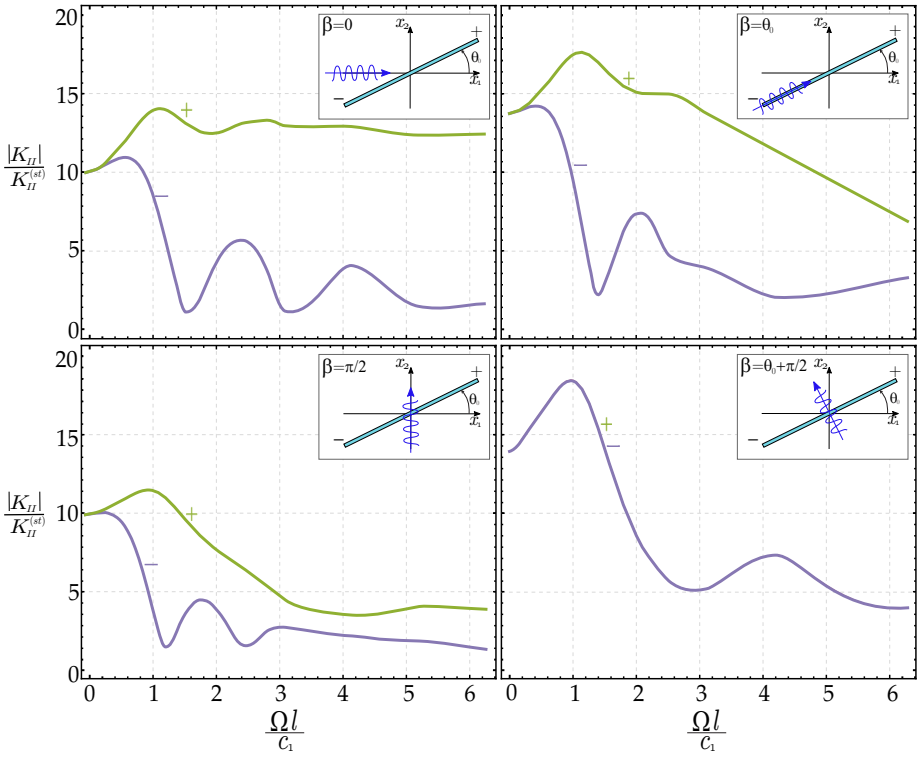

FIGURE 5.6: SIF at the left '−' and right '+' tips of a shear band (in a J_2-deformation theory of plasticity material with $N = 0.4$), for different inclinations β of the wave propagation $(0, \theta_0, \pi/2, \pi/2 + \theta_0)$.

5.1.3 Incremental strain fields

The modulus of the incremental strain field (which is deviatoric, because of incompressibility) defined as $\left(v_{i,j}v_{i,j} + v_{i,j}v_{j,i}\right)/2$, can be computed by using the gradient of the incremental displacement, equation (4.13), in the constitutive equations (2.13). In the following the modulus of the incremental strain field is computed by using the real part of the gradient of incremental displacement, so that the phase shift related to the imaginary part is not considered. The modulus of the incremental strain field, computed at a prestrain level of $\varepsilon_1 = 0.667$ (i.e. close to the elliptic boundary) is reported in Figure 5.7, in terms of scattered wave field (on the left) and in terms of total wave field (on the right). Two incident waves with wavenumber $\Omega l/c_1 = 1$ are considered, one orthogonal to the shear band (with inclination $\beta = \theta_0 + \pi/2$) and the other aligned parallel to the x_1-axis (with inclination $\beta = 0$). These inclinations of propagation represent the directions along which the wave velocity c assumes the minimum and maximum values respectively, see equation (3.16).

It is worth noting that the wavenumber $\Omega l/c_1 = 1$ used for the computations corresponds to a wavelength in the direction orthogonal to the shear band, $2\pi lc/c_1$, which is approximately $1/6$ of the shear band length, thus much greater than the shear band thickness.

It can be noted that for both wave inclinations, the scattered field turns out to be a family of plane waves parallel to the shear band. The effect of this scattered field on the total strain field is to produce a fine texture of parallel vibrations, which superimposes on the impinging wave field. The texture shows a narrow conical shadow zone emanating from the shear band tips, where the scattered field is strongly attenuated and tends to disappear. This effect becomes more visible in the case of $\beta = 0$, because incident and scattered waves propagate in different directions, rather than in the case of wave travels orthogonal to the band. In the case of an incident wave with wavenumber $\Omega l/c_1 = 1$, propagating in the direction parallel to the shear band, Figure 5.8 represents the scattered and total strain fields for three increasing levels of prestrain ($\varepsilon_1 = 0.43, \varepsilon_1 = 0.55, \varepsilon_1 = 0.66$). Starting from the lowest level of prestrain, the unperturbed conical zone is already visible, but this zone tends

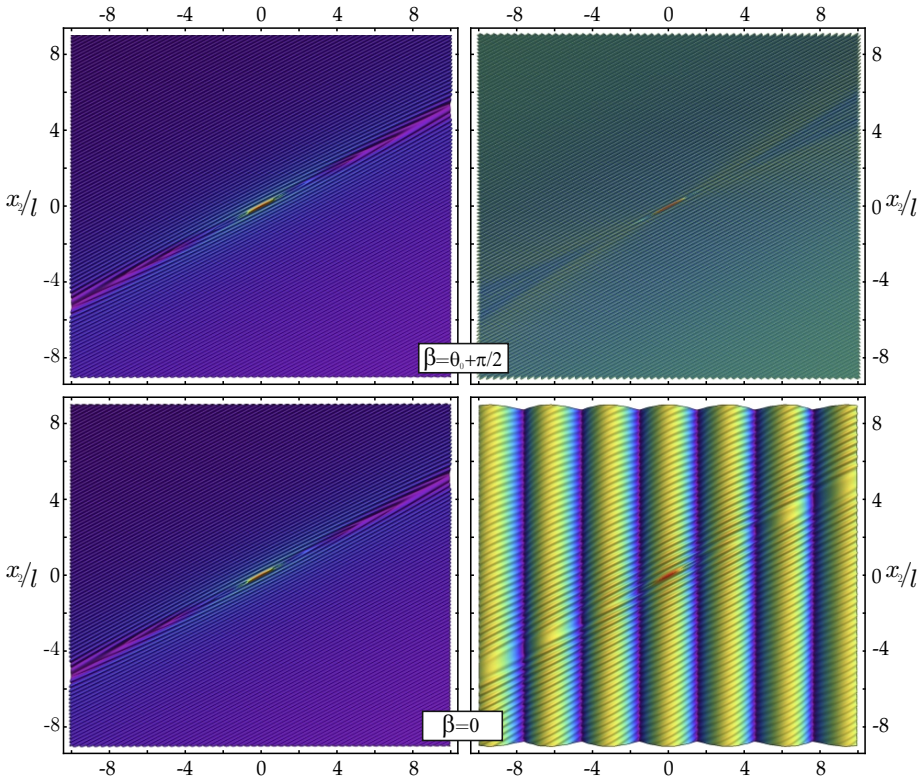

FIGURE 5.7: Scattered (left) and total (right) incremental strain field produced by a wave incident to a shear band (in a J_2-deformation theory of plasticity material with $N = 0.4$) orthogonally to it ($\beta = \theta_0 + \pi/2$) or aligned parallel to the x_1-axis ($\beta = 0$). The wavenumber is $\Omega l/c_1 = 1$ and the level of prestrain is $\varepsilon_1 = 0.667$, close to the elliptic boundary.

to become narrower when the elliptic boundary is approached.

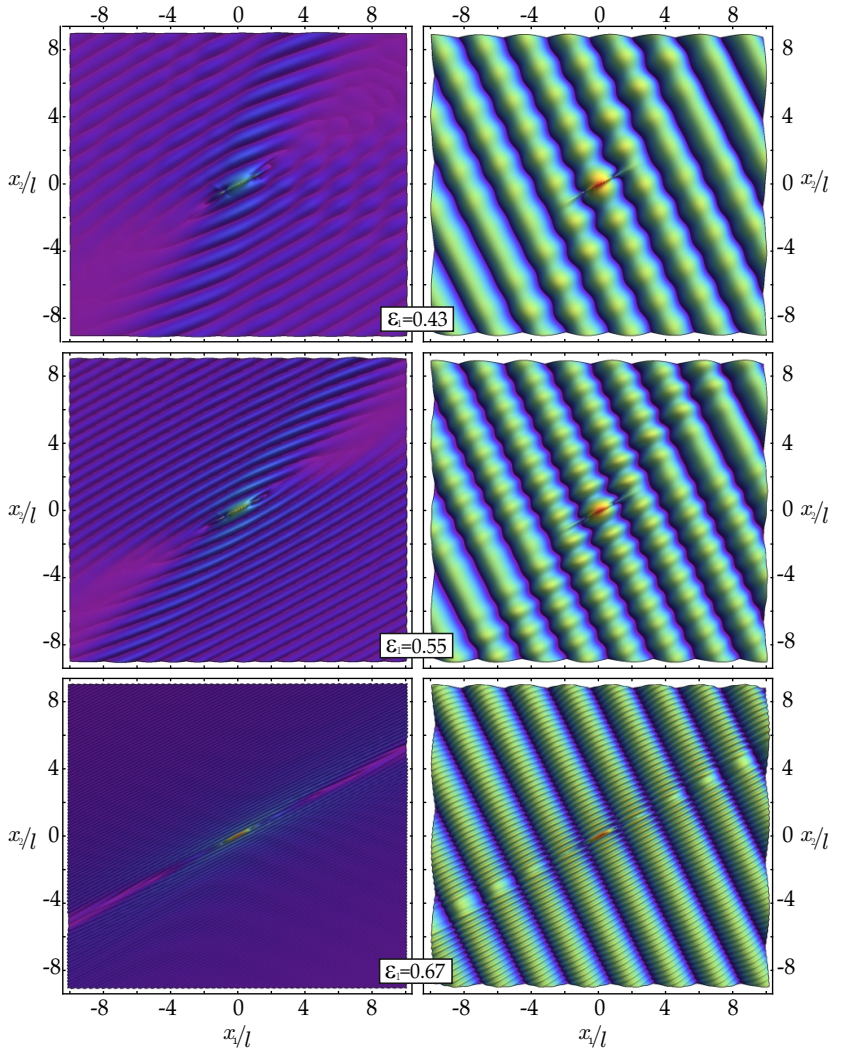

FIGURE 5.8: Scattered (left) and total (right) incremental strain field produced by a wave impinging parallel to a shear band, $\beta = \theta_0$, (in a J_2-deformation theory of plasticity material with $N = 0.4$). Various levels of prestrain $\varepsilon_1 = 0.43, \varepsilon_1 = 0.55, \varepsilon_1 = 0.66$ are reported with wavenumber $\Omega l/c_1 = 1$.

The shadow zone is analyzed near the elliptic boundary as a function of the frequency, in particular, the upper left quarter of the map of the incremental strain field is reported in Figure 5.9 for two frequencies ($\Omega l/c_1 = \pi/5, \Omega l/c_1 = \pi/2$). This plot reveals that the shadow zone becomes more visible at frequencies higher than the value corresponding to resonance.

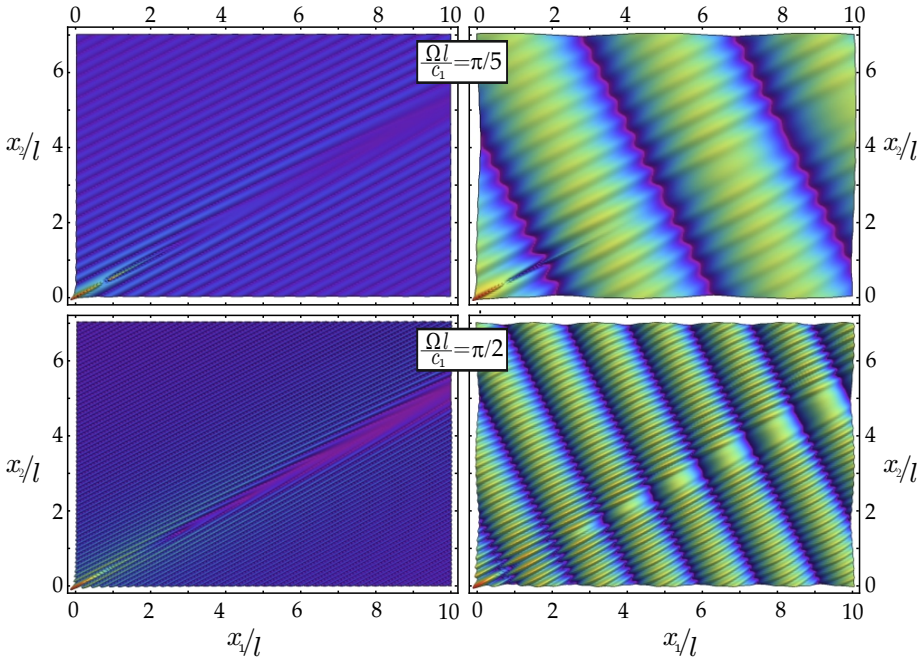

FIGURE 5.9: Incremental strain field near a shear band (in a J_2-deformation theory of plasticity material with $N = 0.4$) produced by a wave impinging parallel to the shear band, $\beta = \theta_0$ and waveleght $\Omega l/c_1 = \pi/5$ (upper part) and $\Omega l/c_1 = \pi/2$ (lower part).

5.2 Results for a Mooney-Rivlin material

A shear band in a Mooney-Rivlin material, emerges and grows parallel to the σ_1-principal axis, with a null inclination, $\theta_0 = 0$. In order to approach the elliptic/parabolic boundary, the limit of the prestress $k \to 1$ (which formally corresponds to infinite stretch) is considered, and for which the ellipticity is lost for a logarithmic strain of $\varepsilon_1 \approx 1.32$.
Due to the inclination $\theta_0 = 0$, the integral equation (4.26) simplifies to

$$\hat{t}_{21}^{(inc)}(\mathbf{y}) = \int_{-l}^{l} \left[(\mu - p)\dot{t}_{21,1}^{2}(\hat{x}_1, \mathbf{y}) + \left(\mu - \frac{\sigma}{2}\right) \dot{t}_{21,2}^{1}(\hat{x}_1, \mathbf{y}) \right] [\![\hat{v}_1]\!] d\hat{x}_1. \tag{5.4}$$

Results pertaining to the Mooney-Rivlin material are close to ones shown for the J_2-deformation theory of plasticity, so only the main results are going to be proposed.
The variation with the wavenumber, $\Omega l/c_1$, (of the modulus) of the displacement jump $[\![\hat{v}_1]\!]$ (normalized with respect to the quasi-static value $[\![\hat{v}_1^{(st)}]\!]$) is shown in Figure 5.10 for several values of prestrain, ranging from 0 to $\varepsilon_1 = 0.99$. In this figure the maxima of the curves represent the resonance condition, so an increase in the prestrain leads to an amplification factor which grows from 20%, occurring at null prestrain, to 41%, occurring at a prestrain close to the border of ellipticity loss as shown before for the J_2-deformation theory of plasticity.

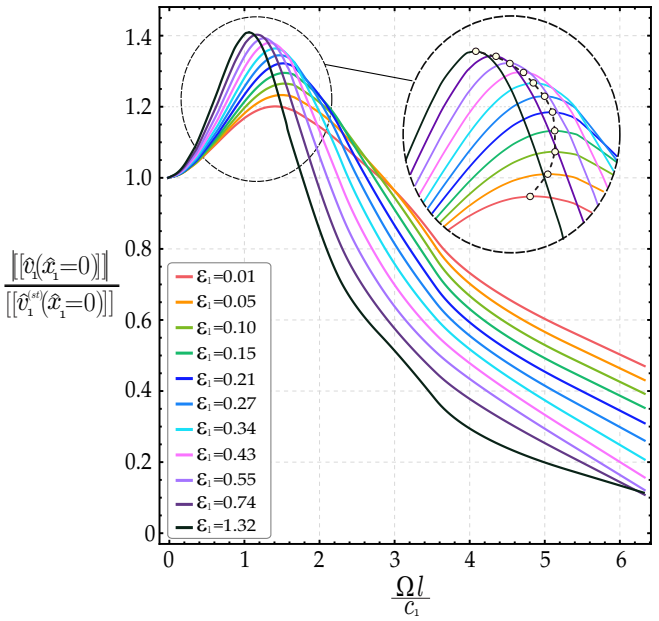

FIGURE 5.10: Modulus of dimensionless displacement jump in the middle of the shear band ($\hat{x}_1 = 0$) is plotted as a function of the dimensionless frequency for different values of prestrain and for the Mooney-Rivlin material and limit prestrain $\varepsilon_1 = 1.32$ at the EI/P boundary. Note that a resonance frequency is visible (the peak of the curves) and that this resonance becomes more evident at increasing prestrain, when it approaches the elliptic boundary.

Figure 5.11 shows the scattered (left part) and total (right part) incremental deviatoric strain fields, for a shear band in a Mooney-Rivlin material at prestress $k = 0.99$, near the elliptic boundary. An incident wave is considered travelling parallel to the shear band ($\beta = 0$), with wavenumber $\Omega l/c_1 = 1$. The emergence of plane waves, parallel to the shear band, can be noted and the formation of a conical shadow zone is visible, which can be compared with the experimental results on wave propagation in a rectangular aluminium block containing a crack prestressed through compressive forces orthogonal to the crack faces [11] (their figure 8).

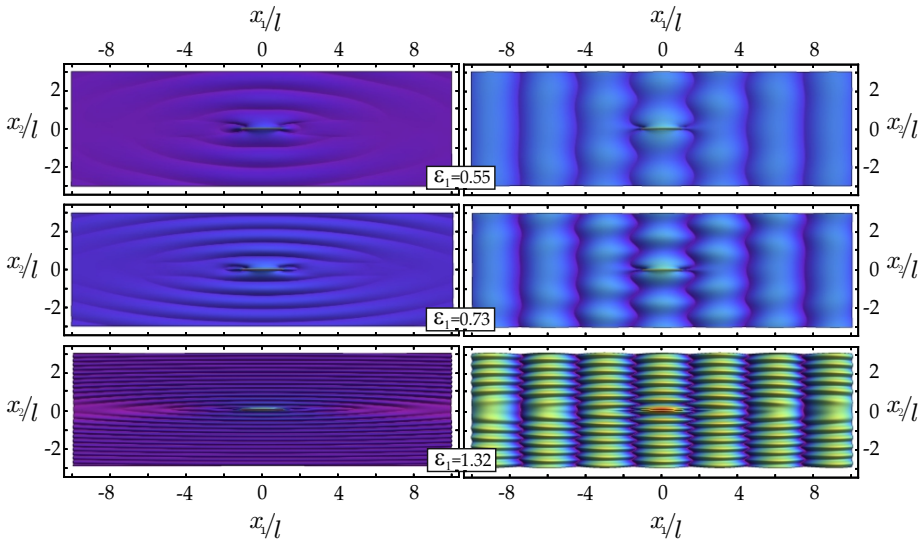

FIGURE 5.11: Scattered (left part) and total (right part) incremental strain field produced by a wave impinging parallel to a shear band, $\beta = \theta_0 = 0$, in a Mooney-Rivlin material. A wavenumber $\Omega l/c_1 = 1$ and a prestress $k = 0.99$ (near the elliptic/parabolic boundary) have been considered.

It is remarked that experimental results on time-harmonic vibration of shear bands are not available in the literature. However, a close scrutiny of experiments on dynamic propagation of shear bands induced by an impact loading reveals that waves propagate in the material with the shear band inclination ([33], their figures 4, 5, 6, and 8), a feature also observed in our simulations (Figures 5.8 and 5.9). Moreover, results relative to wave propagation in highly orthotropic materials exhibit shadow zones similar to those visible in Figure 5.9 ([58], their figure 3). Finally, experiments on wave propagation in an aluminium solid containing a crack with attritive faces, which are prestressed in compression, ([11], their figure 8) can be compared with results pertinent to a Mooney-Rivlin material. In both cases waves parallel to the discontinuity line are evidenced.

6 Multiple shear bands interaction

Interaction between shear bands has been documented so far only for quasi-static deformation processes [20, 25, 28], where it has been shown that different shear band geometries emerge as related to load conditions and material properties of the samples and that parallel [35], aligned, and converging shear bands [51] are frequently observed. In dynamics, results are restricted to high strain-rate loading, where numerical simulations [12, 33, 42] and experiments involving impact on prenotched plates [24, 70, 36] have been presented. In this context, experiments on metallic glass [55] show the development of a complex texture of multiple shear bands, with complex interactions.

Direct experimental investigation on the fine development of shear bands in a material and their effect on the stress field during time-harmonic vibrations remains practically impossible, so that mechanical modelling represents the only possibility to shed light on a complex phenomenon, whose comprehension is a key point for the engineering of materials with enhanced mechanical properties.

A plane-strain model of multiple shear bands, arranged in different configurations, commonly observed in materials and involving two or four shear bands, is introduced, to investigate the dynamical interplay between shear bands and their possible progression or stagnation. Reference is made to low to medium carbon steels, stressed until near the verge of a

plastic instability and subject to incoming harmonic waves of small amplitude. The material is modelled following the J_2-deformation theory of plasticity[4], the shear bands are idealized as discontinuity surfaces [9], and their dynamic interaction is described through an *ad hoc* integral equation formulation, presented together with the relevant numerical method.

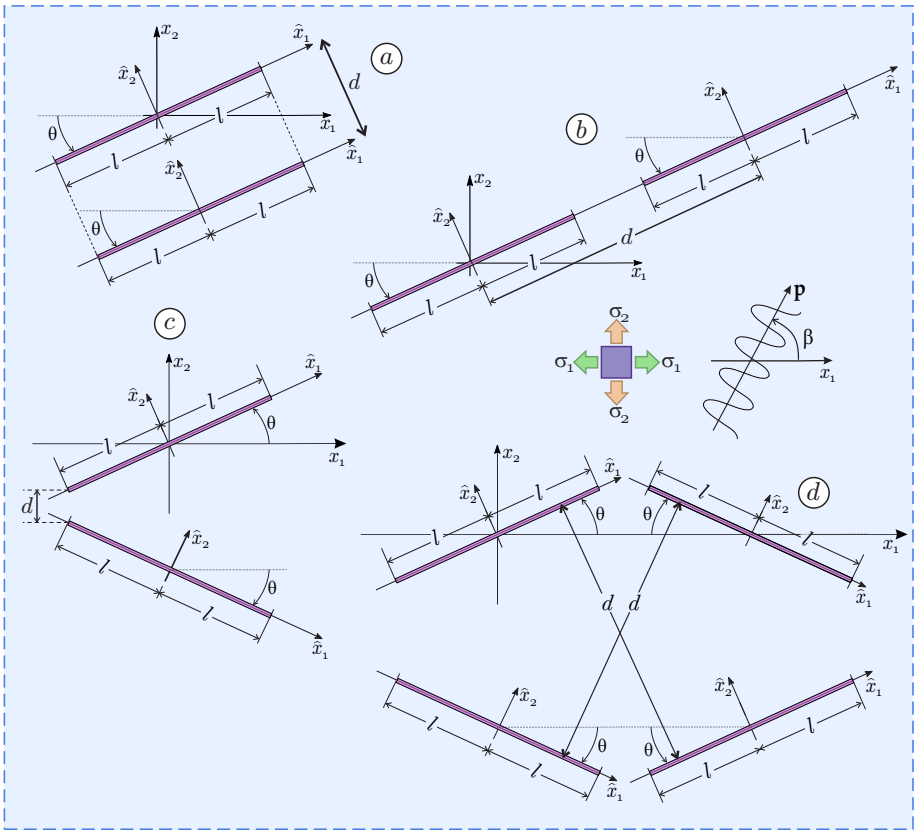

FIGURE 6.1: Waves (inclined at the angle β) impinging on different configurations of shear bands (of equal length $2l$) in a prestressed metal material: (a) parallel, (b) aligned, (c) converging, and (d) involving 4 shear bands.

Since shear bands can emerge and propagate with a definite inclination θ_0, three commonly observed [35, 51] configurations of shear bands

embedded in the material are analyzed, namely, (a) parallel, (b) aligned and (c) converging geometries, arranged as shown in Figure 6.1.

6.1 Boundary integral equation and numerical solution

The boundary integral equation governing the dynamics of a shear band was previously presented in Chapter 4. In the case of multiple shear bands, labelled $A, B, ..., Z$, in order to account for the reciprocal interaction, the equation (4.26) has to be generalized to the following system of integral equations

$$
\begin{aligned}
\hat{t}_{21}^{(inc)}(\mathbf{y}^A) = n_l^A s_m^A \mathbb{K}_{lmkg} \Bigg(& \int_{-l}^{l} t_{ij,k}^{g}(\hat{x}_1^A, \mathbf{y}^A) n_i^A s_j^A [\![\hat{v}_1^A]\!] d\hat{x}_1^A \\
& + \int_{-l}^{l} t_{ij,k}^{g}(\hat{x}_1^B, \mathbf{y}^A) n_i^B s_j^B [\![\hat{v}_1^B]\!] d\hat{x}_1^B \\
& + \cdots + \int_{-l}^{l} t_{ij,k}^{g}(\hat{x}_1^Z, \mathbf{y}^A) n_i^Z s_j^Z [\![\hat{v}_1^Z]\!] d\hat{x}_1^Z \Bigg), \\
\hat{t}_{21}^{(inc)}(\mathbf{y}^B) = n_l^B s_m^B \mathbb{K}_{lmkg} \Bigg(& \int_{-l}^{l} t_{ij,k}^{g}(\hat{x}_1^A, \mathbf{y}^B) n_i^A s_j^A [\![\hat{v}_1^A]\!] d\hat{x}_1^A \\
& + \int_{-l}^{l} t_{ij,k}^{g}(\hat{x}_1^B, \mathbf{y}^B) n_i^B s_j^B [\![\hat{v}_1^B]\!] d\hat{x}_1^B \\
& + \cdots + \int_{-l}^{l} t_{ij,k}^{g}(\hat{x}_1^Z, \mathbf{y}^B) n_i^Z s_j^Z [\![\hat{v}_1^Z]\!] d\hat{x}_1^Z \Bigg), \\
& \cdots \\
\hat{t}_{21}^{(inc)}(\mathbf{y}^Z) = n_l^Z s_m^Z \mathbb{K}_{lmkg} \Bigg(& \int_{-l}^{l} t_{ij,k}^{g}(\hat{x}_1^A, \mathbf{y}^Z) n_i^A s_j^A [\![\hat{v}_1^A]\!] d\hat{x}_1^A \\
& + \int_{-l}^{l} t_{ij,k}^{g}(\hat{x}_1^B, \mathbf{y}^Z) n_i^B s_j^B [\![\hat{v}_1^B]\!] d\hat{x}_1^B \\
& + \cdots + \int_{-l}^{l} t_{ij,k}^{g}(\hat{x}_1^Z, \mathbf{y}^Z) n_i^Z s_j^Z [\![\hat{v}_1^Z]\!] d\hat{x}_1^Z \Bigg),
\end{aligned}
$$

where the generic source point $\mathbf{y}^Z$ is located on the surface of the shear band Z.

Since the kernel $\dot{t}^g_{ij,k}$ of the integral equation is hypersingular of order r^{-2} as $r \to 0$, and the distance r is defined:

- by a field point $\mathbf{x}$ and source point $\mathbf{y}$, both on the same shear band, the hypersingular integrals are considered in the Hadamard finite part sense as shown in Section 4.3;
- by a field point $\mathbf{x}$ that belongs to a shear band and source point $\mathbf{y}$ that belongs to a different shear band, the integral becomes hypersingular when the two shear band are very close. In this particular case, the problem becomes strongly mesh dependent because the linear and square root shape functions introduced before, are not sufficiently stronger to annihilate the singularity on their own.

In order to analyse the interaction of multiple shear bands, without manipulating the hypersingular integrals when the two shear bands are very close, and realize a more general numerical tool, a higher order shape function is needed. For this purpose, in order to describe the square-root singularity[57], two different kinds of shape function have been adopted: quadratic function for the elements interior to the shear band and square-root function (the so called 'quarter-point elements'[18, 56]) at the shear band tips. For the numerical solution, each shear band has been subdivided into a number Q of elements. Using a collocation method, the integral equation system (6.1), can be transformed into the following algebraic system

$$\begin{Bmatrix} \hat{\mathbf{t}}_{21}^{(inc)^A} \\ \hat{\mathbf{t}}_{21}^{(inc)^B} \\ \dots \\ \hat{\mathbf{t}}_{21}^{(inc)^Z} \end{Bmatrix} = \begin{bmatrix} \mathbf{C}_{AA} & \mathbf{C}_{AB} & \dots & \mathbf{C}_{AZ} \\ \mathbf{C}_{BA} & \mathbf{C}_{BB} & \dots & \mathbf{C}_{BZ} \\ \dots & \dots & \dots & \dots \\ \mathbf{C}_{ZA} & \mathbf{C}_{ZB} & \dots & \mathbf{C}_{ZZ} \end{bmatrix} \begin{Bmatrix} [\![\hat{\mathbf{v}}^A]\!] \\ [\![\hat{\mathbf{v}}^B]\!] \\ \dots \\ [\![\hat{\mathbf{v}}^Z]\!] \end{Bmatrix}, \tag{6.1}$$

where $\hat{\mathbf{t}}_{21}^{(inc)^n}$ is the known nodal value of the incident traction on the n-th shear band, $[\![\hat{\mathbf{v}}^n]\!]$ is the unknown nodal value of the displacement jump across the n-th shear band, and $\mathbf{C}$ is the coefficient matrix with out-of-diagonal sub-matrices, collecting the contributions of the dynamic interaction between the shear bands. A validation of the collocation

method, with reference to other numerical and analytical solutions, is reported below.

6.2 Discretization and numerical procedure

The treatment of the boundary integral equation (4.27) requires the development of an *ad hoc* numerical procedure, which needs the implementation of a special strategy to enforce the singular behaviour at the band tips, similar to that developed for cracks in [56, 57].

As previously mentioned, the integral equation (4.24) can be numerically solved by using a collocation technique with two different kinds of shape functions: quadratic for the elements inside the shear band and quarter-point at the tips, Figure 6.2. The quarter-point element is a quadratic element with the mid-node moved at the quarter of the lenght of the element from the tip [56], so that the shape functions describe the square root singularity present at the shear band tips, as is usual for the crack tip problem [45, 57, 60].

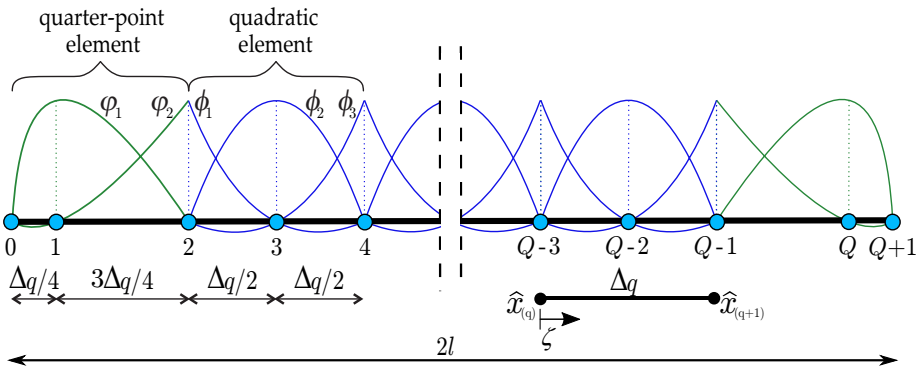

FIGURE 6.2: Subdivision of the shear band line in Q-elements. Within each elements a quadratic variation of the incremental displacement jump is assumed, with the exception of the two elements at the shear band tips where the incremental displacement jump assume a quarter point variation.

The quadratic shape functions are

$$\phi_1 = 1 - 3\,\zeta + 2\,\zeta^2, \tag{6.2}$$

$$\phi_2 = 4\,\zeta - 4\,\zeta^2, \tag{6.3}$$

$$\phi_3 = 2\,\zeta^2 - \zeta, \tag{6.4}$$

while the shape functions for the quarter point element become

$$\varphi_1 = 4\sqrt{\zeta} - 4\,\zeta, \tag{6.5}$$

$$\varphi_2 = 2\,\zeta - \sqrt{\zeta}. \tag{6.6}$$

The square root variation is adopted to take into account the singularity at the shear band tip, as the previous discretization with the linear and square root element for the isolated shear band. For simplicity the length Δ_q of all the elements in the discretization has been taken equal for each element and called Δ_l, in order to have a more compact form for the following equations.

When $\hat{y} = \hat{x}_{(p)}\,(p = 1, \ldots, Q-1)$ is assumed to be the source point, the relevant integral equation becomes

$$\hat{t}_{21}^{(inc)}(\hat{x}_{(p)}) = n_l s_m \mathbb{K}_{lmkg} n_i s_j \Delta_l \int_0^1 i_{ij,k}^g(\hat{x}_{(0)} + \zeta\Delta_l, \hat{x}_{(p)}) \left[[\![\hat{v}]\!]_{(1)}(4\sqrt{\zeta} - 4\zeta) + [\![\hat{v}]\!]_{(2)}(-\sqrt{\zeta} + 2\zeta) \right] d\zeta$$
$$+ n_l s_m \mathbb{K}_{lmkg} n_i s_j \sum_{q=1}^{p-4} \Delta_l \int_0^1 i_{ij,k}^g(\hat{x}_{(q)} + \zeta\Delta_l, \hat{x}_{(p)}) \left[[\![\hat{v}]\!]_{(q)}(1 - 3\zeta + 2\zeta^2)) + [\![\hat{v}]\!]_{(q+1)}(4\zeta - 4\zeta^2) + [\![\hat{v}]\!]_{(q+2)}(2\zeta^2 - \zeta) \right] d\zeta$$
$$+ n_l s_m \mathbb{K}_{lmkg} n_i s_j \sum_{q=p-2}^{p} \Delta_l \int_0^1 i_{ij,k}^g(\hat{x}_{(q)} + \zeta\Delta_l, \hat{x}_{(p)}) \left[[\![\hat{v}]\!]_{(q)}(1 - 3\zeta + 2\zeta^2)) + [\![\hat{v}]\!]_{(q+1)}(4\zeta - 4\zeta^2) + [\![\hat{v}]\!]_{(q+2)}(2\zeta^2 - \zeta) \right] d\zeta$$
$$+ n_l s_m \mathbb{K}_{lmkg} n_i s_j \sum_{q=p+2}^{Q-2} \Delta_l \int_0^1 i_{ij,k}^g(\hat{x}_{(q)} + \zeta\Delta_l, \hat{x}_{(p)}) \left[[\![\hat{v}]\!]_{(q)}(1 - 3\zeta + 2\zeta^2)) + [\![\hat{v}]\!]_{(q+1)}(4\zeta - 4\zeta^2) + [\![\hat{v}]\!]_{(q+2)}(2\zeta^2 - \zeta) \right] d\zeta$$
$$+ n_l s_m \mathbb{K}_{lmkg} n_i s_j \Delta_l \int_0^1 i_{ij,k}^g(\hat{x}_{(Q-2)} + \zeta\Delta_l, \hat{x}_{(p)}) \left[[\![\hat{v}]\!]_{(Q-2)}(4\sqrt{1-\zeta} + 4(\zeta - 1)) + [\![\hat{v}]\!]_{(Q-1)}(-\sqrt{1-\zeta} - 2(\zeta - 1)) \right] d\zeta. \tag{6.7}$$

In equation (6.7), the integrals which are singular for $\hat{x}_{(q)} + \zeta\Delta_l \to \hat{x}_{(p)}$ are relevant to the static kernel $i_{12}^{q(st)}$ and, when the source point $\hat{x}_{(p)}$ coincides with the external node of the quadratic element, can be

rearranged as

$$\begin{aligned}
&\sum_{q=p-2}^{p} \Delta_l \int_0^1 \dot{t}^{g(st)}_{ij,k}(\hat{x}_{(q)} + \zeta\Delta_l, \hat{x}_{(p)}) \left[[\![\hat{v}]\!]_{(q)}(1 - 3\zeta + 2\zeta^2)) \right. \\
&\qquad\qquad \left. + [\![\hat{v}]\!]_{(q+1)}(4\zeta - 4\zeta^2) + [\![\hat{v}]\!]_{(q+2)}(2\zeta^2 - \zeta) \right] d\zeta \\
&= \Delta_l \int_0^1 \dot{t}^{g(st)}_{ij,k}(\hat{x}_{(p-2)} + \zeta\Delta_l, \hat{x}_{(p)}) [\![\hat{v}]\!]_{(p-2)}(1 - 3\zeta + 2\zeta^2)\, d\zeta \\
&+ \Delta_l \int_0^1 \dot{t}^{g(st)}_{ij,k}(\hat{x}_{(p-2)} + \zeta\Delta_l, \hat{x}_{(p)}) [\![\hat{v}]\!]_{(p-1)}(4\zeta - 4\zeta^2)\, d\zeta \\
&+ \Delta_l \int_0^1 \dot{t}^{g(st)}_{ij,k}(\hat{x}_{(p-2)} + \zeta\Delta_l, \hat{x}_{(p)}) [\![\hat{v}]\!]_{(p)}(2\zeta^2 - \zeta)\, d\zeta \\
&+ \Delta_l \int_0^1 \dot{t}^{g(st)}_{ij,k}(\hat{x}_{(p)} + \zeta\Delta_l, \hat{x}_{(p)}) [\![\hat{v}]\!]_{(p)}(1 - 3\zeta + 2\zeta^2)\, d\zeta \\
&+ \Delta_l \int_0^1 \dot{t}^{g(st)}_{ij,k}(\hat{x}_{(p)} + \zeta\Delta_l, \hat{x}_{(p)}) [\![\hat{v}]\!]_{(p+1)}(4\zeta - 4\zeta^2)\, d\zeta \\
&+ \Delta_l \int_0^1 \dot{t}^{g(st)}_{ij,k}(\hat{x}_{(p)} + \zeta\Delta_l, \hat{x}_{(p)}) [\![\hat{v}]\!]_{(p+2)}((2\zeta^2 - \zeta)\, d\zeta,
\end{aligned} \tag{6.8}$$

so that, by means of a change of variable, the integrals can be evaluated as

$$\begin{aligned}
&\sum_{q=p-2}^{p} \Delta_l \int_0^1 \dot{t}^{g(st)}_{ij,k}(\hat{x}_{(q)} + \zeta\Delta_l, \hat{x}_{(p)}) \left[[\![\hat{v}]\!]_{(q)}(1 - 3\zeta + 2\zeta^2)) \right. \\
&\qquad\qquad \left. + [\![\hat{v}]\!]_{(q+1)}(4\zeta - 4\zeta^2) + [\![\hat{v}]\!]_{(q+2)}(2\zeta^2 - \zeta) \right] d\zeta \\
&= \int_{-\Delta_l}^{0} \dot{t}^{g(st)}_{ij,k}(r\mathbf{e}_r) [\![\hat{v}]\!]_{(p-2)} \left(\frac{r}{\Delta_l} + \frac{2r^2}{\Delta_l^2} \right) dr \\
&+ \int_{-\Delta_l}^{0} \dot{t}^{g(st)}_{ij,k}(r\mathbf{e}_r) [\![\hat{v}]\!]_{(p-1)} \left(-\frac{4r}{\Delta_l} - \frac{4r^2}{\Delta_l^2} \right) dr \\
&+ \int_{-\Delta_l}^{\Delta_l} \dot{t}^{g(st)}_{ij,k}(r\mathbf{e}_r) [\![\hat{v}]\!]_{(p)} \left(1 - \frac{3r}{\Delta_l} + \frac{2r^2}{\Delta_l^2} \right) dr \\
&+ \int_{0}^{\Delta_l} \dot{t}^{g(st)}_{ij,k}(r\mathbf{e}_r) [\![\hat{v}]\!]_{(p+1)} \left(\frac{4r}{\Delta_l} - \frac{4r^2}{\Delta_l^2} \right) dr \\
&+ \int_{0}^{\Delta_l} \dot{t}^{g(st)}_{ij,k}(r\mathbf{e}_r) [\![\hat{v}]\!]_{(p+2)} \left(-\frac{r}{\Delta_l} + \frac{2r^2}{\Delta_l^2} \right) dr,
\end{aligned} \tag{6.9}$$

with $\mathbf{e}_r = \mathbf{r}/r$. The non-null finite parts of the above integrals can be calculated as

$$\begin{aligned}
\int_{-\Delta_l}^{0} i_{ij,k}^{g(st)}(r\mathbf{e}_r)\left(\frac{r}{\Delta_l}+\frac{2r^2}{\Delta_l^2}\right)dr &= T_{ijk}^{g}(\theta)\left(\frac{1-3\log(\Delta_l)}{\Delta_l}\right),\\
\int_{-\Delta_l}^{0} i_{ij,k}^{g(st)}(r\mathbf{e}_r)\left(-\frac{4r}{\Delta_l}-\frac{4r^2}{\Delta_l^2}\right)dr &= T_{ijk}^{g}(\theta)\left(\frac{-1+\log(\Delta_l)}{\Delta_l}\right),\\
\int_{-\Delta_l}^{\Delta_l} i_{ij,k}^{g(st)}(r\mathbf{e}_r)\left(1-\frac{3r}{\Delta_l}+\frac{2r^2}{\Delta_l^2}\right)dr &= -T_{ijk}^{g}(\theta)\frac{2}{\Delta_l},\\
\int_{0}^{\Delta_l} i_{ij,k}^{g(st)}(r\mathbf{e}_r)\left(\frac{4r}{\Delta_l}-\frac{4r^2}{\Delta_l^2}\right)dr &= T_{ijk}^{g}(\theta)\left(\frac{-1+\log(\Delta_l)}{\Delta_l}\right),\\
\int_{0}^{\Delta_l} i_{ij,k}^{g(st)}(r\mathbf{e}_r)\left(-\frac{r}{\Delta_l}+\frac{2r^2}{\Delta_l^2}\right)dr &= T_{ijk}^{g}(\theta)\left(\frac{1-3\log(\Delta_l)}{\Delta_l}\right),
\end{aligned} \tag{6.10}$$

and the function $T_{ijk}^{g}(\theta)$ is explicitly provided in Appendix A.

In the particular cases when $\hat{y} = \hat{x}_{(p)}$ is assumed to be the source point and $\hat{x}_{(p)}$ coincides with the inner node of the quadratic element, the singular integrals in equation (6.7) can be rearranged as

$$\begin{aligned}
&\sum_{q=p-1}^{p-1}\Delta_l\int_0^1 i_{ij,k}^{g(st)}(\hat{x}_{(q)}+\zeta\Delta_l,\hat{x}_{(p)})\left[[\![\hat{v}]\!]_{(q)}(1-3\zeta+2\zeta^2)\right.\\
&\qquad\left.+[\![\hat{v}]\!]_{(q+1)}(4\zeta-4\zeta^2)+[\![\hat{v}]\!]_{(q+2)}(2\zeta^2-\zeta)\right]d\zeta\\
&=\Delta_l\int_0^1 i_{ij,k}^{g(st)}(\hat{x}_{(p-1)}+\zeta\Delta_l,\hat{x}_{(p)})[\![\hat{v}]\!]_{(p-1)}(1-3\zeta+2\zeta^2)\,d\zeta\\
&+\Delta_l\int_0^1 i_{ij,k}^{g(st)}(\hat{x}_{(p-1)}+\zeta\Delta_l,\hat{x}_{(p)})[\![\hat{v}]\!]_{(p)}(4\zeta-4\zeta^2)\,d\zeta\\
&+\Delta_l\int_0^1 i_{ij,k}^{g(st)}(\hat{x}_{(p-1)}+\zeta\Delta_l,\hat{x}_{(p)})[\![\hat{v}]\!]_{(p+1)}(2\zeta^2-\zeta)\,d\zeta,
\end{aligned} \tag{6.11}$$

so that, by means of a change of variable, the integrals can be evaluated as

$$\begin{aligned}
\Delta_l \int_0^1 \dot{t}^{g(st)}_{ij,k}(\hat{x}_{(p-1)} + \zeta\Delta_l, \hat{x}_{(p)}) \left[[\![\hat{v}]\!]_{(p-1)}(1 - 3\zeta + 2\zeta^2)) \right. \\
\left. + [\![\hat{v}]\!]_{(p)}(4\zeta - 4\zeta^2) + [\![\hat{v}]\!]_{(p+1)}(2\zeta^2 - \zeta) \right] d\zeta \\
= \int_{-\Delta_l/2}^{\Delta_l/2} \dot{t}^{g(st)}_{ij,k}(r\mathbf{e}_r) [\![\hat{v}]\!]_{(p-1)} \left(-\frac{r}{\Delta_l} + \frac{2r^2}{\Delta_l^2} \right) dr \\
+ \int_{-\Delta_l/2}^{\Delta_l/2} \dot{t}^{g(st)}_{ij,k}(r\mathbf{e}_r) [\![\hat{v}]\!]_{(p)} \left(1 - \frac{4r^2}{\Delta_l^2} \right) dr \\
+ \int_{-\Delta_l/2}^{\Delta_l/2} \dot{t}^{g(st)}_{ij,k}(r\mathbf{e}_r) [\![\hat{v}]\!]_{(p+1)} \left(\frac{2r^2}{\Delta_l^2} \right) dr \\
= T^g_{ijk}(\theta) \frac{2}{\Delta_l} \left[[\![\hat{v}]\!]_{(p-1)} - 4[\![\hat{v}]\!]_{(p)} + [\![\hat{v}]\!]_{(p+1)} \right]
\end{aligned} \tag{6.12}$$

with $\mathbf{e}_r = \mathbf{r}/r$.

In the particular cases when $\hat{y} = \hat{x}_{(p)}$ is assumed to be the source point and $p = 1$ or $p = Q - 1$, equation (6.7) has to be rewritten as

$$\begin{aligned}
\hat{t}^{(inc)}_{21}(\hat{x}_{(p)}) = n_l s_m \mathbb{K}_{lmkg} n_i s_j \Delta_l \int_0^1 \dot{t}^g_{ij,k}(\hat{x}_{(0)} + \zeta\Delta_l, \hat{x}_{(p)}) \left[[\![\hat{v}]\!]_{(1)}(4\sqrt{\zeta} \right. \\
\left. - 4\zeta) + [\![\hat{v}]\!]_{(2)}(-\sqrt{\zeta} + 2\zeta) \right] d\zeta \\
+ n_l s_m \mathbb{K}_{lmkg} n_i s_j \sum_{q=2}^{Q-4} \Delta_l \int_0^1 \dot{t}^g_{ij,k}(\hat{x}_{(q)} + \zeta\Delta_l, \hat{x}_{(p)}) \left[[\![\hat{v}]\!]_{(q)}(1 - 3\zeta + 2\zeta^2)) \right. \\
\left. + [\![\hat{v}]\!]_{(q+1)}(4\zeta - 4\zeta^2) + [\![\hat{v}]\!]_{(q+2)}(2\zeta^2 - \zeta) \right] d\zeta \\
+ n_l s_m \mathbb{K}_{lmkg} n_i s_j \Delta_l \int_0^1 \dot{t}^g_{ij,k}(\hat{x}_{(Q-2)} + \zeta\Delta_l, \hat{x}_{(p)}) \left[[\![\hat{v}]\!]_{(Q-2)}(4\sqrt{1-\zeta} \right. \\
\left. + 4(\zeta - 1)) + [\![\hat{v}]\!]_{(Q-1)}(-\sqrt{1-\zeta} - 2(\zeta - 1)) \right] d\zeta.
\end{aligned} \tag{6.13}$$

When $p = 1$, the finite parts of singular integrals can be evaluated as

$$\Delta_l \int_0^1 \dot{t}^g_{ij,k}(\hat{x}_{(0)} + \zeta\Delta_l, \hat{x}_{(p)}) \left[[\![\hat{v}]\!]_{(1)}(4\sqrt{\zeta} - 4\zeta) + [\![\hat{v}]\!]_{(2)}(-\sqrt{\zeta} + 2\zeta) \right] d\zeta$$

$$= T^g_{ijk}(\theta) \left[-\frac{28}{3\Delta_l} [\![\hat{v}]\!]_{(1)} - \left(\frac{1}{\Delta_l} + \frac{\ln 3}{\Delta_l} \right) [\![\hat{v}]\!]_{(2)} \right], \tag{6.14}$$

while, when $p = Q - 1$, the finite parts of the singular integrals can be evaluated as

$$\Delta_l \int_0^1 \dot{t}^g_{ij,k}(\hat{x}_{(Q-2)} + \zeta\Delta_l, \hat{x}_{(p)}) \left[[\![\hat{v}]\!]_{(Q-2)}(4\sqrt{1-\zeta} + 4(\zeta - 1)) \right.$$

$$\left. + [\![\hat{v}]\!]_{(Q-1)}(-\sqrt{1-\zeta} - 2(\zeta - 1)) \right] d\zeta$$

$$= T^g_{ijk}(\theta) \left[-\frac{28}{3\Delta_l} [\![\hat{v}]\!]_{(Q-1)} - \left(\frac{1}{\Delta_l} + \frac{\ln 3}{\Delta_l} \right) [\![\hat{v}]\!]_{(Q-2)} \right]. \tag{6.15}$$

In the last particular case when $\hat{y} = \hat{x}_{(p)}$ is assumed to be the source point and $p = 2$ or $p = Q - 2$, the relevant integral equation becomes

$$\hat{t}_{21}^{(inc)}(\hat{x}_{(p)}) = n_l s_m \mathbb{K}_{lmkg} n_i s_j \Delta_l \int_0^1 \dot{t}_{ij,k}^g(\hat{x}_{(0)} + \zeta\Delta_l, \hat{x}_{(p)}) \left[[\![\hat{v}]\!]_{(1)}(4\sqrt{\zeta} - 4\zeta) + [\![\hat{v}]\!]_{(2)}(-\sqrt{\zeta} + 2\zeta) \right] d\zeta$$
$$+ n_l s_m \mathbb{K}_{lmkg} n_i s_j \Delta_l \int_0^1 \dot{t}_{ij,k}^g(\hat{x}_{(2)} + \zeta\Delta_l, \hat{x}_{(p)}) \left[[\![\hat{v}]\!]_{(2)}(1 - 3\zeta + 2\zeta^2)) + [\![\hat{v}]\!]_{(3)}(4\zeta - 4\zeta^2) + [\![\hat{v}]\!]_{(4)}(2\zeta^2 - \zeta) \right] d\zeta$$
$$+ n_l s_m \mathbb{K}_{lmkg} n_i s_j \sum_{q=4}^{Q-4} \Delta_l \int_0^1 \dot{t}_{ij,k}^g(\hat{x}_{(q)} + \zeta\Delta_l, \hat{x}_{(p)}) \left[[\![\hat{v}]\!]_{(q)}(1 - 3\zeta + 2\zeta^2)) + [\![\hat{v}]\!]_{(q+1)}(4\zeta - 4\zeta^2) + [\![\hat{v}]\!]_{(q+2)}(2\zeta^2 - \zeta) \right] d\zeta$$
$$+ n_l s_m \mathbb{K}_{lmkg} n_i s_j \Delta_l \int_0^1 \dot{t}_{ij,k}^g(\hat{x}_{(Q-4)} + \zeta\Delta_l, \hat{x}_{(p)}) \left[[\![\hat{v}]\!]_{(Q-4)}(1 - 3\zeta + 2\zeta^2)) + [\![\hat{v}]\!]_{(Q-3)}(4\zeta - 4\zeta^2) + [\![\hat{v}]\!]_{(Q-2)}(2\zeta^2 - \zeta) \right] d\zeta$$
$$+ n_l s_m \mathbb{K}_{lmkg} n_i s_j \Delta_l \int_0^1 \dot{t}_{ij,k}^g(\hat{x}_{(Q-2)} + \zeta\Delta_l, \hat{x}_{(p)}) \left[[\![\hat{v}]\!]_{(Q-2)}(4\sqrt{1-\zeta} + 4(\zeta - 1)) + [\![\hat{v}]\!]_{(Q-1)}(-\sqrt{1-\zeta} - 2(\zeta - 1)) \right] d\zeta. \tag{6.16}$$

When $p = 2$, the finite parts of singular integrals can be evaluated as

$$\Delta_l \int_0^1 \dot{t}_{ij,k}^g(\hat{x}_{(0)} + \zeta\Delta_l, \hat{x}_{(p)}) \left[[\![\hat{v}]\!]_{(1)}(4\sqrt{\zeta} - 4\zeta) + [\![\hat{v}]\!]_{(2)}(-\sqrt{\zeta} + 2\zeta) \right] d\zeta$$
$$+ \Delta_l \int_0^1 \dot{t}_{ij,k}^g(\hat{x}_{(2)} + \zeta\Delta_l, \hat{x}_{(p)}) \left[[\![\hat{v}]\!]_{(2)}(1 - 3\zeta + 2\zeta^2) + [\![\hat{v}]\!]_{(3)}(4\zeta - 4\zeta^2) + [\![\hat{v}]\!]_{(4)}(2\zeta^2 - \zeta) \right] d\zeta =$$
$$= T_{ijk}^g(\theta) \left[\left(-\frac{1}{2\Delta_l} + \frac{2\ln\Delta_l}{\Delta_l} \right) [\![\hat{v}]\!]_{(1)} + \left(\frac{1}{8\Delta_l} - \frac{9\ln\Delta_l}{2\Delta_l} \right) [\![\hat{v}]\!]_{(2)} + \left(-\frac{4}{\Delta_l} + \frac{4\ln\Delta_l}{\Delta_l} \right) [\![\hat{v}]\!]_{(3)} + \left(\frac{2}{\Delta_l} - \frac{\ln\Delta_l}{\Delta_l} \right) [\![\hat{v}]\!]_{(4)} \right]. \tag{6.17}$$

with $\mathbf{e}_r = \mathbf{r}/r$.

6.3 Validation of the numerical procedure

A validation of the numerical approach, is pursued through an analysis of a shear band present in an isotropic material at null prestress, that can be compared with a crack loaded in Mode II. Figure 6.3 shows the results of the normalized SIF function of the wavenumber, for three different inclinations of the wave propagation vector $(0, \pi/6, \pi/3)$. The solution obtained with quadratic and quarter point elements (Q+QP, circle spots) is compared with an available analytical solution [17] (solid lines), and the previous discretization based on linear and square root shape functions (L+SR, diamond spots).

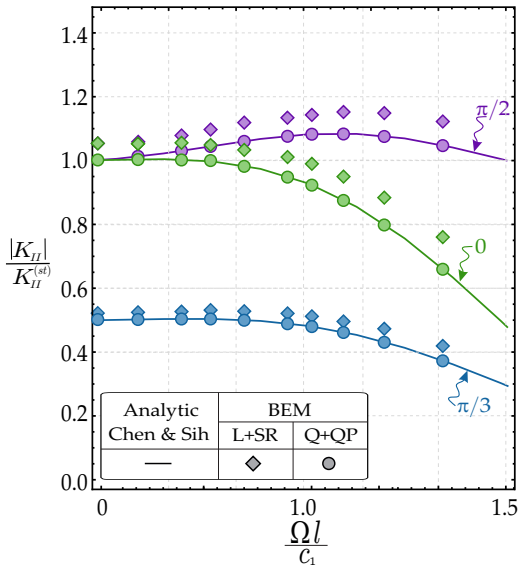

FIGURE 6.3: Comparison of the modulus of the normalized mode II Stress Intensity Factor at the shear band tip (for an isotropic material at null prestress) as a function of the wavenumber, with the analytical solution of Chen and Sih[17] and the numerical solution based on linear and square root shape functions.

With a discretization of 100 elements the errors related to the analytical solution are about 8% for the mixed BEM with $L + SR$ and about 0.2% for the collocation technique with $Q + QP$.

7 Results for multiple shear bands interaction

Results reported in the following are limited for simplicity to the hardening exponent $N = 0.4$, representative of a medium carbon steel, and to a level of prestress close to the elliptic boundary (k =0.87 and ξ=0.26, parameters corresponding to the inclination $\theta \approx \pm 26°$), so that some shear bands are expected to be already formed. Time-harmonic incident shear waves of circular frequency Ω have been adopted, as for the case of the isolated shear band.

7.1 Parallel shear bands

In the case of two equal and parallel shear bands (Figure 6.1(a)), two directions of propagation for the impinging waves with wavenumber $\Omega\, l/c_1 = 1$ (c_1 is the propagation velocity in the direction of x_1-axis) are considered: one aligned orthogonal ($\beta = \theta + \pi/2$) and the other parallel to the shear bands ($\beta = \theta$). The wavenumber considered corresponds to ones in which resonance condition occurs for the isolated shear band. The ratio between the static and dynamic Mode II Stress Intensity Factor at the tip of the shear band is reported in Figure 7.1 as a function of the dimensionless distance d/l between the two shear bands, denoting with $+$ and $-$ the right and left tips respectively. At the tips A^-, A^+ and

B^-, B^+ the values of the SIF oscillate about the value pertinent to an isolated shear band. Note that the SIF assumes the same value

- at the tip pairs A^-, A^+ and B^-, B^+ for wave propagation orthogonal to the shear bands;
- at the tip pairs A^-, B^- and A^+, B^+ for wave propagation parallel to the shear bands.

For both wave propagation directions, the SIFs grow when the distance between the two shear bands decreases. The peaks of the SIFs denote resonance, which is much more pronounced than in the case of an isolated shear band (reported in Figure 7.1 for comparison with Figure 5.2). Therefore, two shear bands provide an amplification to resonance, thus promoting shear band growth.

For the shear band geometry (a), the (modulus of the) incremental deviatoric strain is plotted in Figure 7.2, when a wave is travelling parallel to the shear band ensemble. The two cases reported in the figure differ only in the distance between the shear bands. In the upper and lower parts of Figure 7.2, the distance is $d = 2.5\,\lambda_{\pi/2+\theta}$ and $d = 4\,\lambda_{\pi/2+\theta}$, respectively, with λ_α being the wavelength in the propagation direction singled out by angle α. The scattered field is reported on the left, while the total field in the centre. The graphs on the right side are cross-sections of the scattered deviatoric strain along $\hat{x}_2$-axis, cut at shear band centre.

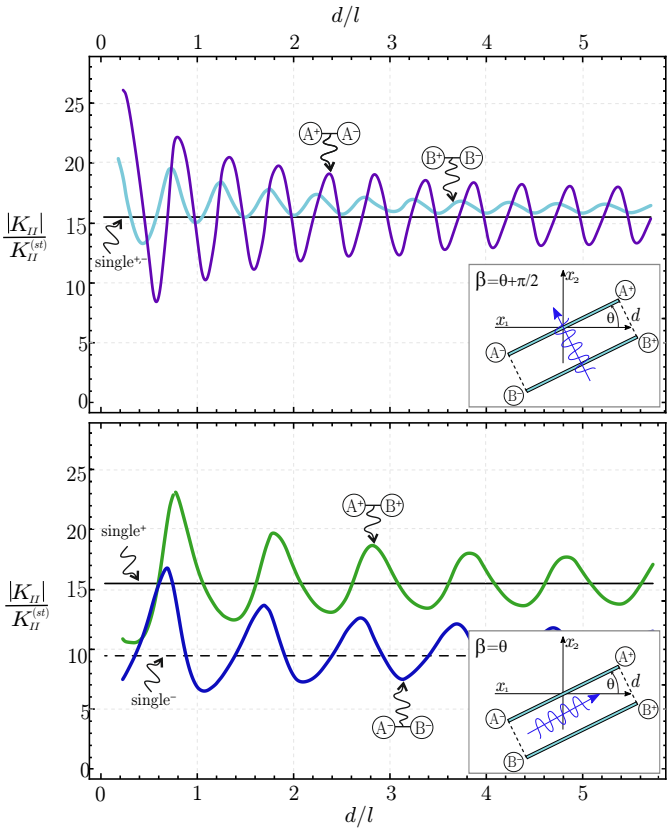

FIGURE 7.1: Resonance, as induced by two parallel shear bands (much more pronounced than in the case of an isolated shear band, also reported in the figure), is revealed by the peaks of the dimensionless stress intensity factor, reported as a function of the distance d between the shear bands for a wavenumber $\Omega l/c_1 = 1$: (a) direction of the wave propagation orthogonal to the shear bands $\beta = \theta + \pi/2$, (b) direction of the wave propagation parallel to the shear bands $\beta = \theta$. The SIF of one isolated shear band is also reported. The right and left tips are labelled with $+$ and $-$ respectively.

Overall, Figure 7.2 shows that the ratio between the shear band distance and the wavelength of the impinging wave may determine focusing (which promotes shear band nucleation, see the upper part of the figure)

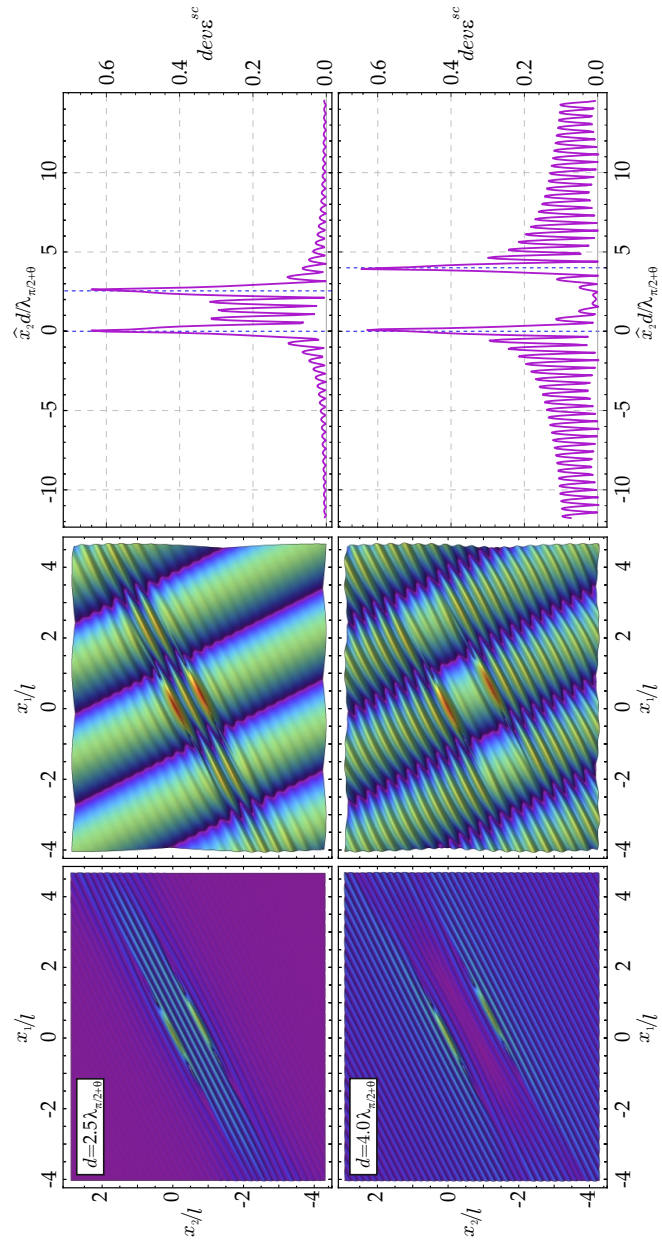

FIGURE 7.2: Examples of wave focusing (upper part) and shielding (lower part) generated by two parallel shear bands. Scattered (left) and total (œntre) incremental deviatoric strain field is reported as produced by an incident shear wave travelling parallel to the shear bands ($\beta = \theta$) with wave number $\Omega l/c_1 = 1$. The graphs on the right side are cross-sections of maps on the left side, cut at the centre of the shear bands.

or shielding (which leaves the material inside the shear bands unstressed, see the lower part of the figure) of the mechanical disturbance in the region enclosed within the shear bands.
The explanation of this behaviour is given by the analysis of the single contribution of each shear band in the definition of the modulus of the deviatoric strain field, expressed in the form

$$dev\,\varepsilon = \sqrt{\frac{v_{1,1}^2 + v_{2,2}^2 - 2v_{1,1}v_{2,2} + 2v_{1,2}v_{2,1}}{4}}. \tag{7.1}$$

Considering equation (3.11) in which the total displacement field is given by the superimposition of the incident and the scattered fields, the same thing is valid for the gradient of the displacement field. Thus, using the integral equation (4.13), the gradient of the scattered field for a couple of shear bands can be evaluated with the equation

$$v_{g,k}^{sc}(\mathbf{y}) = \underbrace{-\int_{-l_A}^{l_A} \dot{t}_{ij,k}^{g}(\hat{x}_1^A, \mathbf{y}) n_i^A [\![v_j^A]\!] d\hat{x}_1^A}_{Contribution\,A} \underbrace{-\int_{-l_B}^{l_B} \dot{t}_{ij,k}^{g}(\hat{x}_1^B, \mathbf{y}) n_i^B [\![v_j^B]\!] d\hat{x}_1^B}_{Contribution\,B}, \tag{7.2}$$

which sums the two contributions of the shear bands A and B. Figure 7.3 shows both contributions A and B of the gradient of the displacement $v_{1,2}$ for the previous cases presented in Figure 7.2, and it is possible to conclude that:

- when the distance between the shear bands is equal to an entire number and a half the wavelength (i.e. $2.5\,\lambda_{\pi/2+\theta}$ in the picture), contributions A and B are *in phase* inside the shear bands and in *anti-phase* outside, where the scattered gradient of the displacement $v_{1,2}$ goes to vanish;

- when the distance between the shear bands is equal to an entire number the wavelength (i.e. $4\,\lambda_{\pi/2+\theta}$ in the picture), contribution A and B are *in phase* outside the shear bands and in *anti-phase* inside them, where the scattered gradient of the displacement $v_{1,2}$ goes to vanish.

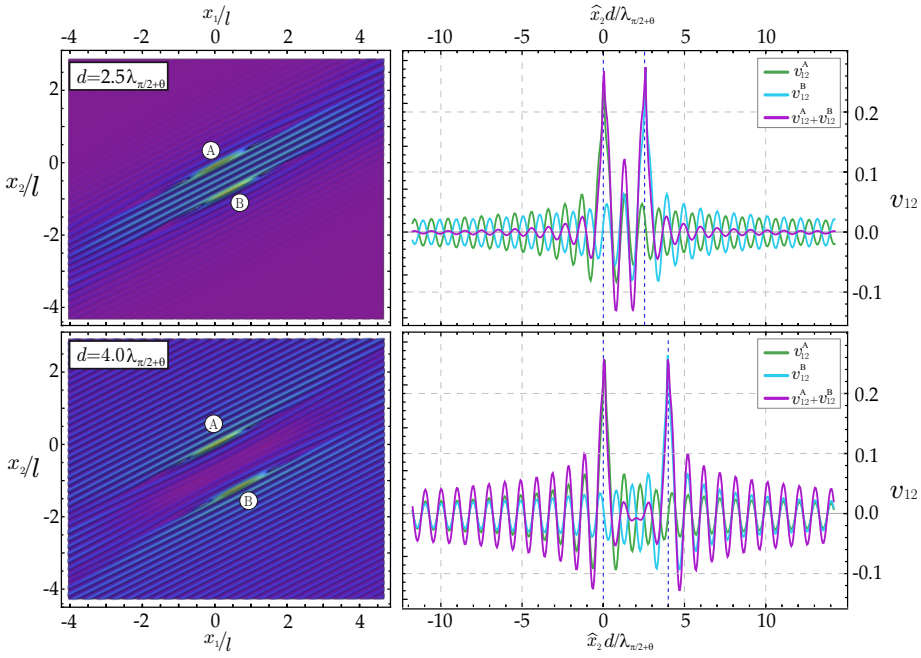

FIGURE 7.3: Examples of wave focusing (upper part) and shielding (lower part) generated by two parallel shear bands. Scattered incremental deviatoric strain field is reported as produced by an incident shear wave travelling parallel to the shear bands ($\beta = \theta$) with wave number $\Omega\, l/c_1 = 1$. The graphs on the right side are cross-sections of maps on the gradient of the displacement field $v_{1,2}$, cut at the centre of the shear bands.

Similar results for the SIF can be found in fracture mechanics, for the dynamics of parallel cracks. In particular, increasing values of the SIF at decreasing crack distance [19, 23, 21, 47] and focussing of the displacement field between the cracks[54] have been found.

7.2 Aligned shear bands

Two aligned shear bands of equal length $2l$, at a distance d, are analyzed (Figure 6.1(b)) for an impinging wave with wavenumber $\Omega\, l/c_1 = 1$. The normalized SIF at the tips of the shear bands is evaluated as a function of the dimensionless distance d/l, for an incident wave with direction of propagation orthogonal to the shear bands ($\beta = \theta + \pi/2$), Figure 7.4. When the two shear bands are distant, the SIFs tend to the value pertinent to one isolated shear band, but the SIF at the inner tips (A^+B^-) strongly blows up when the distance between the two shear bands tends to vanish. This effect promotes the coalescence of the two shear bands.

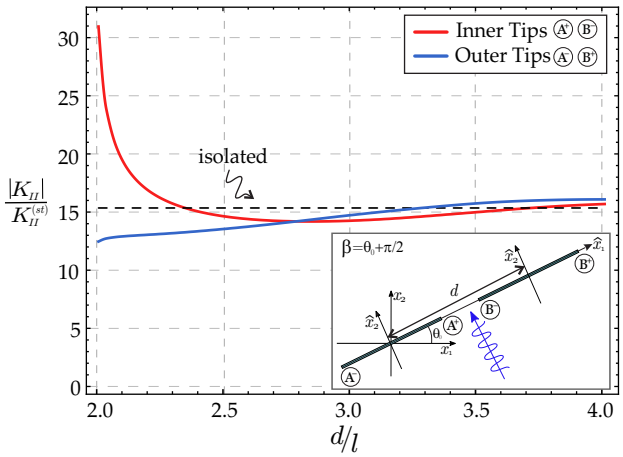

FIGURE 7.4: Coalescence of two aligned shear bands is demonstrated by the dimensionless SIF reported as a function of the distance d for a wave travelling orthogonal to the shear bands and wavenumber $\Omega\, l/c_1 = 1$.

For a wave travelling orthogonal to two aligned shear bands, the profile of the displacement jump across the shear band surfaces is reported in Figure 7.5, for $d = 2l(1 + 1/100) \approx 2l$, together with the profile pertinent to an isolated shear band of length $2l$ and $4l$. The profiles of the two aligned shear bands are non-symmetric and, in a sense, they seem to 'attract each other'. However, the two profiles are very different, so that two shear bands are not equivalent to an isolated shear band with a length equal to the sum of the two lengths.

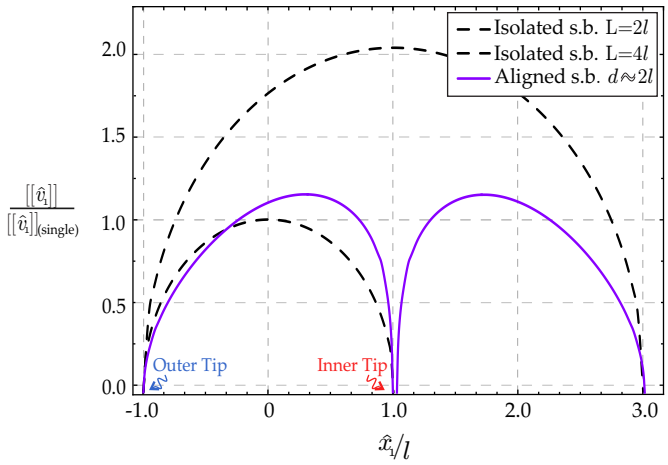

FIGURE 7.5: The strong difference between two aligned shear bands of length $2l$ close to each other, and one isolated shear band, either of length $4l$ or $2l$ (both reported as dashed lines) is visible from the profile of the displacement jump along the shear band surfaces.

The modulus of the total deviatoric strain field is reported for two aligned shear bands in Figure 7.6 (a) and (b), for a wave travelling parallel to them ($\beta = \theta$), for the case with $d = \lambda_\theta/2$ and for the case with $d = \lambda_\theta$ respectively. These figures show a sort of 'overall' elimination or intensification, meaning that the scattered field is everywhere annihilated in case (a) or amplified in case (b). Therefore, a system of two shear bands produces a mechanical disturbance which may or may not (depending on the ratio d/λ) propagate in a material far beyond the location of the shear bands.

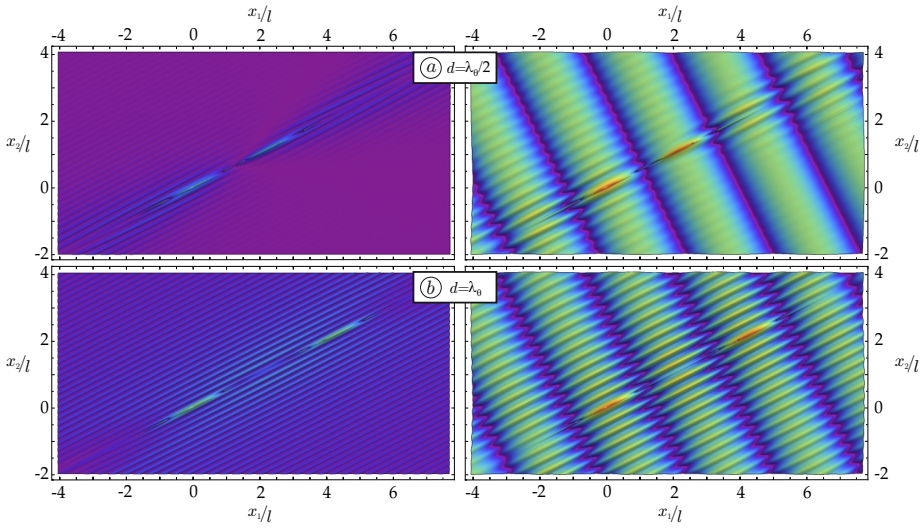

FIGURE 7.6: (a) Annihilation of the stress field is revealed by the modulus of the incremental deviatoric strain field produced by an incident shear wave travelling parallel to the shear bands ($\beta = \theta$) with wave number $\Omega\, l/c_1 = 1$ and distance $d = \lambda_\theta/2$; (b) Amplification of the stress field is determined under the same condition as for (a), but assuming $d = \lambda_\theta$. Note that the maps on the left represent the scattered field, while the total fields are reported on the right.

7.3 Converging shear bands

Two shear bands, disposed in a conical geometry, inclined at $\pm\theta$ and located at a minimal distance $d = l/10$ (Figure 6.1(c)), are analyzed in Figure 7.7 and 7.8, for $\Omega\, l/c_1 = 1$. The dimensionless SIF is reported in the lower part of Figure 7.7, as a function of the propagation direction β of the impinging wave, that generates the nominal shear stress t_{21} reported in the upper part of the figure. The picture shows that when the wave travels orthogonal to one of the two shear bands ($\beta = \pi/2 - \theta$ or $\beta = \pi/2 + \theta$), the relevant shear band tip is loaded with a maximum value of the shear stress, while the other shear band tip results quite unloaded because is subjected to a minimum value of shear stress, hence the SIF reaches a maximum or minimum values when the wave travels orthogonal to one or the other shear band respectively.

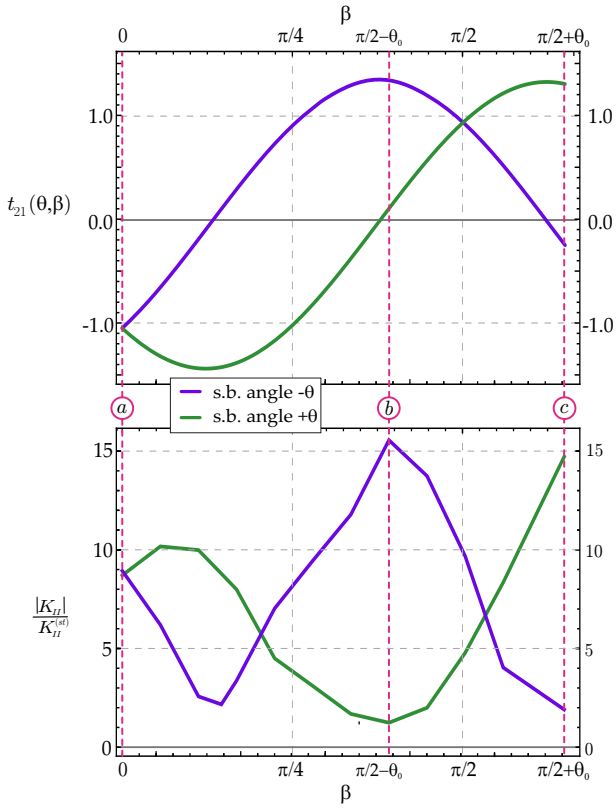

FIGURE 7.7: Loading and simultaneous unloading of two converging shear band tips is revealed by the dimensionless Mode II SIF, reported at the closest tips of both shear bands, as function of the propagation direction β of the impinging wave. The three inclination β highlighted with (a), (b), (c), correspond to the cases analyzed in Figure 7.8.

In Figure 7.8 the modulus of the scattered and total deviatoric strain fields are analysed for the three directions of propagation of the wave β, referred to the cases (a), (b), (c) labelled in Figure 7.7. The effect in which the shear band results unloaded (minimum shear stress and SIF), corresponds to its annihilation, and it becomes clearly visible in parts (b) and (c) of the Figure 7.8, where one shear band (marked with a dashed white line) 'disappears', while at the same time the other is 'reinforced'.

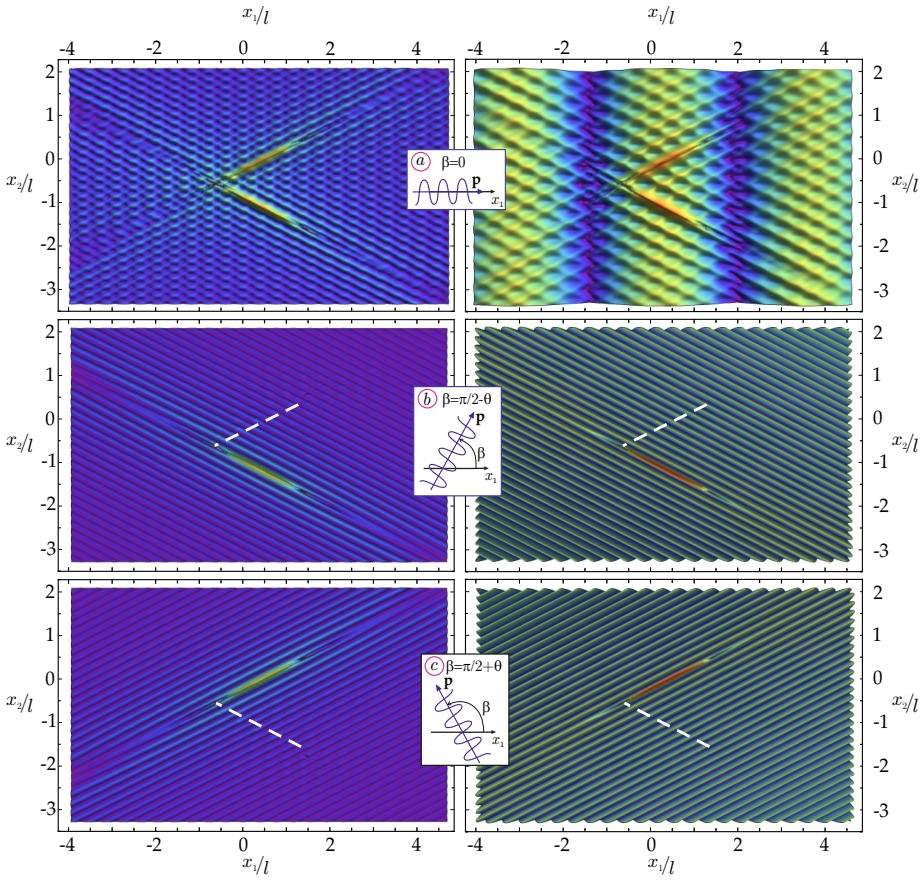

FIGURE 7.8: (a) A fine texture of secondary planar waves is evidenced by the modulus of the deviatoric incremental strain field produced by an impinging wave propagating horizontally $\beta = 0$; (b) Annihilation of one shear band and reinforcement of the other is produced in the same conditions as for part (a), but assuming $\beta = \pi/2 - \theta$; (c) A switch is produced from the annihilated to the reinforced shear band with respect to part (b), assuming now $\beta = \pi/2 + \theta$. Note that the maps on the left represent the scattered field, while the total fields are reported on the right. The three inclination of (a), (b), (c) are referred to to the same label of Figure 7.7.

This is due to the fact that the scattered field of the annihilated shear

band is so small that doesn't influence the contribution of the other shear band. When the impinging wave is horizontal, the two shear bands behave in the same way and produce a fine texture of 'secondary' planar waves inclined at the critical directions for shear band formation, as is shown in Figure 7.8 (a).

7.4 Four shear bands

A system of four shear bands is considered as sketched in Figure 6.1 (d), impinged by a horizontally propagating wave with $\Omega\, l/c_1 = 1$. Results in terms of maps of the (modulus of the) deviatoric strain are reported in Figure 7.9 for the scattered (left) and total (right) fields at a distance $d = 8\,\lambda_{\pi/2+\theta}$ (upper part) and $d = 8.5\,\lambda_{\pi/2+\theta}$ (lower part).

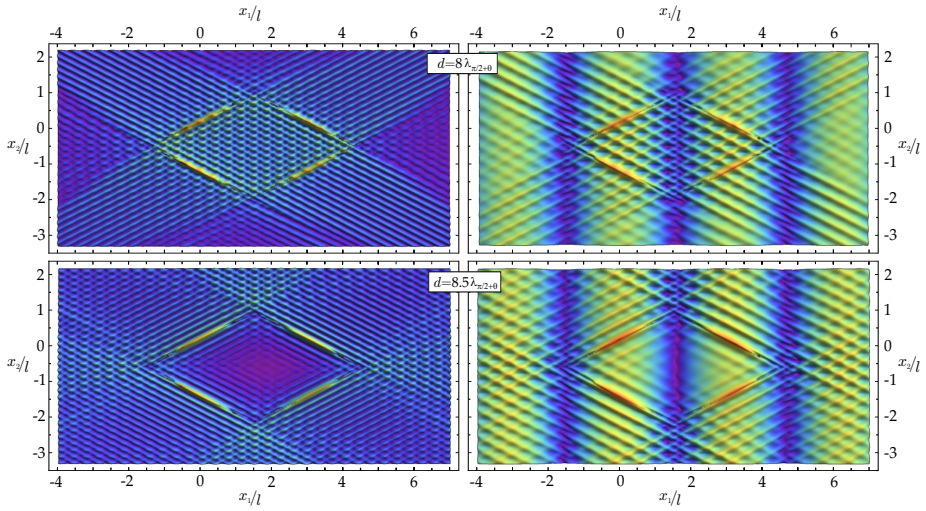

FIGURE 7.9: Examples of creation of an 'island' of focusing (upper part) and shielding (lower part) produced by a system of four shear bands subjected to horizontally ($\beta = 0$) impinging waves. Scattered (left) and total (right) incremental deviatoric strain field are reported, for wave number $\Omega\, l/c_1 = 1$: in the upper part, a characteristic shear band distance $d = 8\lambda_{\pi/2+\theta}$ is selected, while $d = 8.5\lambda_{\pi/2+\theta}$ is selected for the lower part.

The case reported in the upper part of the figure provides an example of focusing of the signal, while shielding is evidenced in the case reported in the lower part. In the upper case, the stress intensifies, while in the lower case an 'island of stress relief' is created.

8 Conclusions

The dynamic effects induced by a shear band formed in a material strained close to the failure of ellipticity can be analysed through the development of *ad hoc* boundary integral equations and collocation techniques. Results show that the shear band produces a complex dynamic interaction with impinging waves generating resonance at a certain frequency. This resonance promotes shear band development, as can be revealed by the variation with frequency of the stress intensity factor at the shear band tips. Moreover, the vibration pattern generated near the shear band shows a fine development of plane waves and the formation of a narrow zone of low incremental strain emerging from the shear band edges and propagating with a conical shape.

The analysis can be extended to investigate the complex interactions between multiple shear bands during wave propagation, leading in some cases to resonance (which promotes shear band growth and coalescence), but in other cases to annihilation (which produces shear band arrest). Furthermore, different geometries can lead to opposite effects, of focusing or shielding from waves, so that in the former case nucleation of a new shear band is promoted, while in the latter the material remains 'untouched' by the wave field.

It is worth noting that the results obtained in the present thesis can be generalized in several ways. In particular: (i.) three-dimensional problems can be analysed in which the shear band can assume a complex

form, for instance penny-shaped, conical or curved; (ii.) materials with different constitutive equations and even materials different from metals, for instance granular matter, can be considered; (iii.) transient dynamics may be studied. In all these cases, the boundary integral equations developed in the thesis are either still valid or require minimal modifications, so that only the Green's function has to be determined, a difficulty which can be attacked with the methods shown in [1, 48, 64].

A The particular case of two parallel cracks

Let now consider a Mooney-Rivlin material in the limit case in which the prestress is null ($k = 0$), so that the isotropic condition is reached. As mentioned in Chapter 3, in the absence of prestress the shear band model reduces to a weak surface whose faces can freely slide, so that in the isotropic condition, the solution presented for the shear band, corresponds to the same solution of an horizontal fracture subjected to a Mode II shear loading. In fact since a fracture has null incremental nominal traction orthogonal to the surfaces, boundary condition (3.3) is always valid.

Two parallel cracks of length $2l$ and distance d, both parallel to the horizontal principal axes x_1 in an infinite incompressible and isotropic material, are now considered. The present Chapter wants to analyse the dynamic regime and the resonance condition of two parallel cracks. Results will be compared to those of a rectangular block with dimensions $2l$ and d (equal to the length of the cracks and the distance between them), subjected to pure shear loading.

A.1 The Green's function for linear elasticity

The isotropic condition corresponds in the elliptic regimes to null prestress ($k = 0$) and parameter of anisotropy $\xi = 1$. With these assumptions, 2-D Green's function for linear elasticity in the time harmonic domain can be used to evaluate the problem, and it can be derived in the same way as for the Green's function for nonlinear elasticity presented in Chapter 2. The final expression of the Green's function is defined as

$$v_i^g(\mathbf{x}, \Omega) = \frac{1}{8\,\pi^2} \int_{|\boldsymbol{\omega}|=1} \sum_{m=1}^{2} \frac{P_{gi}^m}{\rho\, c_m^2} \Phi(k_m\, |\boldsymbol{\omega} \cdot \mathbf{x}|)\, d\boldsymbol{\omega}, \tag{A.1.1}$$

with

$$\Phi(\xi) = i\,\pi\, e^{\xi} - 2\,[\cos(\xi) Ci(\xi) + \sin(\xi) Si(\xi)]\,, \tag{A.1.2}$$

in which $k_m = \Omega / c_m$ is the wavenumber and c_m is the wavespeed in the direction m defined as

$$c_1 = \sqrt{\frac{\mu}{\rho}}, \qquad c_2 = \sqrt{\frac{\lambda + 2\mu}{\rho}}. \tag{A.1.3}$$

The expressions of the Lamè constants λ and μ are

$$\lambda = \frac{\nu}{(1-2\nu)(1+\nu)}, \qquad \mu = \frac{1}{2(1+\nu)}, \tag{A.1.4}$$

in which ν is the Poisson's ratio, and they characterise the elastic constants of the fourth-order tensor $\mathbf{C}$ with the relation

$$C_{ijpk} = \lambda \delta_{ij} \delta_{pq} + \mu(\delta_{ip}\delta_{jq} + \delta_{iq}\delta_{jp}). \tag{A.1.5}$$

Moreover, the term P_{gi}^m in equation (A.1.1) is defined as

$$P_{gi}^m = E_{il} E_{jl}, \tag{A.1.6}$$

where the column of tensor $\mathbf{E}$ are the eigenvectors of the tensor $\Gamma_{ip}(\boldsymbol{\omega})$, which is expressed as a function of the elastic coefficients with the relation

$$\Gamma_{ip}(\boldsymbol{\omega}) = C_{ijpk}\omega_j\omega_q. \tag{A.1.7}$$

As for the previous case of nonlinear elasticity, the 2-D Green's functions can be split into a regular and singular parts as

$$v_i^g(\mathbf{x},\Omega) = v_i^{gR}(\mathbf{x},\Omega) + v_i^{gS}(\mathbf{x}), \tag{A.1.8}$$

with the regular part $v_i^{gR}(\mathbf{x},\Omega)$ defined as

$$v_i^{gR}(\mathbf{x},\Omega) = \frac{1}{8\,\pi^2}\int_{|\boldsymbol{\omega}|=1}\sum_{m=1}^{2}\frac{P_{gi}^m}{\rho\,c_m^2}\Phi^R(k_m,|\boldsymbol{\omega}\cdot\mathbf{x}|)\,d\boldsymbol{\omega}, \tag{A.1.9}$$

with

$$\Phi^R(k_m,|\boldsymbol{\omega}\cdot\mathbf{x}|) = \Phi(k_m|\boldsymbol{\omega}\cdot\mathbf{x}|) + 2\log(|\boldsymbol{\omega}\cdot\mathbf{x}|), \tag{A.1.10}$$

and the singular part $v_i^{gS}(\mathbf{x})$ as

$$v_i^{gS}(\mathbf{x}) = -\frac{1}{4\,\pi^2}\int_{|\boldsymbol{\omega}|=1}\sum_{m=1}^{2}\Gamma_{ip}^{-1}(\boldsymbol{\omega})\log(|\boldsymbol{\omega}\cdot\mathbf{x}|)\,d\boldsymbol{\omega}. \tag{A.1.11}$$

The 2-D Green's function (A.1.1) has been used in the boundary integral equation (4.28), and the results are reported in the chapter.

A.2 The resonance of a rectangular block under pure shear loading

A rectangular, incompressible and isotropic elastic block of dimensions $2l \times d$ under pure shear loading, whose principal directions are aligned parallel to the edges of the block, is considered.

Referring to Figure A.1, the boundary conditions are:

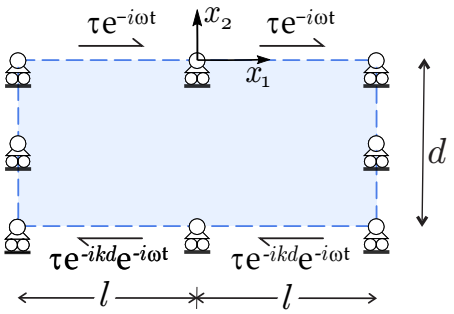

FIGURE A.1: A rectangular, incompressible and isotropic elastic block under pure shear loading.

- null horizontal incremental tractions and vertical incremental displacement:

$$\dot{t}_{11} = 0, v_2 = 0 \tag{A.2.12}$$

  along the vertical edges at $x_1 = -l$ and $x_1 = l$;

- prescribed time-harmonic shear tractions and null vertical displacement:

$$\dot{t}_{21} = \tau e^{i\,k\,x_2} e^{-i\omega\,t}, v_2 = 0 \tag{A.2.13}$$

  along the horizontal edges at $x_2 = 0$ and $x_2 = -d$, with k the wavenumber.

Considering the nominal incremental stress field described in Chapter 2, and assuming a solution in the form

$$v_1(x_1, x_2) = \tilde{v}_1 e^{i\Omega\,t}, \quad v_2(x_1, x_2) = 0, \tag{A.2.14}$$

and with substitution in the equations of motion (2.31), with null incremental body forces $f_j = 0$, leads to the non-trivial equation

$$\frac{\mathrm{d}^2\tilde{v}_1}{\mathrm{d}x_2^2} = -\frac{\omega^2}{c_L^2}\tilde{v}_1. \tag{A.2.15}$$

where c_L is the propagation velocity of a transverse plane wave travelling parallel to x_2-axis.

By solving the differential equation (A.2.15) and imposing the boundary conditions (A.2.12) and (A.2.13), the solution of the problem is

$$v_1(x_1,x_2) = -\frac{c_L\left(\cos\left(\frac{\omega}{c_L}d\right) - e^{\left(i\frac{\omega}{c_L}d\right)}\right)}{\omega\,\sin\left(\frac{\omega}{c_L}d\right)}\cos\left(\frac{\omega}{c_L}x_2\right) + \frac{c_L}{\omega}\sin\left(\frac{\omega}{c_L}x_2\right) \tag{A.2.16}$$

for which the eigenfrequencies of the elastic block are

$$\Omega = n\,\pi\frac{c_L}{d} \quad n = 1,2,3... \tag{A.2.17}$$

A.3 The resonance of two parallel cracks

Two parallel cracks of length $2l$ and distance d, parallel to the horizontal principal axes x_1 in an infinite incompressible and isotropic material, are now considered. Three different cases of distances between the cracks have been evaluated: $d = l, l/2, l/4$, and for each distance d the results obtained are compared to those of the elastic block that have the same length d.

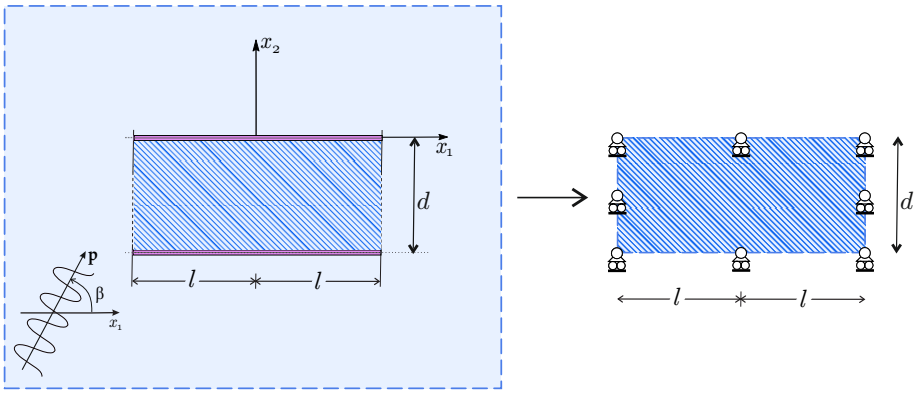

FIGURE A.2: Two parallel cracks (left) of length $2\,l$ and distance d. The material between the two parallel cracks is sketched as a rectangular block (right) under pure shear loading.

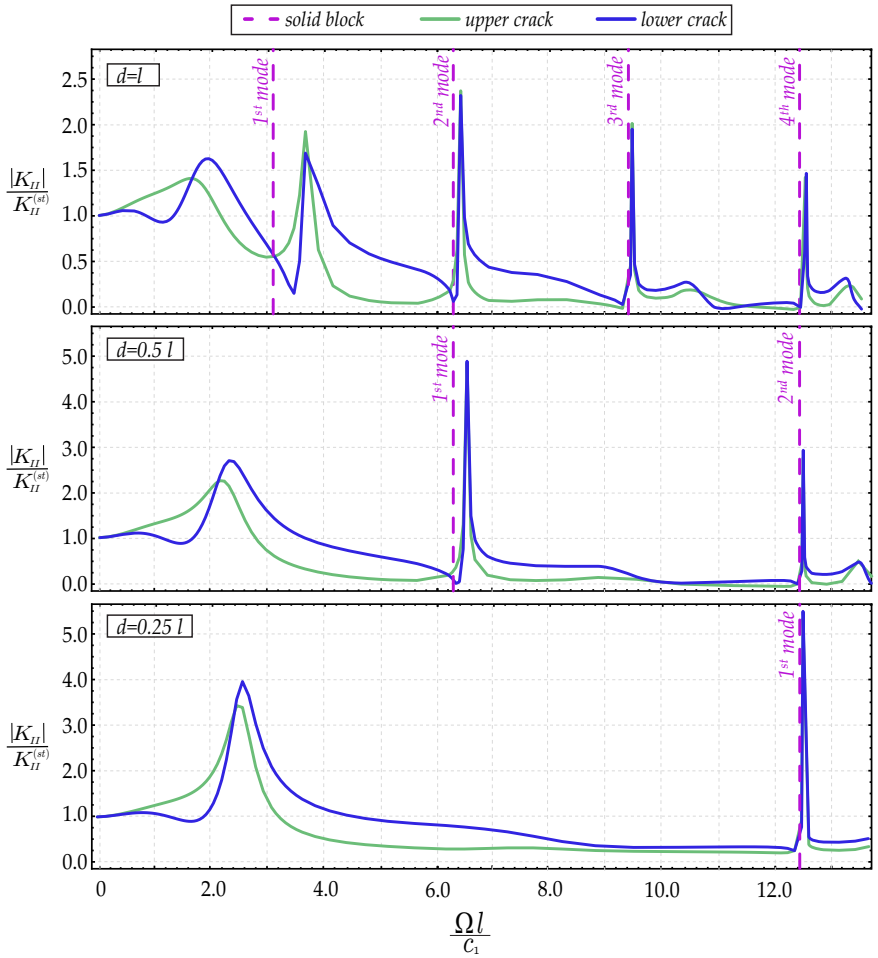

FIGURE A.3: Normalized Mode II Stress Intensity Factor of two parallel cracks as a function of the wavenumber for three different cases of distances $d = l, l/2, l/4$ between the cracks. Comparison of the eigenfrequencis of the elastic block (with length d equal to the distance between the cracks), with the peaks of the SIFs that show the resonance of the cracks.

The variation with the wavenumber, $\Omega l/c_1$, of the modulus of the normalized Mode II Stress Intensity Factor K_{II}/K_{II}^{st} for the two parallel cracks, is shown in Figure A.3 for the three different distances between

the crack $d = l, l/2, l/4$, and the results obtained are compared to those of the elastic block under pure shear loading found in the previous section, with the same distance/length d.
In this figure the peaks of the curves represent resonance condition, so that it is clear that a decrease in the distance leads to an higher amplification factor. For each solid curve of the Figure, many different resonance peaks are visible for high frequencies ($\Omega l/c_1 > 2$). In particular, the comparison of the results with the eigenfrequencies of the elastic block studied in the previous sections (dashed lines in Figure A.3), leads to the conclusion that two parallel cracks reach resonance condition for quite the same frequencies of a solid block with dimensions d equal to the distance between the two cracks. The lower is the distance d, the lower is the error between the eigenfrequency and the resonance of the cracks, and then it means that the surfaces of the cracks behave as free surfaces.
This is due to the fact that for higher distance d the lateral material corresponds to a constraint of the rectangular area between the cracks.
The results obtained can be compared to those of a single crack near a free surface, in which a strong correlation between its resonance and the natural frequencies of a Timoshenko plate (plane-strain case) was found [31]. In particular, for values of d/l small (≈ 0.2) the clamped plate and the simply supported plate appeared to provide an upper and lower bound, respectively, of the frequency.

A.3.1 Deviatoric strain fields

For the three previous cases of distances $d = l, l/2, l/4$ between the two parallel cracks, the deviatoric strain field is analysed, and for all the following figures the scattered deviatoric strain field is reported on the left, while the total deviatoric strain field is reported on the right.

Considering the first case with distance $d = 0.25\, l$ between the cracks, Figure A.4 shows in the upper part the deviatoric fields for a frequency a bit before the resonance condition ($\Omega < \Omega^{R1}$), and in the lower part for the frequency corresponding to the first resonance condition of the cracks ($\Omega = \Omega^{R1}$) (the first peak of the curves for high frequencies $\Omega l/c_1 > 2$ of Figure A.3). It is shown that the two scattered fields are more similar

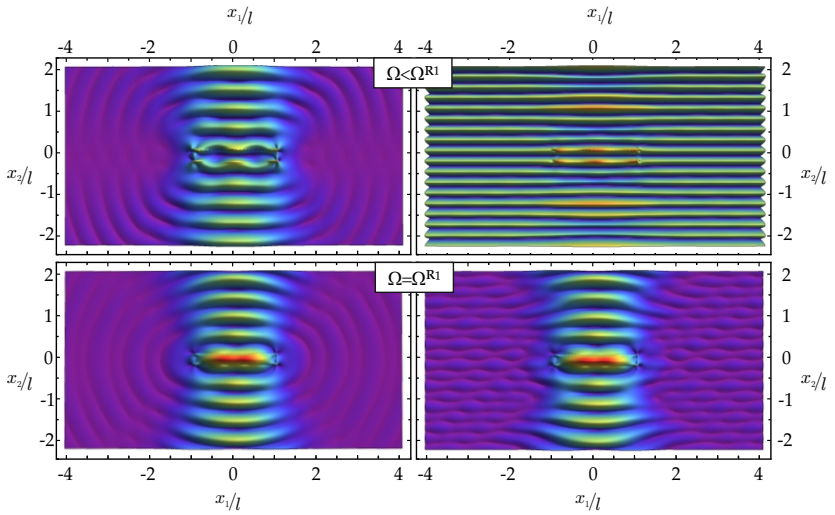

FIGURE A.4: Scattered (left) and total (right) deviatoric strain fields for two parallel cracks of length $2\,l$ and distance $d = 0.25\,l$, and for a frequency before the resonance ($\Omega < \Omega^{R1}$) and in resonance condition ($\Omega = \Omega^{R1}$).

and composed of a family of plane waves propagating orthogonal to the cracks, whereas, the total deviatoric strain fields are completely different. In fact, for the case before the resonance condition ($\Omega < \Omega^{R1}$), the total field is predominant respect to the scattered field that generates only a very low perturbation of the total field. At the opposite, in the case of resonance ($\Omega = \Omega^{R1}$) the scattered field is dominant, and creates a sort of focussing of the waves for a width equal to the length of the cracks, so that the incident field is strongly perturbed by the scattered field.
The same effects can be seen for the other cases of $d = 0.5\,l$ in Figure A.5, in which the deviatoric strain fields are reported for the two resonance conditions Ω^{R1}, Ω^{R2} and for the two frequencies before each resonance $\Omega < \Omega^{R1}$ and $\Omega^{R1} < \Omega < \Omega^{R2}$. Moreover, results for $d = l$ are reported in Figure A.6 and A.7 in which four resonance conditions $\Omega^{R1}, \Omega^{R2}, \Omega^{R3}, \Omega^{R4}$ and four frequencies before each resonance are shown.

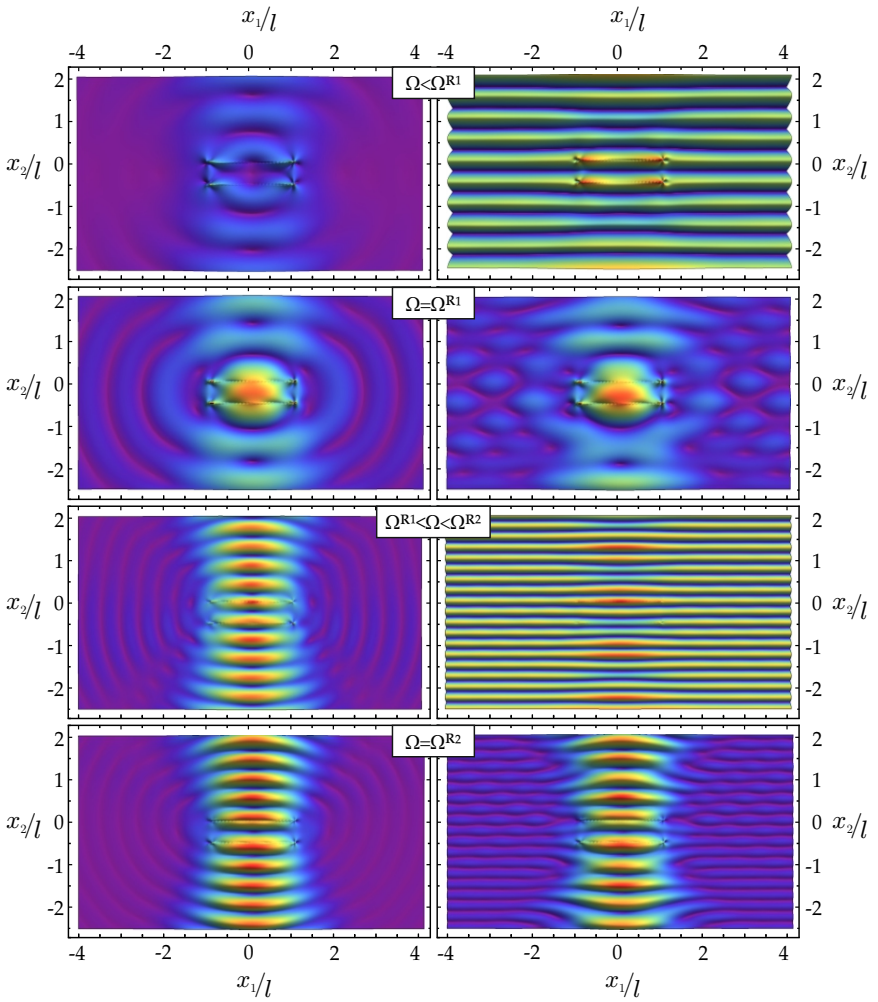

FIGURE A.5: Scattered (left) and total (right) deviatoric strain fields for two parallel cracks of length $2\,l$ and distance $d = 0.5\,l$, and for two cases of frequency before the n-th resonance ($\Omega < \Omega^{Rn}$) and in resonance condition ($\Omega = \Omega^{Rn}$), with $n = 1, 2$.

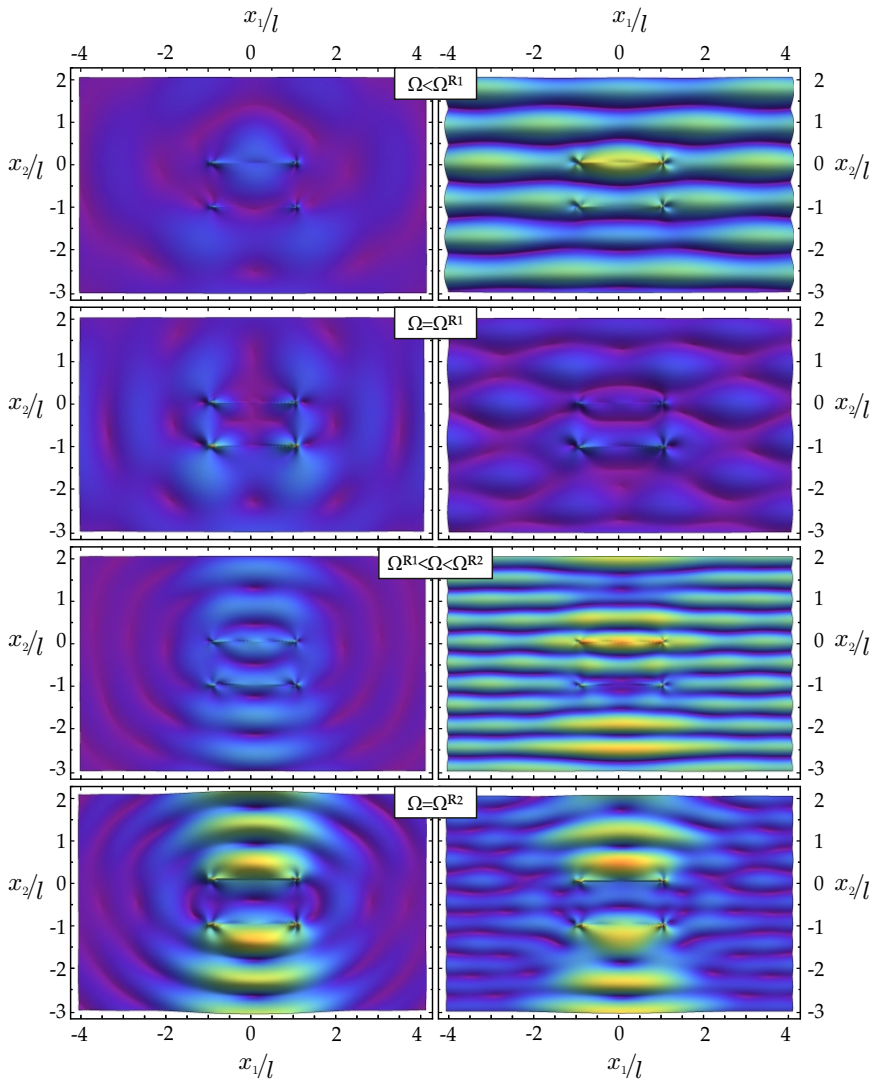

FIGURE A.6: Scattered (left) and total (right) deviatoric strain fields for two parallel cracks of length $2\,l$ and distance $d = l$, and for two cases of frequency before the n-th resonance ($\Omega < \Omega^{Rn}$) and in resonance condition ($\Omega = \Omega^{Rn}$), with $n = 1, 2$.

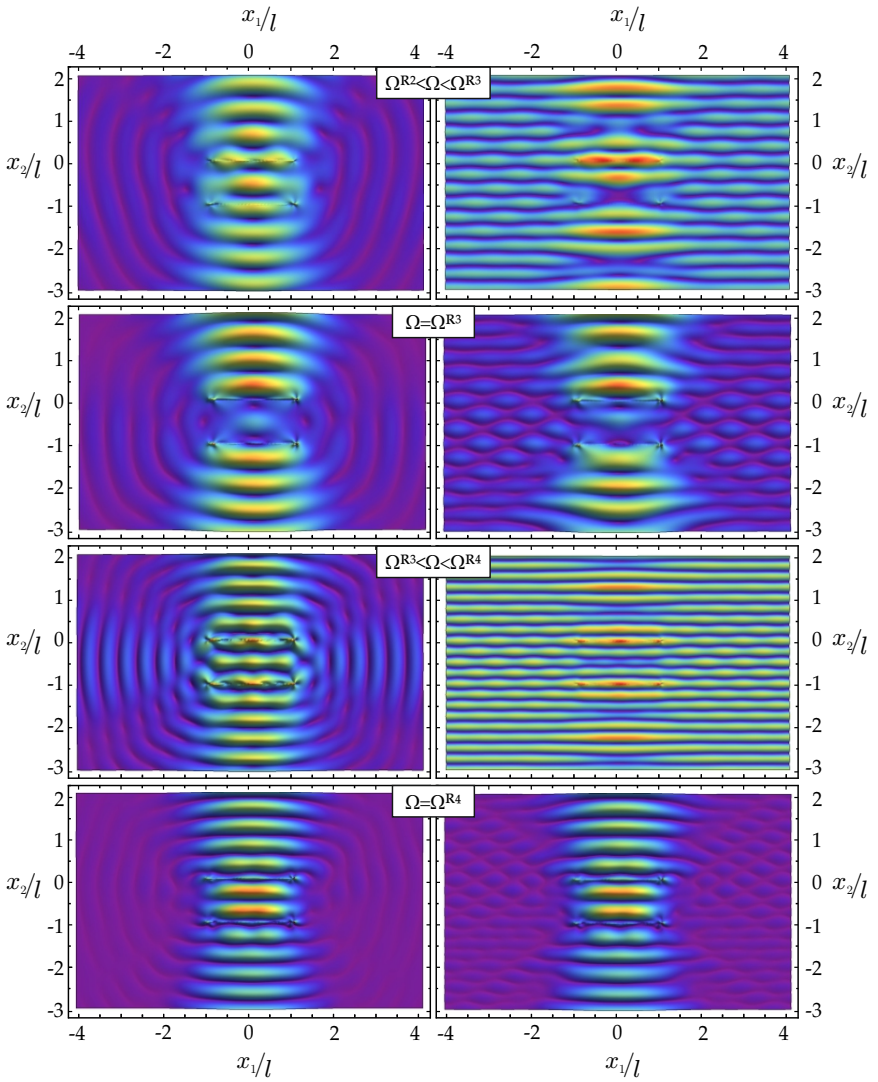

FIGURE A.7: Scattered (left) and total (right) deviatoric strain fields for two parallel cracks of length $2\,l$ and distance $d = l$, and for two cases of frequency before the n-th resonance ($\Omega < \Omega^{Rn}$) and in resonance condition ($\Omega = \Omega^{Rn}$), with $n = 3, 4$.

B Regularization of the traction of the Green's function

The gradient of the nominal stress tensor $\dot{t}^g_{ij,k}$ is obtained by the plane wave expansion as

$$\dot{t}^g_{ij,k} = -\frac{1}{4\pi^2}\int_{\boldsymbol{\omega}} \tilde{t}^g_{ij,k}(\boldsymbol{\omega})\, d\omega, \tag{B.0.1}$$

and it can be decomposed into a static and a dynamic contribution as

$$\tilde{t}^g_{ij,k}(\boldsymbol{\omega}) = \tilde{t}^{g(st)}_{ij,k}(\boldsymbol{\omega}) + \tilde{t}^{g(dyn)}_{ij,k}(\boldsymbol{\omega}), \tag{B.0.2}$$

which are defined as

$$\tilde{t}^{g(st)}_{ij,k}(\boldsymbol{\omega}) = -\frac{\tilde{F}^g_{ijk}(\boldsymbol{\omega})}{(\boldsymbol{\omega}\cdot\mathbf{x})^2}, \tag{B.0.3}$$

$$\tilde{t}^{g(dyn)}_{ij,k}(\boldsymbol{\omega}) = \left[\omega_g\omega_k\delta_{ij} - \tilde{F}^g_{ijk}(\boldsymbol{\omega})\right]\eta^2\Xi'(\eta\boldsymbol{\omega}\cdot\mathbf{x}), \tag{B.0.4}$$

where a prime denotes differentiation with respect to $\boldsymbol{\omega}\cdot\mathbf{x}$ and

$$\tilde{F}^g_{ijk}(\boldsymbol{\omega}) = \mathbb{K}_{ijhl}\omega_k\omega_h\frac{\delta_{lg}-\omega_l\omega_g}{L(\boldsymbol{\omega})} + \left(\frac{\omega_g(2\mu_*-\mu)(1-\omega_g^2)}{L(\boldsymbol{\omega})} + \right.$$
$$\left. + \frac{(\mu-(\delta_{2g}-\delta_{1g}))\frac{\sigma}{2}\omega_g^2}{L(\boldsymbol{\omega})} - \frac{\sigma}{2}\omega_k\frac{\omega_1\omega_2^2}{L(\boldsymbol{\omega})}\right)\delta_{ij}. \quad \text{(B.0.5)}$$

By specifying the unit vector $\boldsymbol{\omega}$ as

$$\omega_1 = \cos(\alpha+\theta), \quad \omega_2 = \sin(\alpha+\theta), \quad \text{(B.0.6)}$$

the static contribution (B.0.3) is strongly singular in both the variables α and r, so that, to evaluate the plane wave expansion (B.0.1), the quantity $\tilde{t}^{g(st)}_{ij,k}$ is regularized as follows

$$\tilde{t}^{g(st)}_{ij,k}(\boldsymbol{\omega}) = \frac{\tilde{T}^g_{ijk}(\alpha,\theta)}{r^2}, \quad \text{(B.0.7)}$$

where

$$\tilde{T}^g_{ijk} = -\frac{1}{\cos^2\alpha}\left[\tilde{F}^g_{ijk}(\alpha+\theta) - \left(\tilde{F}^g_{ijk}(\alpha+\theta)\right)_{\alpha=\pi/2}\right.$$
$$\left. - \left(\alpha-\frac{\pi}{2}\right)\left(\tilde{F}^g_{ijk}(\alpha+\theta)\right)'_{\alpha=\pi/2}\right], \quad \text{(B.0.8)}$$

in which the prime denotes differentiation with respect to α.

List of Figures

Bibliography

[1] Argani, L., Bigoni, D., Capuani, D., Movchan, N.V. (2014) Cones of localized shear strain in incompressible elasticity with prestress: Green's function and integral representations. Proc. R. Soc. A 470, 20140423.

[2] L. Argani, D. Bigoni, G. Mishuris Dislocations and inclusions in prestressed metals. Proc. R. Soc. A A, 2013, 469, 2154 20120752.

[3] Barraa, L.P.S., Telles, J.C.F. (1999) A hyper-singular numerical Green's function generation for BEM applied to dynamic SIF problems. Engineering Analysis with Boundary Elements 23, 77-87.

[4] Bigoni, D. (2012) Nonlinear Solid Mechanics Bifurcation Theory and Material Instability. Cambridge University Press.

[5] Bigoni, D., Bordignon, N., Piccolroaz, A., Stupliewickz, S. (2017) Bifurcation of elastic solids with sliding interfaces. Proc. R. Soc. A In press.

[6] Bigoni, D., Capuani, D. (2002) Green's function for incremental nonlinear elasticity: shear bands and boundary integral formulation. J. Mech. Phys. Solids 50, 471-500.

[7] Bigoni, D., Capuani, D. (2005) Time-harmonic Green's function and boundary integral formulation for incremental nonlinear elasticity: dynamics of wave patterns and shear bands. J. Mech. Phys. Solids 53, 1163-1187.

[8] Bigoni, D., Capuani, D., Bonetti, P. and Colli, S. (2007) A novel boundary element approach to time-harmonic dynamics of incremental nonlinear elasticity: The role of pre-stress on structural vibrations and dynamic shear banding. Comput. Meth. Appl. Mech. Engrg. 196, 4222-4249.

[9] Bigoni, D., Dal Corso, F. (2008) The unrestrainable growth of a shear band in a prestressed material. Proc. R. Soc. A 464, 2365-2390.

[10] Biot, M.A. (1965) *Mechanics of incremental deformations*. J. Wiley and Sons, New York.

[11] Blanloeuil, P., Rose, L.R.F., Guinto, J.A., Veidt, M., Wang, C.H. (2016) Closed crack imaging using time reversal method based on fundamental and second harmonic scattering. Wave Motion 66, 156-176.

[12] Bonnet-Lebouvier, A.S., Molinari, A., Lipinski, P., (2002) Analysis of the dynamic propagation of adiabatic shear bands. Int. J. Solids Structures 39, 4249-4269.

[13] Bordignon, N., Piccolroaz, A., Dal Corso, F., Bigoni, D. (2015) Strain localization and shear banding in ductile materials. Frontiers in Materials, 2, 1-13.

[14] Brun, M., Capuani, D., Bigoni, D. (2003) A boundary element technique for incremental, non-linear elasticity Part I: Formulation. Comput. Meth. Appl. Mech. Engrg. 192, 2461-2479.

[15] Capuani, D., Bigoni, D., Brun, M. (2005) Integral representations at the boundary for Stokes flow and related symmetric Galerkin formulation. Arch. Mech. 57, 363-385.

[16] Capuani, D., Willis, J.R. (1997) Wave propagation in elastic media with cracks. Part I: transient nonlinear response of a single crack. Eur. J. Mech. A/Solids, vol. 16, 377-408.

[17] Chen, E.P., Sih, G.C. (1977) Scattering waves about stationary and moving cracks. *Mechanics of fracture:Elastodynamic crack problems*, pp. 119-212. Noordhoff, Leyden.

[18] Chirino, F., Abascal, R. (1998) Dynamic and static analysis of cracks using the hypersingular formulation of the boundary element method. Int. J. Num. Meth. Engng. 43, 365-388.

[19] Dineva, P, Gross, D. & Rangelov, T. Dynamic interaction of cracks in piezoelectric and anisotropic solids: a non-hypersingular BIEM approach. *Theoret. Appl. Mech.* **35**, 73-91 (2008).

[20] Dolinski, M., Merzer, M., Rittel, D. (2015) Analytical formulation of a criterion for adiabatic shear failure. Int. J. Impact Eng. 85, 20-26.

[21] Garcia-Sanchez, F., Saez, A., Dominguez, J. (2006) Two-dimensional time-harmonic BEM for cracked anisotropic solids. Engineering Analysis with Boundary Elements 30, 88-99.

[22] Giarola, D., Capuani, D. & Bigoni, D. The dynamics of a shear band. *J. Mech. Phys. Solids* **112**, 472-490 (2018).

[23] Gross, D. & Zhang, C.H. Diffraction of SH waves by a system of cracks: Solution by an integral equation method. *Int. J. Solids Structures* **24**, 41-49 (1986).

[24] Guduru, P.R., Rosakis, A.J., Ravichandran, G. (2001) Dynamic shear bands: an investigation using high speed optical and infrared diagnostic Mech. Materials 33, 371-402.

[25] He, J., *et al.* Local microstructure evolution at shear bands in metallic glasses with nanoscale phase separation. *Scientific Reports* **6**, 25832 (2016).

[26] Hill, R. (1958) A general theory of uniqueness and stability in elastic-plastic solids. J. Mech. Phys. Solids 6, 236-249.

[27] Hill, R., Hutchinson, J.W. (1975) Bifurcation phenomena in the plane tension test. J. Mech. Phys. Solids 23, 239-264.

[28] Hsieh, T.H., Kinloch, A.J., Masania, K., Taylor, A.C. & Sprenger, S. The mechanisms and mechanics of the toughening of epoxy polymers modified with silica nanoparticles. *Polymer* **51**, 6284-6294 (2010).

[29] Hutchinson, J.W., Neale, K.W. (1979) Finite strain J2-deformation theory. In Proc. IUTAM Symp. on Finite Elasticity (eds D. E. Carlson and R. T. Shield), pp. 237-247. The Hague, The Netherlands: Martinus Nijhoff.

[30] Kalthoff, J.F. (2000) Modes of dynamic shear failure in solids. Int. J. Frac. 101, 1-31.

[31] Keer, L.M., Lin, W., Achenbach, J.D. (1984) Resonance effects for a crack near a free surface. J. Appl. Mech. 51, 65-70.

[32] Kudryashov, N.A., Ryabov, P.N., Zakharchenko, A.S. (2015) Self-organization of adiabatic shear bands in OFHC copper and HY-100 steel. J. Mech. Phys. Solids 76, 180-192.

[33] Li, S., Liu, W.K., Qian, D., Guduru, P.R., Rosakis, A.J., (2001) Dynamic shear band propagation and micro- structure of adiabatic shear band. Comput. Methods Appl. Mech. Eng. 191, 73-92.

[34] Li, S., Liu, W.K., Rosakis, A.J., Belytschko, T. Hao, W. (2002) Mesh-free Galerkin simulations of dynamic shear band propagation and failure mode transition. Int. J. Solids Structures 39, 1213-1240.

[35] Li, W., Gao, Y. & Bei, H. Instability Analysis and Free Volume Simulations of Shear Band Directions and Arrangements in Notched Metallic Glasses. *Scientific Reports* **6**, 34878 (2016).

[36] Ma, M., Vijayan, K., hiltner, A. & Baer, E. Shear yielding modes of polycarbonate *J. Mat. Sci.* **24**, 2687-2696(1989).

[37] Mal, A.K. (1970) Interaction of elastic waves with a Griffith crack. Int. J. Eng. Sci. 8, 763-776.

[38] Manolis, G.D., Dineva, P. S., Rangelov, T. V. (2004) Wave scattering by cracks in inhomogeneous continua using BIEM. Int. J. Solids Structures 41, 3905-3927.

[39] Medyanik, S.N., Liu, W.K., Li, S., (2007) On criteria for dynamic adiabatic shear band propagation J. Mech. Phys. Solids 55, 1439-1461

[40] Merodio, J., Ogden, R.W. (2005) On tensile instabilities and ellipticity loss in fiber-reinforced incompressible non-linearly elastic solids Mech. Res. Comm. 32, 290-299.

[41] Morin, D., Hopperstad, O.S., Benallal, A. (2017) On the description of ductile fracture in metals by the strain localization theory. Int. J. Frac. https://doi.org/10.1007/s10704-017-0236-9.

[42] Needleman, A. (1989) Dynamic Shear Band Development in Plane Strain J. Appl. Mech. 56 1-9.

[43] Ogden, R., Singh, B. (2011) Propagation of waves in an incompressible transversely isotropic elastic solid with initial stress: Biot revisited. J. Mech. Materials Struct. 6, 453-477.

[44] Palmer, A.C., Rice, J.R. (1973) The growth of slip surfaces in the progressive failure of overconsolidated clay. Proc. R. Soc. A 332, 527-548.

[45] Paulino, G.H., Gray, L.J. (1998) Crack Tip Interpolation, Revisited. SIAM Journal on Applied Mathematics. 58, 428-455.

[46] Petryk, H., Kursa, M. (2013) The energy criterion for deformation banding in ductile single crystals. J. Mech. Phys. Solids 61, 1854-1875.

[47] Phan, A.V. Dynamic stress intensity factor analysis of the interaction between multiple impact-loaded cracks in infinite domains. *AIMS Mat. Sci.* **3(4)**: 1683-1695 (2016).

[48] Piccolroaz, A., Bigoni, D., Willis, J.R. (2006) A dynamical interpretation of flutter instability in a continuous medium. J. Mech. Phys. Solids 54, 2391-2417.

[49] Puzrin, A.M. and Germanovich, L.N. (2005) The growth of shear bands in the catastrophic failure of soils. Proc. R. Soc. A 461, 1199-1228.

[50] Qu, R.T, Wang, S.G., Wang, X.D., Liu, Z.Q., Zhang, Z.F. (2017) Revealing the shear band cracking mechanism in metallic glass by X-ray tomography. Scripta Materialia 133, 24-28.

[51] Qu, R.T., Liu, Z.Q., Wang, G. & Zhang, Z.F. Progressive shear band propagation in metallic glasses under compression. *Acta Materialia* **91**, 19-33 (2015).

[52] Radi, E., Bigoni, D., Capuani, D. (2002) Effects of prestress on crack-tip fields in elastic, incompressible solids. Int. J. Solids Structures 39, 3971-3996.

[53] Rice, J.R. (1973) The initiation and growth of shear bands. In Plasticity and Soil Mechanics (ed. A. C. Palmer), p. 263. Cambridge, UK: Cambridge University Engineering Department.

[54] Rojas-Diaz, R., Garcia-Sanchez & F. Saez, A. Dynamic crack interactions in magnetoelectroelastic composite materials. *Int. J. Frac.* **157**, 119-130 (2009).

[55] Ruan, H.H., Zhang, L.C. & Lu, J. A new constitutive model for shear banding instability in metallic glass. *Int. J. Solids Structures* , **48(21)**, 3112–3127 (2011).

[56] Salvadori, A. (2002) Analytical integrations in 2D BEM elasticity. Comput. Meth. Appl. Mech. Engrg. 53, 1695-1719.

[57] Salvadori, A. , Gray, L.J. (2007) Analytical integrations and SIFs computation in 2D fracture mechanics. Comput. Meth. Appl. Mech. Engrg. 70, 445-495.

[58] Shen, Y., Cesnik, C.E.S. (2018) Local interaction simulation approach for efficient modeling of linear and nonlinear ultrasonic guided wave active sensing of complex structures. Journal of Nondestructive Evaluation, Diagnostics and Prognostics of Engineering Systems 1, 011008-1.

[59] Song, S.X., Nieh, T.G. (2011) Direct measurements of shear band propagation in metallic glasses - An overview. Intermetallics 19, 1968-1977.

[60] Tan, A., Hirose, S., Zhang, Ch. (2005) A time-domain collocation-Galerkin BEM for transient dynamic crack analysis in anisotropic solids. Engineering Analysis with Boundary Elements 29, 1025-1038.

[61] Tekoglu, C., Hutchinson, J.W., Pardoen, T. (2015) On localization and void coalescence as a precursor to ductile fracture. Phil. Trans. R. Soc. A 373, 20140121.

[62] Van der Hijden, J.H.M.T., Neerhoff, F.L. (1984) Scattering of Elastic Waves by a Plane Crack of Finite Width. J. Appl. Mech. 51, 646.

[63] Vaz-Romero, A., Rotbaum, Y., Rodriguez-Martinez, J.A., Rittel, D. (2016) Necking evolution in dynamically stretched bars: New experimental and computational insights. J. Mech. Phys. Solids 91, 216-239.

[64] Willis, J.R. (1991) Inclusions and cracks in constrained anisotropic media. In: Wu, J.J., Ting, T.C.T., Barnett, D.M. (Eds.), Modern Theory of Anisotropic Elasticity and Applications. SIAM, Philadelphia, pp. 87-102.

[65] Xu, Y., Zhang, J., Bai, Y., Meyers, M.A. (2008) Shear localization in dynamic deformation: Microstructural evolution. Metallurgical and Materials Transactions A: *Physical Metallurgy and Materials Science* 39, 811-843.

[66] Yang, B., Morrison, M.L., Liaw, P.K., Buchanan, R.A., Wang, G., Liu, C.T., Denda, M. (2005) Dynamic evolution of nanoscale shear bands in a bulk-metallic glass. Applied Phisics Letters 86, 141904.

[67] Zhang, X. (2015) Field Dislocation Mechanics with Applications in Atomic, Mesoscopic and Tectonic Scale Problems. PhD Thesis, Carnegie Mellon University.

[68] Zhang, X., Acharya, A., Walkington, N.J., Bielak, J. (2015) A single theory for some quasi-static, supersonic, atomic, and tectonic scale applications of dislocations. J. Mech. Phys. Solids 84, 145-195.

[69] Zhang, Y., Greer, A.L. (2006) Thickness of shear bands in metallic glasses. Applied Physics Letters 89, 071907.

[70] Zhou, M., Rosakis, A.J., Ravichandran, G. (1996) Dynamically propagating shear bands in impact-loaded prenotched plates. II-Numerical simulations. J. Mech. Phys. Solids 44, 1007-1032.